Title

In Situ/Operando Liquid Cell Transmission Electron Microscopy for Understanding Dynamic Processes of Electrocatalysts and Other Nanomaterials

Author

Wan, Jiawei

Publication Date

2024

Peer reviewed|Thesis/dissertation

In Situ/Operando Liquid Cell Transmission Electron Microscopy for Understanding Dynamic Processes of Electrocatalysts and Other Nanomaterials

By

Jiawei Wan

A dissertation submitted in partial satisfaction of the

requirements for the degree of

Doctor of Philosophy

in

Engineering - Materials Science and Engineering

in the

Graduate Division

of the

University of California, Berkeley

Committee in charge:

Professor Haimei Zheng, Co-Chair

Professor Mark Asta, Co-Chair

Professor Mary Scott

Professor Bryan McCloskey

Fall 2024

In Situ/Operando Liquid Cell Transmission Electron Microscopy

for Understanding Dynamic Processes of Electrocatalysts and Other Nanomaterials

Jiawei Wan

Abstract

In Situ/Operando Liquid Cell Transmission Electron Microscopy

for Understanding Dynamic Processes of Electrocatalysts and Other Nanomaterials

by

Jiawei Wan

Doctor of Philosophy in Engineering - Materials Science and Engineering

University of California, Berkeley

Professor Haimei Zheng, Co-Chair

Professor Mark Asta, Co-Chair

In situ/operando liquid cell transmission electron microscopy (TEM) enables real-time visualization of physical and chemical processes in liquid environments at nanoscale resolution. It creates opportunities to understand the dynamic behavior of nanomaterials across various applications ranging from materials synthesis to energy storage, and chemical production. However, challenges remain in probing dynamic processes of nanomaterials under complex working conditions (e.g., electrocatalysis), which limits mechanistic understanding of the structure-performance correlations. The development of liquid cell TEM platform with enhanced spatial resolution and versatile functionalities, e.g., by implementing multimodal *in situ/operando* capabilities, is essential to overcome the challenge entailing the broader applications.

This dissertation aims to deepen the fundamental understanding of dynamic processes of nanomaterials and reveal their structure-performance correlations by developing and applying *in situ/operando* liquid cell TEM. I focus on two topics of studies on electrocatalysts and nanomotors. The work begins by the innovations of liquid cell microdevices that address challenges in investigating electrochemical systems. By applying *operando* electron microscopy and X-ray spectroscopy, my systematic investigation uncovers the dynamic structural reconstruction of CuO nanowire-derived Cu under carbon dioxide reduction reaction (CO_2RR) working conditions. Additionally, I discover the underlying mechanisms in nanomotor movement through *in situ* liquid cell TEM, thus providing new insights into the structure-performance relationships.

In Chapter 1, I briefly introduce the fundamentals of *in situ/operando* liquid cell TEM and review its applications, including nucleation and growth of nanoparticles, the structural evolutions of electrocatalysts, and electrochemical processes at electrode-electrolyte interfaces of batteries. In Chapter 2, I provide an overview of typical liquid cell designs, followed by the latest techniques and optimized strategies for improving spatial resolution and extending functionality of liquid cells. I emphasize the newly developed polymer membrane-based electrochemical liquid cells, which have enabled high-resolution imaging as well as chemical analysis capabilities during electrochemical reactions. In Chapter 3, I combine the *operando* electrochemical liquid cell TEM (EC-TEM) with time-resolved X-ray absorption spectroscopy (XAS) to unveil the formation

pathways of oxide-derived Cu (OD-Cu) active sites from CuO bicrystal nanowire precatalysts, driven by nanocrack generation and propagation. It provides new mechanistic insights into better control of catalyst structure and performance. In Chapter 4, I further investigate the temperature-dependent structural diversity of Cu nanoparticles formed during electrodeposition for electrocatalyst synthesis. In Chapter 5, I demonstrate the mechanism of the directional movement of $CdCl_2 \cdot 4H_2O$ nanomotors. The facet-dependent reactivity of nanomotor leads to ionic self-diffusiophoresis and drives its movement. Finally, in Chapter 6, I summarize the key findings of this dissertation and provide my perspectives on the future directions for advancing *in situ/operando* liquid cell TEM.

Acknowledgments

First, I would like to express my gratitude to my advisor, Prof. Haimei Zheng. Over the past five years, I have been incredibly fortunate to have had the opportunity to explore the scientific world under her guidance. Her creative ideas, passion for science, and patient mentorship has not only inspired me, but also provided me with a strong platform to grow into an independent researcher. I am also deeply grateful to my co-advisor, Prof. Mark Asta, whose guidance and support have broadened my horizons and knowledge access different fields.

I would also like to extend my sincere thanks to my qualification and dissertation committee members: Prof. Mary Scott, Prof. Bryan McCloskey, Prof. Junqiao Wu, and Prof. Miquel Salmeron. Their expert advice and support have been invaluable throughout my dissertation. I am equally grateful to all the professors who provided courses and instructions, helping me build a solid foundation for my research.

A heartfelt thank you goes to my group members, including Dr. Qiubo Zhang, Mr. Yi Chen, Dr. Junyi Shangguan, Dr. Xinxing Peng, Dr. Sophia Betzler, Dr. Seunyong Lee, Mr. Daewon Lee, Dr. Yu Wang, Dr. Xianhu Sun, Dr. Diyi Cheng, Dr. Qi Zheng, Ms. Amy Ren, Mr. Jiana Zheng, Dr. Yujun Xie, Dr. Wen Wang, Dr. Jiawei Sun, Dr. Chi Zhang, Mr. Mo Lin, Mr. Kai-Yuan Hsiao, and Mr. Masaya Sakakibara. I have learned immensely from the professional discussions and collaborations, and the atmosphere in the lab has been a great source of joy and inspiration.

I am deeply appreciative of my collaborators, whose contributions make my research fruitful. Dr. Ershuai Liu and Dr. Walter S. Drisdell provide exceptional experimental skills and insightful feedback on XAS. Dr. Jiayun Liang and Prof. Zakaria Y. Al Balushi offer remarkable expertise in both experiments and simulations. Dr. Buyu Zhang and Prof. Mark Asta's pivotal role in theoretical calculations greatly advanced our work. Special thanks to Dr. Woong Choi, Dr. Keon-Han Kim, Mr. Changlian Wen, Dr. Adam Z. Weber, and Prof. Alexis T. Bell for their expertise in electrocatalysis. Dr. Meng Zhang and Dr. Han Xue's remarkable skills in electron microscopy impressed me a lot. I also appreciate the support from Dr. Ji Yang and Dr. Ji Su in materials synthesis. My gratitude extends to Dr. Karen C. Bustillo, Dr. Peter Ercius, Dr. Rohan Dhall, Mr. Chengyu Song, Dr. Eli Stavitski, Dr. Denis Leshchev, Dr. Akhil Tayal, Dr. Lu Ma, and Dr. Dali Yang for their invaluable technical support. Special thanks also go to Dr. Ji Yang, Dr. Yuhang Cai, Dr. Hao Chen, Dr. Ruihan Guo, Dr. Healin Im, Dr. Ershuai Liu, Dr. Han Xue, and Dr. Meng Li for initiate collaborations that enriched my research.

The long journey of my Ph.D. would not have been possible without the support of my family and friends. Their patience, encouragement, and belief in me have been my motivation through challenges, and they have shared in the joy of each accomplishment. A special thank you goes to Dr. Xiao Zhao, Dr. Yizhen Chen, Dr. Hao Chen, Dr. Ji Yang, Dr. Xin Chen, Dr. Ershuai Liu, and Dr. Han Xue for the fun and camaraderie we've shared.

Finally, I would like to express my deepest gratitude to my wife, Dr. Jiayun Liang. Your unwavering love, patience, encouragement, and support have been my constant source of strength throughout this journey. This accomplishment would not have been possible without you by my side.

Table of Contents

List of Figures

List of Tables

List of abbreviations and symbols

1D	One-dimensional
2D	Two-dimensional
3D	Three-dimensional
4D-STEM	Four-dimensional scanning transmission electron microscopy
AFM	Atomic force microscopy
C_{2+}	Multicarbon
CA	Chronoamperometry
CAB	Cellulose acetate butyrate
CE	Counter electrode
CO_2RR	Carbon dioxide reduction reaction
CV	Cyclic voltammetry
DEC	Dimethyl carbonate
DFT	Density functional theory
DP	Diffraction pattern
EC	Ethylene carbonate
ECSA	Electrochemical active surface area
EC-TEM	Electrochemical liquid cell transmission electron microscopy
EDS	Energy-dispersive X-ray spectroscopy
EELS	Energy-dispersive X-ray spectroscopy
EIS	Electrochemical impedance spectroscopy
Cryo-EM	Cryogenic electron microscopy
Cryo-ET	Cryogenic transmission electron tomography
ETFE	Ethylene tetrafluoroethylene
EXAFS	Extended X-ray absorption fine structure
FE	Faradaic efficiency
FEM	Finite element model
FFT	Fast Fourier transform
FT	Fourier transform
GDL	Gas diffusion layer

GGA	Generalized gradient approximation
HAADF	High-angle annular dark-field
HER	Hydrogen evolution reaction
HERFD	High energy resolution fluorescence detected
HIF	High index facets
HRTEM	High-resolution transmission electron microscopy
LDH	Layered double hydroxide
LPCVD	Low-pressure chemical vapor deposition
LSV	Linear sweep voltammetry
MEA	Membrane electrode assembly
MOF	Metal-organic framework
MTC	Mass-thickness contrast
NC	Nanocluster
NEB	Nudged Elastic Band
NMR	Nuclear magnetic resonance
NP	Nanoparticle
NW	Nanowire
OCV	Open-circuit voltage
OD-Cu	Oxide-derived Cu
OER	Oxygen evolution reaction
ORR	Oxygen reduction reaction
PBE	Perdew-Burke-Ernzerhof
PMMA	Poly (methyl methacrylate)
PTL	Porous transport layers
PVD	Physical vapor deposition
RDF	Radial distribution function
RE	Reference electrode
RHE	Reversible hydrogen electrode
RIE	Reactive ion etching
SAED	Selected area electron diffraction
SEI	Solid-electrolyte interface
SEM	Scanning electron microscopy

SHE	Standard hydrogen electrode
STEM	Scanning transmission electron microscopy
TB	Twin boundary
TEM	Transmission electron microscopy
UPD	Underpotential deposition
VASP	Vienna ab initio simulation package
WE	Working electrode
XANES	X-ray absorption near-edge structure
XAS	X-ray absorption spectroscopy
XRD	X-ray Diffraction
XRF	X-ray fluorescence spectroscopy
ZIF	Zeolitic imidazolate framework

Chapter 1

Liquid cell transmission electron microscopy

This chapter introduces the concept of liquid cell transmission electron microscopy (TEM) and its role in advancing the state-of-the-art applications for studying the structural dynamics of nanomaterials in liquids and dynamic phenomena at solid-liquid interfaces. It provides a review of *in situ/operando* liquid cell TEM, highlighting the critical role in investigating the mechanisms of functional materials since the invention of electron microscopy. The chapter also summarizes the current limitations and challenges in the field, setting the stage for the key focus of this dissertation: exploring new possibilities for correlating nanomaterial structures with their functions by real-time imaging with the necessary spatial and temporal resolution. Lastly, an outline of the remainder of the dissertation is provided.

1.1 An overview of liquid cell TEM

Transmission electron microscope is a powerful tool that has widely used to investigate the microscopic structure of materials at nanoscale and beyond[1–4]. By utilizing a highly focused electron beam with an extremely short wavelength, it enables the visualization of nanomaterials with the atomic resolution[5]. Beyond imaging, TEM can be coupled with analytical techniques such as energy-dispersive X-ray spectroscopy (EDS)[6] and electron energy loss spectroscopy (EELS)[7], allowing to provide detailed chemical and electronic information of the sample. These advanced techniques facilitate the study of materials composition, structure and bonding, which are critically important for developing a comprehensive understanding of the materials. TEM has become indispensable in physics[8–11], chemistry[12,13], biology[3,14,15], geology[16,17], as well as materials science[18–20] and nanotechnology[21,22], with applications ranging from assisting the development of novel functional nanomaterials to visualization of biological macromolecules. It remains a leading tool in nanoscale research and discovery.

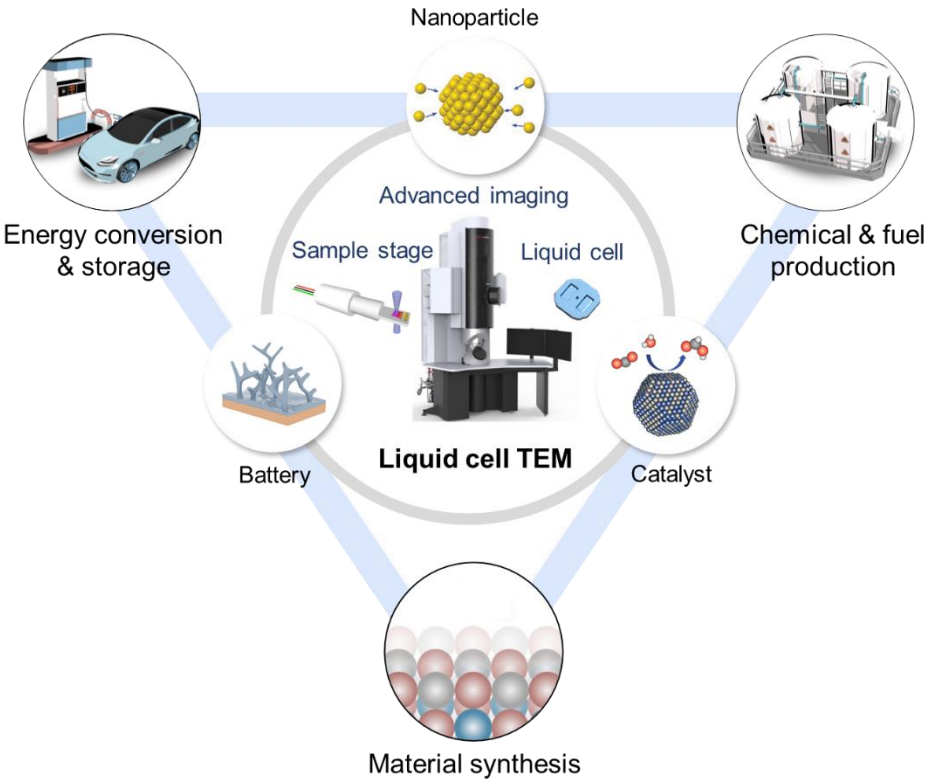

Figure. 1.1: Applications of *in situ/operando* liquid cell TEM. A typical liquid cell TEM platform consists of an electron microscope for advanced imaging, paired with a specially designed sample stage and liquid cells. *In situ/operando* liquid cell TEM provides the capability to monitor reactions in liquid environments in real-time, such as nanoparticle growth and transformations, the structural evolution of battery materials, electrocatalysts restructuring and so on. These real-time observations offer valuable insights for improving materials synthesis, energy conversion and

storage, as well as chemical and fuel production. Reprinted with permission from Reference 18 © 2024 AAAS, and 20 © 2020 AAAS.

Conventional TEM requires samples to be placed in a high vacuum environment, which makes it unsuitable for studying processes that naturally occur in liquids, including many important physical, chemical, and biological phenomena. Liquid cell TEM techniques overcome this limitation by enclosing the liquid samples in a sealed and electron-transparent microdevice, named liquid cell[21,23–25], integrated with a functional sample stage. This setup allows researchers to directly visualize and analyze structural, chemical, and morphological changes in materials in liquids as they undergo dynamic processes in real-time (**Fig. 1.1**). For example, the nanoparticle behaviors in solutions can be studied, e.g., nucleation and growth[26–35,16], phase transformation[36–39], self-assembly[40–46], corrosion[47–55], and dynamic motion[56–60]. Moreover, it can realize observation of biological samples in wet condition[43,61–63]. External stimulus can be integrated into the liquid cells as well. For instance, thermal heating helps explore thermally induced nucleation and growth[30,33], while biasing is important for research on various electrochemical processes, including electrodeposition[25,64,65], rechargeable batteries[66–69], and electrocatalysis[38,50,70–74].

These capabilities of liquid cell TEM are essential for driving breakthroughs in technology developments and innovations in materials synthesis, energy conversion and storage, and chemical and fuel production. By enabling direct observation of nanoscale materials dynamic processes in their native environments, liquid cell TEM provides critical insights into reaction mechanisms and material transformations, which are vital for development of advanced materials and devices.

1.2 Investigation of nanomaterial transformations using liquid cell TEM

1.2.1 Nucleation and growth

Nucleation and growth in solution-phase synthesis have traditionally been described by the classical theory that it is driven by the competing surface energy and volume energy in colloidal chemistry, while recent studies have revealed nonclassical multistep crystallization[75,76]. *In situ* liquid cell TEM provides an ideal platform for uncovering the pathways and intricate information of these processes, enabling the study of nanoparticle growth and elucidating the factors that control the structure and morphology of nanoparticles[26–35,16].

The formation of Pt nanocube has been investigated using *in situ* liquid cell TEM[26]. Contrary to the surface energy minimization rule, the growth rates of all low-index facets are similar until the {100} facets cease growing. Subsequently, the {110} facets continue to grow until they reach a limit, forming the edges of a nanocube, while the continued growth of {111} facets fill the corners. Liquid cell TEM imaging also provides valuable insights into the growth mechanisms of one-dimensional (1D) nanostructures. Single Pt_3Fe nanorod grows from a molecular precursor solution[27]. Initial nanoparticles form and subsequently attach end-to-end to create a nanowire, with the formation of such nanoparticle chains attributed to dipolar interactions between the nanoparticles. In addition, the ligand-controlled oriented attachment of Au nanoparticles has been observed at atomic resolution under *in situ* liquid cell TEM (**Fig. 1.2a**)[34]. In this case, pairs of Au nanocrystals preferentially contact via {111} facets and begin orienting with one another. As they approach, the angle difference between the Au (111) planes of the two nanoparticles gradually decreased from 31° to 0°. Additionally, since processes at the nanoscale

often diverge from our macro- and microscopic understanding, liquid cell TEM studies have revealed unexpected growth pathways. For instance, the growth of two-dimensional (2D) metal oxide sheets has been discovered through the nucleation of intermediate three-dimensional (3D) nanoparticles that transform into nanosheets. These nanosheets subsequently grow into larger ones through coalescence (**Fig. 1.2b**)[77]. It's proposed that both negative surface energy and particle size contribute to the 3D-to-2D transformations.

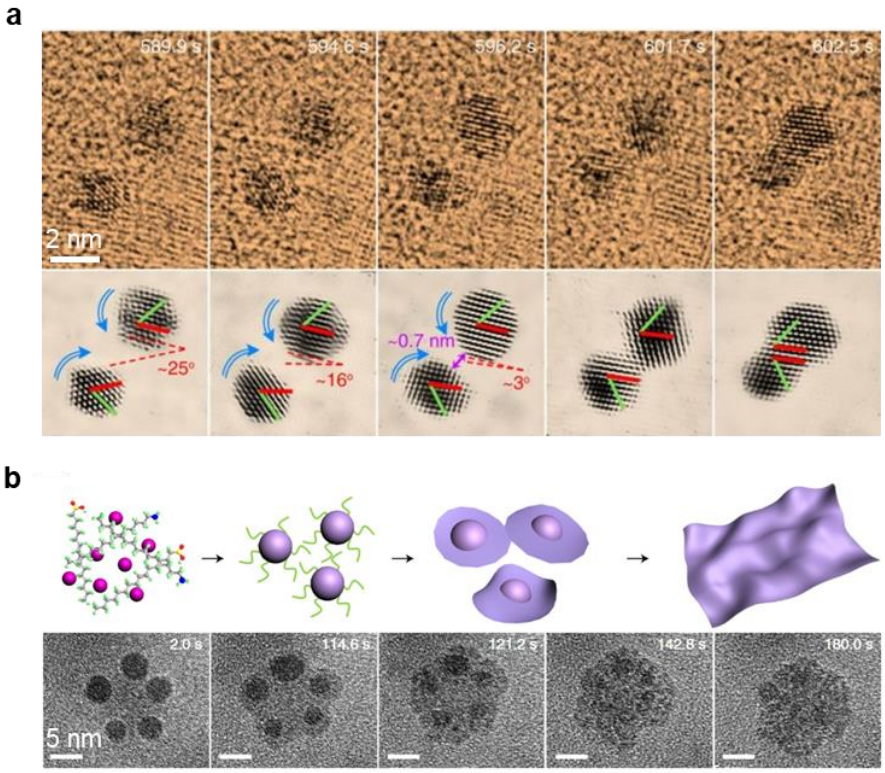

Figure. 1.2: Nucleation and growth of nanoparticles investigated by *in situ* liquid cell TEM. *In situ* observation of (**a**) ligand-controlled oriented attachment of Au nanoparticles, and (**b**) the formation of a 2D cobalt nickel oxide nanosheets from a molecular precursor solution with the pathway of 3D nanoparticle growth followed by 3D-to-2D transformations. (a) Reprinted with permission from Reference 34. © 2018 Springer Nature. (b) Reprinted with permission from Reference 77. © 2019 Springer Nature.

1.2.2 Etching and corrosion

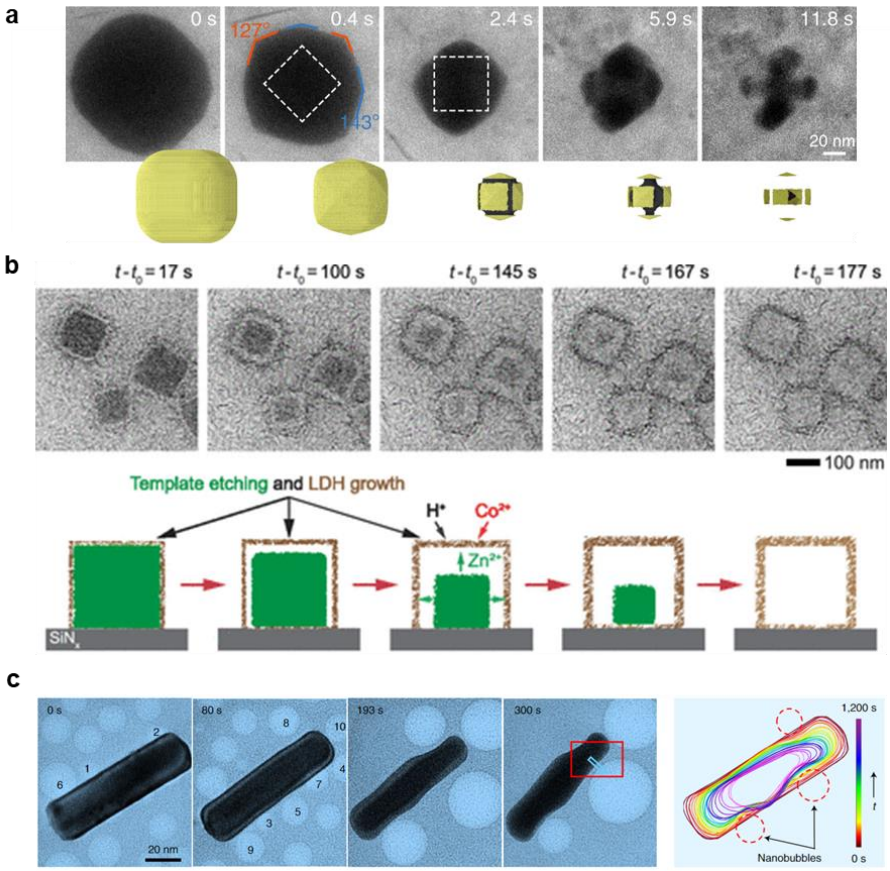

Figure. 1.3: Etching and corrosion of nanoparticles investigated by *in situ* liquid cell TEM. *In situ* observation of (**a**) the dissolution of a Pd@Au nanocube, (**b**) the transformation of MOFs into LDHs using ZIF-8 nanocubes as etching templates, (**c**) the etching of a Au nanorod at solid-liquid-gas interfaces. (a) Reprinted with permission from Reference 48. © 2020 Springer Nature. (b) Reprinted with permission from Reference 54. © 2021 American Chemical Society. (c) Reprinted with permission from Reference 55. © 2022 Springer Nature.

Etching and corrosion are significant concerns in the application of metals and alloys, often leading to structural damage and device failure[78,79]. One of the greatest challenges is accurately predicting how and where materials will degrade under specific conditions, largely due to a limited understanding of the precise corrosion mechanisms. *In situ* liquid cell TEM offers a unique opportunity to gain deeper insights into these mechanisms by dynamically capturing microstructural and chemical changes at high-resolution in realistic or near-realistic environments[47–55].

For example, time-series *in situ* TEM images show that a Pd@Au nanocube undergoes rapid oxidative etching with terminated {210} facets. The dissolution of the Pd core proceeds more rapidly than that of the Au shell upon exposure to the etching solution, resulting in a complex architecture where Au branches are interconnected through a central Pd core (**Fig. 1.3a**)[48]. Additionally, liquid cell TEM provides valuable insights into chemical etching mechanisms used in synthesis. The transformation mechanism of metal-organic frameworks (MOFs) into layered

double hydroxides (LDHs) has been investigated using zeolitic imidazolate framework-8 (ZIF-8) nanocubes as etching templates[54]. As shown in **Fig. 1.3b**, the {100} facets of the ZIF-8 nanocubes are initially etched, creating a gap between the newly formed LDH shell and the shrinking ZIF-8 core. Eventually, the remaining ZIF-8 is fully etched away, completing the transformation into LDH nanocages. Furthermore, the corrosion processes of nanoparticles at solid-liquid-gas interfaces can also be observed using *in situ* liquid cell TEM. The corrosion of Au nanorods has been monitored in aqueous hydrobromic acid with atomic-level resolution, revealing that the etching rate of the nanorods is directly related to the distance between oxygen nanobubbles, which provides new insights into the mechanisms of solid-liquid-gas reactions (**Fig. 1.3c**)[55].

1.2.3 Self-assembly

Self-assembly, the spontaneous organization of molecules or nanoparticles into structured functional materials, is fundamental to both natural systems and advanced synthetic nanomaterials[80,81]. *In situ* liquid cell TEM enables the direct observation of the formation, growth, and interaction of nanoparticles in solution to capture the dynamics of self-assembly in liquid environments. This technique provides critical insights into the kinetics, pathways, and mechanisms of self-assembly, shedding light on how factors such as concentration, temperature, or external stimuli influence the organization of nanostructures[40–46].

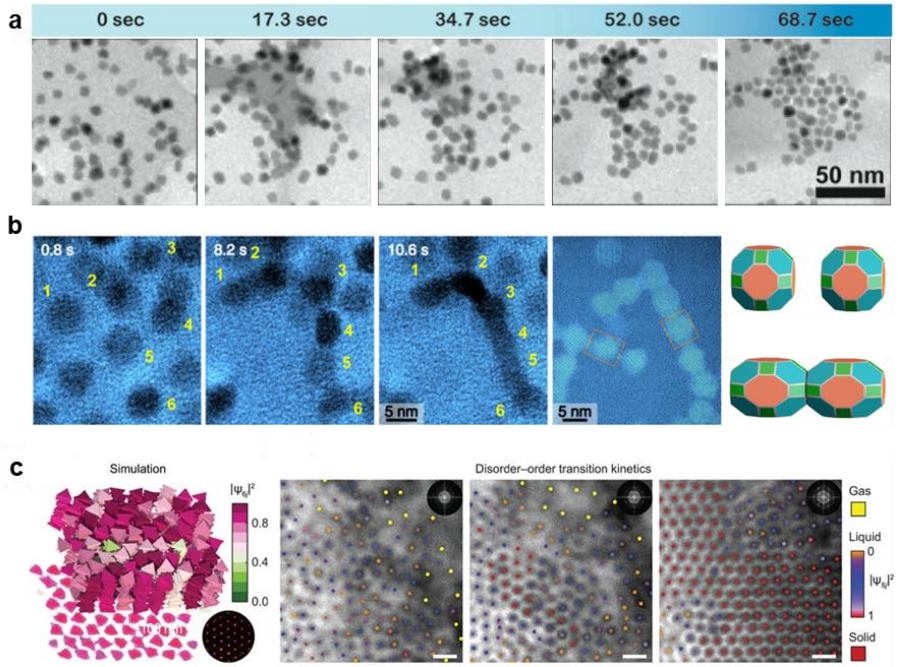

Figure. 1.4: Self-assembly of nanoparticles revealed by *in situ* liquid cell TEM. (**a**) Pt superlattice formation from nanoparticles. (**b**) Self-assembly of PbSe nanoparticles from 2D hexagonal monolayer to a 1D nanocrystal chain. (**c**) 3D hexagonal columnar superlattice formed by triangular nanoprisms. (a) Adapted with permission from Reference 40. © 2012 American Chemical Society. (b) Adapted with permission from Reference 42. © 2019 AAAS. (c) Reprinted with permission from Reference 44. © 2019 Springer Nature.

Researchers have reported the real-time formation of 2D nanoparticle arrays under conditions of low diffusive limit, where nanoparticles are primarily driven by capillary forces and solvent fluctuations (**Fig. 1.4a**)[40]. They find that superlattice formation occurs in multiple stages. Initially, the solvent front drags the nanoparticles, condensing them into an amorphous agglomerate. Subsequently, local fluctuations drive the crystallization of the nanoparticles into an ordered array. *In situ* liquid cell TEM also reveals the transformation behavior of individual nanocrystals during superlattice phase transitions (**Fig. 1.4b**)[42]. PbSe nanocrystals exhibit significant directional shape deformation when the spacing between two nanocrystals reached 2 to 4 nm. Remarkably, this deformation can either be fully recover when the nanocrystals move apart or retain when they attach. Furthermore, 3D nanocrystal superlattices have been explicitly analyzed during complex structural evolutions in the crystallization process (**Fig. 1.4c**)[44]. In this case, the system consists of anisotropic Au triangular nanoprisms coated with negatively charged carboxylate ligands, providing electrostatic repulsion in water. As the ion concentration increases, van der Waals attraction between the nanoprisms overcomes the electrostatic repulsion, driving the prisms to stack face-to-face into cylindrical columns standing on the membrane. These columns then interact laterally, assembling into a hexagonal columnar superlattice.

1.2.4 Dynamic motion

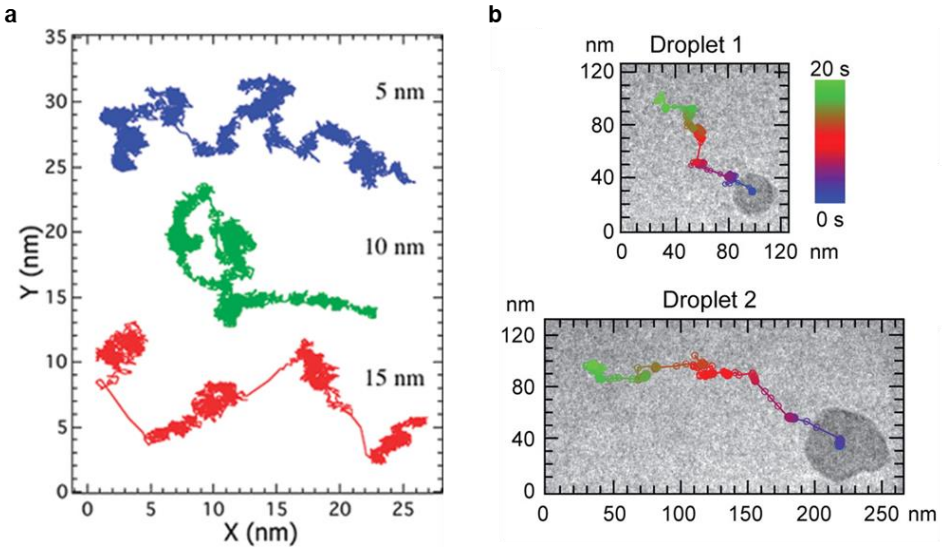

Figure. 1.5: Tracking dynamic motion of nanoparticles by *in situ* liquid cell TEM. (**a**) Trajectory of Au nanoparticles with different sizes. (**b**) The translocation of nanodroplet. (a) Reprinted with permission from Reference 56. © 2009 American Chemical Society. (b) Reprinted with permission from Reference 57. © 2012 National Academy of Sciences.

In situ liquid cell TEM allows researchers to track individual nanoparticles in real-time as they diffuse, rotate and interact with other particles responding to external stimuli[56–60]. For example, researchers have directly resolved the complex motion of inorganic nanoparticles within

a thin liquid film during solvent evaporation (**Fig. 1.5a**)[56]. Additionally, the technique has enabled the direct observation of stick-slip movements in water nanodroplets induced by the electron beam. These insights lay the groundwork for future studies of correlated motion in more concentrated nanoparticle solutions, as well as for investigations into particle diffusion during self-assembly to create complex functional nanoparticle arrangements (**Fig. 1.5b**)[57].

1.3 Mechanism studies of functional materials using electrochemical liquid cell TEM

In situ/operando EC-TEM is a state-of-art technique designed to observe and analyze electrochemical reactions in real-time at the nanoscale[82,83]. By incorporating an electrochemical setup within the liquid cell, this method allows researchers to directly visualize the structural and compositional changes in materials during processes such as battery cycling[66–69], electrocatalysis[38,70], and electrodeposition[25,64,65]. This capability is critical for understanding material behavior under working conditions, where reactions are driven by complex interactions between ions, electrons, and surfaces in a liquid environment. *In situ/operando* EC-TEM enables simultaneous imaging and electrochemical measurements, offering insights into reaction mechanisms, degradation pathways, and performance-related transformations. By providing atomic-level observation of these processes, the technique plays a key role in advancing the design of more efficient energy storage systems, catalysts, and other electrochemical technologies, thereby driving innovation in sustainable energy and materials science.

1.3.1 Rechargeable batteries

Various electrochemical processes occur at the electrode-electrolyte interfaces during battery charge and discharge, including Li intercalation[84], solid-electrolyte interface (SEI) formation[85], and Li dendrite growth[86]. To unveil these dynamic phenomena, *in situ* EC-TEM has been developed to replicate the operational conditions of battery materials under electrochemical stimuli, which opens up the opportunity to resolve key questions about electrode-electrolyte interactions in rechargeable batteries[64,66,68,87,88].

For instance, a SiN_x electrochemical liquid cell has been used to monitor Li metal behavior in an ethylene carbonate (EC)/diethyl carbonate (DEC) liquid electrolyte. The *in situ* TEM imaging results reveal the early stages of electrolyte decomposition[66], and the subsequent growth and dissolution of Li dendrites at high-resolution (**Fig. 1.6a**). A Li dendrite suppression strategy is applied through nanoscale engineering under liquid cell TEM, uncovering correlations between Li metal morphologies and the SEI by coupling it with high-resolution EDS[68]. For example, without the polymer film applied to the electrodes, Li is irregularly plated on the electrode, promoting the dendritic growth. The morphology of the dendritic grains varies, likely due to nanoscale inhomogeneities in the local environment (**Fig. 1.6b**). Recently, the transformation of Li polysulfide species has been studied by *in situ* EC-TEM for lithium-sulfur batteries[69]. It provides a clear evidence of evolving Li polysulfide species during charge and discharge processes, revealing two nucleation pathways for Li_2S_2. The time-series TEM images (**Fig. 1.6c**) demonstrate a two-step process: solid nano-nuclei formed at the electrode-electrolyte interface during initial nucleation, followed by the rapid dissolution of smaller metastable particles. This leads to the

elongation of the initial particle along its longitudinal axis, ultimately forming a rod-like Li_2S_2 sulfide structure.

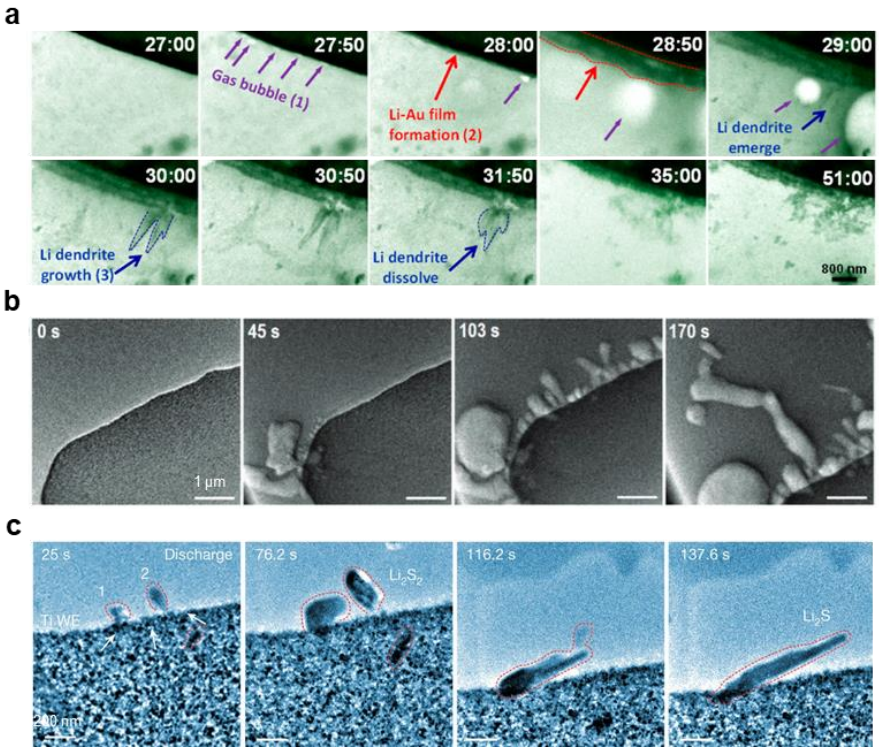

Figure. 1.6: Investigation of battery structural evolution by *in situ* EC-TEM. Sequential TEM images of (**a**) the growth and dissolution of Li-Au alloy, (**b**) Li dendritic growth, and (**c**) the deposition and dissolution of Li_2S in an electrochemical liquid cell. (a) Reprinted with permission from Reference 66. © 2014 American Chemical Society. (b) Reprinted with permission from Reference 68. © 2020 Royal Society of Chemistry. (c) Reprinted with permission from Reference 69. © 2023 Springer Nature.

1.3.2 Electrocatalysis

In situ/operando EC-TEM can also be applied to a wide range of electrocatalytic reactions, such as hydrogen evolution reaction (HER)[89], oxygen evolution reaction (OER)[90], oxygen reduction reaction (ORR)[91], and CO_2RR[92]. Recently, *in situ/operando* EC-TEM has been applied for capturing morphological evolution and phase transformation of electrocatalysts[73,93–95]. This technique is capable for direct investigation of structural dynamics occurring on nanoparticles within the electrolyte in real-time, which provides valuable information assisting the fundamental understanding of underlying mechanisms and catalysts design.

For instance, the dissolution/redeposition mechanisms of Cu nanocatalysts during the early stages of CO_2RR have been revealed (**Fig. 1.7a**)[71]. The formation of small, irregularly shaped nanoparticles is observed, originating from Cu leached out of Cu_2O nanocubes during 45 minutes

of CO_2RR using EC-TEM (**Fig. 1.7b**)[96]. They show that densely loaded cubes and a high density of redeposited nanoparticles contribute to optimal multicarbon (C_{2+}) products selectivity and stability, whereas the detachment of smaller catalyst particles and redeposited nanoparticles lead to performance degradation.

Advanced electron microscopy techniques such as EDS, EELS, and four-dimensional scanning TEM (4D-STEM)[97,98] can provide detailed structural and chemical information during EC-TEM experiments. For OER, EELS can be used to track oxygen evolution under different applied potentials[74]. Correlated changes in the oxygen peak intensity in the EELS spectra and the relative thickness of the liquid layer can be used to probe product formation under electrochemical conditions. **Fig. 1.7c** shows the real-time analysis of the catalytic conversion of adsorbed hydroxide ions into O_2 at the solid-liquid interface using EELS spectra. Additionally, 4D-STEM can be employed to monitor morphological and compositional changes in catalysts during reactions. For example, researchers observe the restructuring of Cu nanoparticles during CO_2RR, discovering that the nanoparticles reorganize into multi-domain granular structures composed of metallic Cu nanograins under reaction conditions (**Fig. 1.7d-f**)[72].

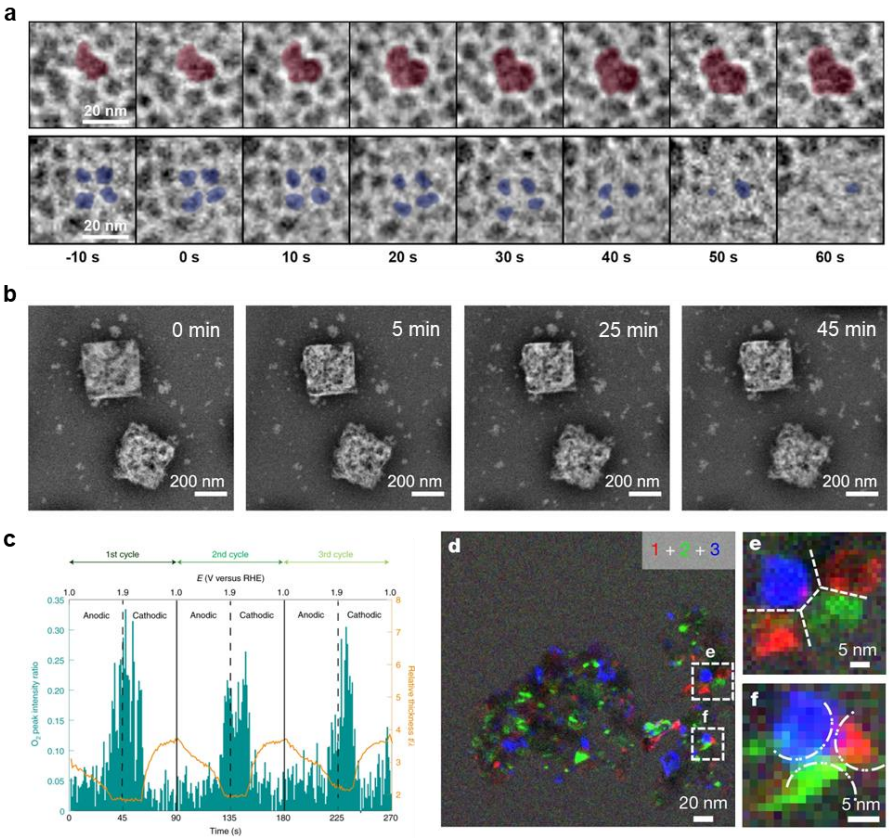

Figure. 1.7: Investigation of electrocatalysts structural evolution by *in situ* EC-TEM. *In situ* observation of (**a**) the dissolution/redeposition of Cu nanoparticles under CO_2RR condition, (**b**) the restructuring of Cu_2O cubes over 45 min of CO_2RR. Advanced techniques such as (**c**) EELS and (**d-f**) 4D-STEM can be utilized to provide structural and chemical information under EC-TEM. (a) Reprinted with permission from Reference 71. © 2020 Wiley. (b) Reprinted with permission

from Reference 96. © 2021 Springer Nature. (c) Reprinted with permission from Reference 74. © 2021 Springer Nature. (d-f) Reprinted with permission from Reference 72. © 2023 Springer Nature.

1.4 Motivation and organization of dissertation

Although the transformation dynamics of nanoparticles, such as nucleation and growth, corrosion, and self-assembly, have been extensively studied using *in situ* liquid cell TEM, understanding the structure-performance correlation in functional materials remains a significant challenge. A major obstacle is the difficulty in directly monitoring the structural evolution of these materials as well as the chemical bonding changes with both high spatial and temporal resolution under operating conditions. This dissertation focuses on understanding the structural transformation mechanisms of electrocatalysts and other nanomaterials (e.g., nanomotor) in aqueous solutions via *in situ/operando* liquid cell TEM techniques.

In Chapter 2, I begin with a brief overview of typical liquid cell designs, followed by a historical development of liquid cell TEM instrument. In this context, I show our development of polymer membrane-based electrochemical liquid cells, which has enabled the study of dynamic phenomena in electrocatalysts during electrocatalytic reactions at high-resolution with elemental composition analysis capability. In Chapter 3, I apply this developed electrochemical liquid cell platform to study electrocatalysis mechanisms. By combining *operando* EC-TEM with time-resolved XAS, our multimodal *operando* techniques unveil the formation pathways of CuO-derived Cu active sites from precatalysts through nanocracking. The nanocrack network help increase the active sites for C_{2+} products. We suggest that nanocracking by tailoring grain boundaries in CuO precatalysts could optimize active Cu nanostructures, and our advanced operando approach provides new mechanistic insights for improving catalyst structure and performance. In Chapter 4, I demonstrate the temperature-dependent structural diversity of Cu nanoparticles formed by electrodeposition. This study deepens our understanding of nucleation in nanostructures and sheds light on the key factors governing the electrodeposition of metal nanoparticles and related nanoscale dynamic processes. In Chapter 5, I present $CdCl_2 \cdot 4H_2O$ nanomotors exhibiting outstanding directional movement in an aqueous solution, driven by electron beam illumination in *in situ* liquid cell TEM. The $CdCl_2 \cdot 4H_2O$ nanocrystals, with different crystal facets, generate an asymmetric chemical concentration gradient due to facet reactivity differences, driving the nanomotor via ionic self-diffusiophoresis. This study represents significant advancements in designing, characterizing, and controlling nanomotors with directional movement, opening future possibilities for chemically powered nanomachines. In Chapter 6, I summarize the principal findings of this dissertation and suggest potential avenues for advancing this body of research. *In situ/operando* liquid cell TEM provides a powerful platform for real-time visualization of dynamic physical and chemical processes, creating new opportunities for mechanistic studies of various functional materials, such as electrocatalysts and rechargeable batteries. However, challenges remain in probing dynamic processes across diverse fields, and further improvements will be necessary to push this research frontier forward.

Chapter 2

Development of electrochemical liquid cells for high-resolution imaging and chemical analysis

In situ/operando liquid cell TEM enables real-time visualization of dynamic physical and chemical processes in liquid environments with nanoscale resolution, which has created great opportunities for understanding material transformations relevant to a wide range of applications, such as nano-synthesis, electrocatalysis, and rechargeable batteries. The success of this technique is primarily attributed to the design and fabrication of liquid cells, microdevices with electron-transparent imaging windows and sealed solutions. This chapter first introduces the development history of liquid cells for *in situ/operando* TEM, focusing on two foundational design approaches that use SiN_x and 2D membranes as the window materials. We highlight the detailed fabrication procedures of liquid cells, including modifications and innovations, along with functionalities such as flow, heating, and biasing. Next, we report the development of the new generation polymer membrane-based electrochemical liquid cells for *in situ/operando* TEM studies on electrocatalysis. This new electrochemical liquid cell design benefits from a thin polymer membrane, enabling observation of materials inside TEM at atomic resolution. It can also provide possibility for elemental composition analysis, including EDS and EELS, which can meet all required conditions for electrocatalytic reactions and is suitable for studying the dynamic phenomena of electrocatalysts.

This work is reproduced in this dissertation with permission from the collaborators. In this work, Mr. Yi Chen, Dr. Diyi Cheng, Dr. Han Xue, and Dr. Ershuai Liu contributes to the liquid cell fabrication and material characterization.

2.1 An overview of liquid cell design for *in situ/operando* TEM

The structures of typical liquid cells are shown in **Fig. 1.1**. The key component of a TEM liquid cell is its membrane, which encapsulates a thin layer of liquid, providing the electron-transparent window through which imaging occurs. Common materials used for these membranes involve SiN_x and atomically thin 2D materials like graphene, which introduces the two design categories: SiN_x membrane-based liquid cell and 2D membrane-based liquid cell[1,99–103]. SiN_x ($x<4/3$) membranes offer a good balance between mechanical strength and electron transparency. However, thick liquid layers can lead to a lower resolution due to the increased scattering or absorption of electrons and they can be expensive and difficult to fabricate[25]. 2D membranes provide superior atomic spatial resolution with minimal background signal, while they lack the control over liquid thickness and amount[21].

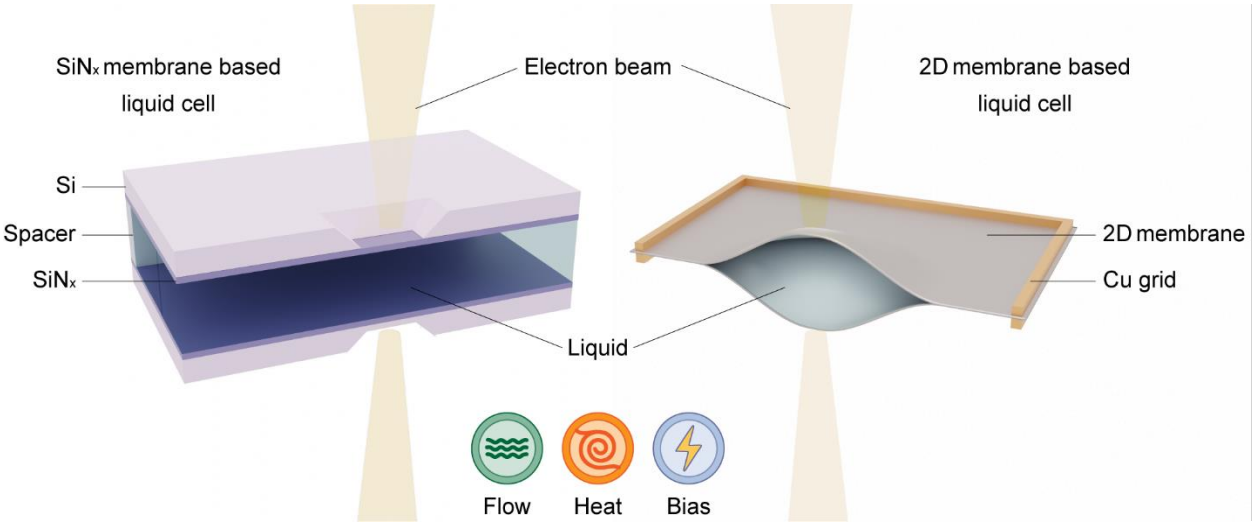

Figure 2.1: Schematic of typical structure of TEM liquid cells, including a SiN_x and a 2D membrane-based liquid cell. Multiple functions can be integrated into liquid cells, such as flow, heating, and biasing.

The liquid cell design must strike a delicate balance between maximizing electron transparency and preserving the natural behavior of the sample within the liquid. This is achieved by controlling the thickness of the membrane and liquid layer, minimizing interaction between the electron beam and the liquid, and ensuring the chemical and mechanical stability of the system over time. Additionally, for applications, such as liquid flow[33,39,61,104,105], heating[33,106,107], and electrochemical biasing[25,38,39,64,70,108], liquid cells are often integrated with specific components (e.g., flow channel, microheater, and electrodes) to enable real-time measurements and analysis of material properties during reactions.

2.2 Development history of liquid cells

The development of liquid cells is the foundation for the field growth of *in situ/operando* liquid cell TEM. The basic concept of static liquid cell design can be attributed to a very early

work in 1944 where liquid could be sealed between two 50 nm collodion membranes (**Fig. 2.2a**)[24]. Advances and success of the modern liquid cell designs and fabrications benefit from the ability to produce durable thin membranes as imaging window[21,25,27,34,38,70] together with multiple capabilities, such as liquid flow[33,39,61,104,109], specimen heating[33,106], and electrochemical biasing[25,38,39,64,70,108]. These capabilities allow probing chemical reactions triggered by the mixing of multiple reactants, at room or elevated temperatures, and the nanoscale details of electrochemical processes related to batteries and electrocatalysis[110–112].

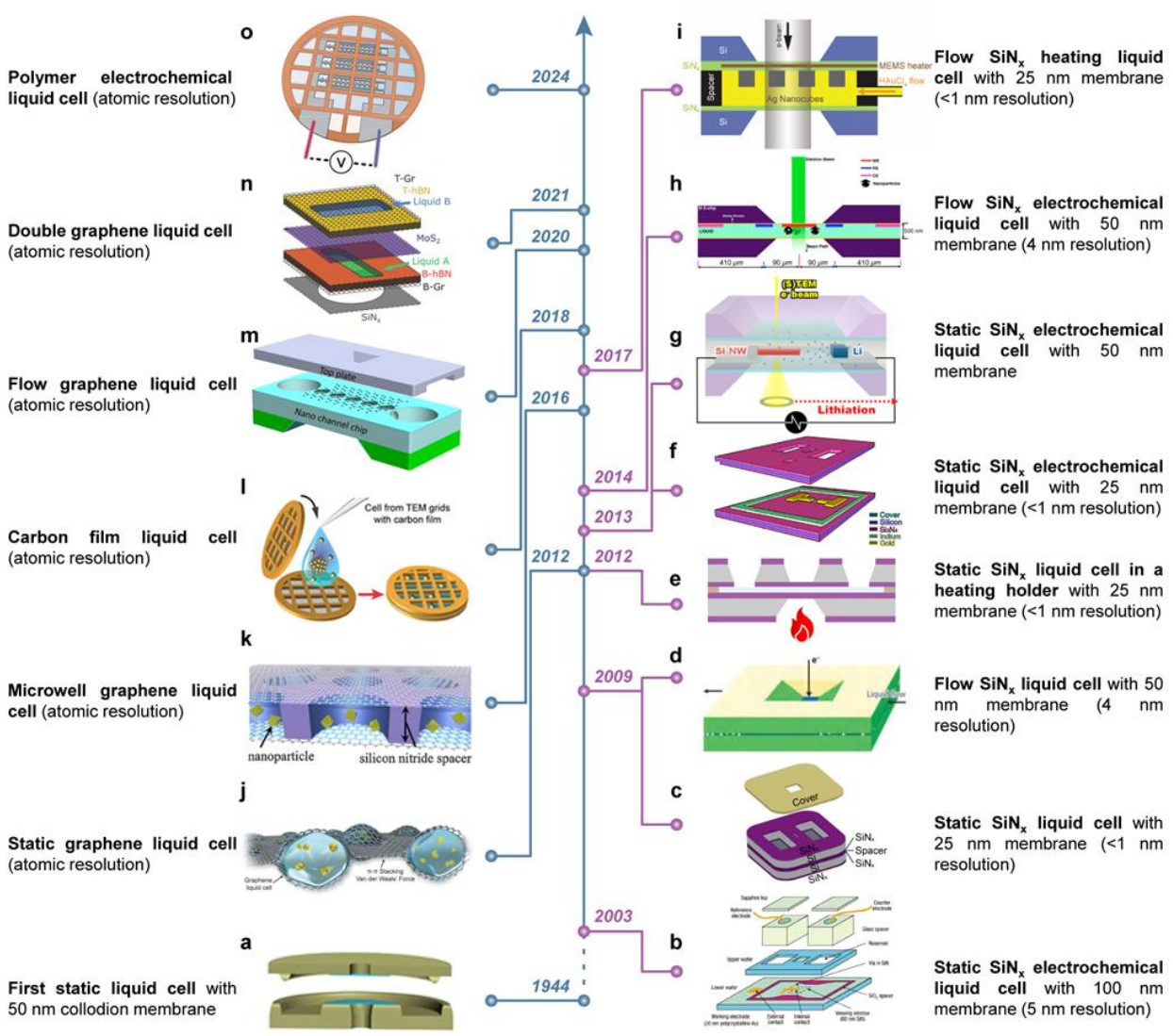

Figure 2.2: Typical designs of liquid cells for *in situ/operando* TEM. (**a**) The first liquid cell using collodion membrane. Reprinted with permission from Reference 1. © 2020 The Materials Research Society. (**b**) A static SiN_x electrochemical liquid cell. Reprinted with permission from Reference 25. © 2003 Springer Nature Limited. (**c**) A high-resolution static SiN_x liquid cell. (**d**) A flow SiN_x liquid cell. Reprinted with permission from Reference 109. © 2022 Elsevier. (**e**) The construct of a liquid cell that can fit into a commercial TEM heating holder. (**f**) A static SiN_x

electrochemical liquid cell. Reprinted with permission from Reference 64. © 2013 Springer Nature. (**g**) A static SiN_x electrochemical liquid cell. Reprinted with permission from Reference 108. © 2013 American Chemical Society. (**h**) A flow SiN_x electrochemical liquid cell. Reprinted with permission from Reference 39. © 2014 American Chemical Society. (**i**) A flow heating SiN_x liquid cell. Reprinted with permission from Reference 33. © 2017 Springer Nature. (**j**) A static graphene liquid cell. Reprinted with permission from Reference 22. © 2017 Wiley. (**k**) A microwell graphene liquid cell. Reprinted with permission from Reference 110. © 2016 Wiley. (**l**) A carbon film liquid cell. Reprinted with permission from Reference 1. © 2020 The Materials Research Society. (**m**) A flow graphene liquid cell. Reprinted with permission from Reference 104. © 2020 American Chemical Society. (**n**) A double graphene liquid cell. Reprinted with permission from Reference 111. © 2021 Wiley. (**o**) A polymer electrochemical liquid cell. Reprinted with permission from Reference 38.

2.2.1 Evolution of SiN_x membrane-based liquid cells

SiN_x is made through wafer-scale micro/nanofabrication techniques (e.g., low-pressure chemical vapor deposition (LPCVD))[113], which enables reliable mass-production of robust SiN_x membranes windows. In 2003, the first static SiN_x electrochemical liquid cell with a two-electrode system was fabricated (**Fig. 2.2b**)[25,114]. The thickness of the SiN_x membranes is 100 nm, resulting in a resolution of 5 nm, which allows for the observation of the electrochemical deposition process of Cu clusters in real-time. Since then, researchers aimed to reduce the membrane thickness and initiated a series of investigations. In 2009, a SiN_x membrane window with a thickness of 25 nm was achieved for a static liquid cell, which successfully improved the spatial resolution to the sub-nanometer level (<1nm), allowing for tracking the dynamic growth of single Pt nanocrystals (**Fig. 2.2c**)[27]. It can also fit into a commercial TEM heating holder for observation of nanoparticle growth at high temperatures (**Fig. 2e**)[30]. Meanwhile, a flow SiN_x liquid cell was created with a resolution of 4 nm to visualize the single molecule in biological cells (**Fig. 2.2d**)[61]. In this liquid cell, the fresh liquid environment was maintained by the continuous exchange between the liquid cell and outside. In 2013, a new generation of electrochemical liquid cell was developed using the 25 nm SiN_x membrane (**Fig. 2.2f**)[64]. This design was equipped with a two-electrode system and revealed the growth of Pb and Li dendrites[66] at high-resolution. In the same year, a similar microdevice was fabricated using a difference electrode design, introducing direct *in situ* observation of lithiation/delithiation of Si nanowires (**Fig. 2.2g**)[108]. In 2014, a flow SiN_x electrochemical liquid cell with a three-electrode system was employed to study the morphological evolution and degradation of Pt-Fe catalysts during ORR (**Fig. 2.2h**)[39]. Besides the development of electrochemical liquid cells, a flow SiN_x heating liquid cell (**Fig. 2.2i**) for studying galvanic replacement reactions of Ag cubes in the $HAuCl_4$ solution was developed in 2017[33], which contained a Mo thin film-based heating chip.

2.2.2 Evolution of 2D membrane-based liquid cells

Another type of membrane is based on graphene or other 2D materials (e.g., hBN, MoS_2), where small pockets of solutions are encapsulated in between through van de Waals force. These ultrathin membranes can significantly reduce electron scattering and improve image contrast. In 2012, a static graphene liquid cell was created based on the entrapment of small droplets of liquid

between two layers of graphene, realizing tracking colloidal nanocrystal growth with atomic resolution (**Fig. 2.2j**)[21]. In 2016, a microwell graphene liquid cell was developed (**Fig. 2.2k**)[110]. The thin SiN_x microwells act as the spacer and container, allowing for a leak-proof confinement of liquids of precise volume while maintaining the benefits of graphene as a viewing window. Similar strategies were also applied in another design[115]. In 2018, a carbon film liquid cell was produced for investigating the ligand-controlled oriented attachment of Au nanoparticles (**Fig. 2.2l**)[115]. This type of liquid cell is easy to fabricate, and therefore drastically reduce the entry barrier for researchers to use *in situ/operando* liquid cell TEM for their studies. In 2020, a flow graphene liquid cell was fabricated, which combines the merits of a SiN_x-based flow cell and a graphene cell (**Fig. 2.2m**)[104]. The nanofluidic channels were produced on the bottom chip, and the hollow cavities acted as the viewing windows. Flow capability was also realized in a different approach[105]. In 2021, a double graphene liquid cell was created, consisting of two adjacent liquid wells. The two liquids were separated by an atomically thin MoS_2 membrane that can be ruptured via local electron beam irradiation, causing liquids to mix (**Fig. 2.2n**)[111]. This design facilitates the visualization of calcium carbonate precipitation as well as tracking single atom motion in liquid[112]. According to the latest studies in 2024, a polymer electrochemical liquid cell was invented to study the structural dynamics of nanomaterials during electrocatalytic processes (**Fig. 2.2o**)[38,70]. This new generation design of electrochemical liquid cell successfully improves the resolution and provides more opportunities for future electron microscopy applications.

2.3 Fabrication and advances of liquid cells

In this section, we will discuss the specific construction and fabrication processes for both categories of SiN_x membrane and 2D membrane-based liquid cells from basic to advanced designs. We will also highlight the integration of multi-field functionalities into liquid cell systems, such as flow, heating, and biasing.

2.3.1 Fabrication of SiN_x membrane-based liquid cells

SiN_x membranes are widely used for liquid cells, which feature robust mechanical properties and compatibility with the microfabrication for commercial production. Previously, thick SiN_x membranes (50~100 nm) were typically used[25], however, making ultrathin freestanding membranes and controlling liquid thickness are some of the key contributions to recent development. The schematic shows the structure of a high-resolution static SiN_x liquid cell (**Fig. 2.3a**)[27]. It contains a bottom chip with a 25 nm thin SiN_x membrane and a top chip with the same window and two liquid reservoirs. The optical image of the assembled liquid cells is shown in **Fig. 2.3b**[100]. This basic design has been continuously used for more applications, such as the electrochemical liquid cell (**Fig. 2.3c** and **d**)[64]. An added step of electrode deposition is needed compared with regular ones, which is able to connect with the biasing TEM holder and potentialstat for electrochemical studies.

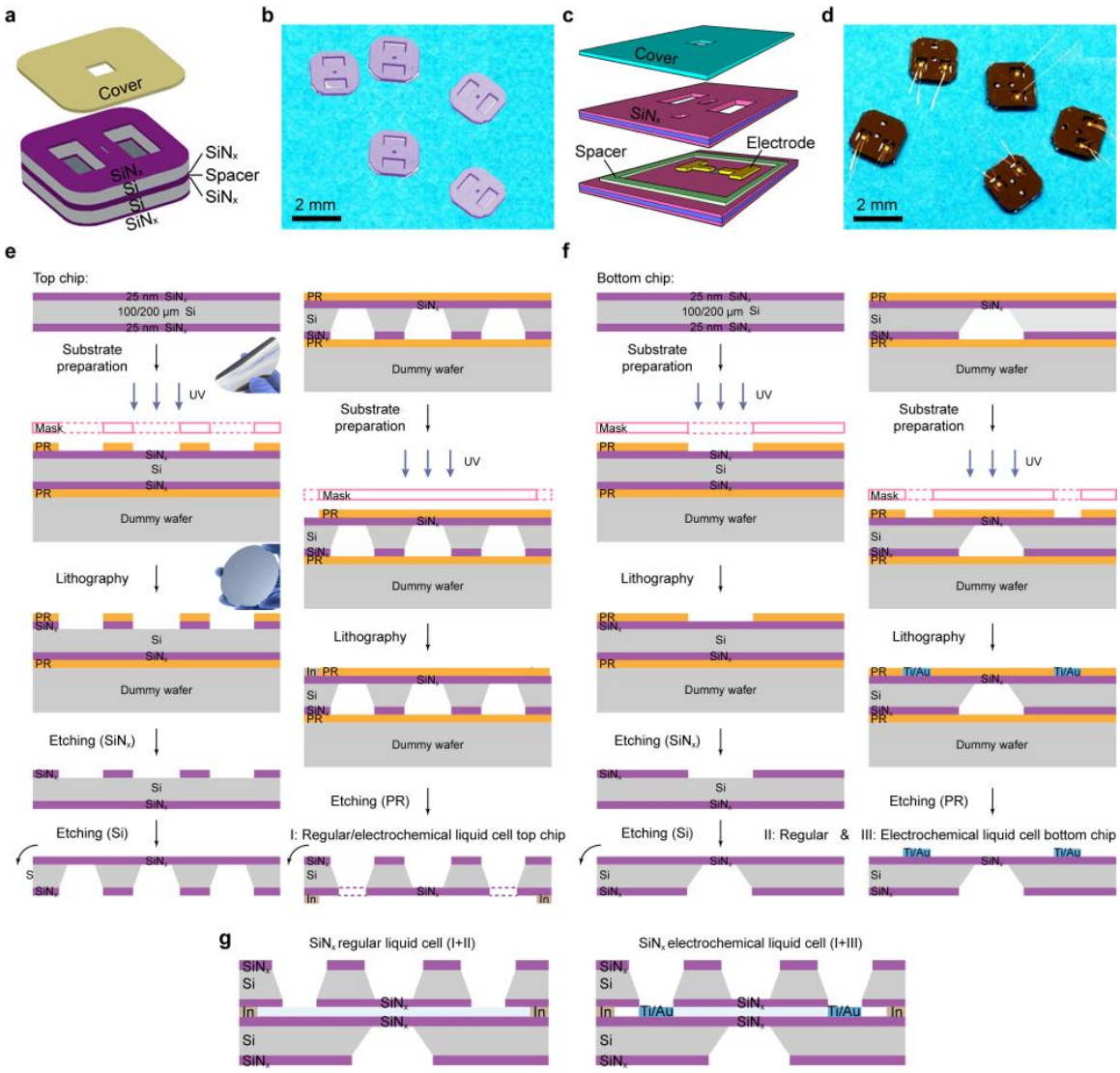

Figure 2.3: Fabrication of SiN_x membrane-based liquid cells. (**a**) Schematic of a static SiN_x liquid cell and (**b**) its optical image. (**c**) Schematic of a static SiN_x electrochemical liquid cell and (**d**) its optical image. (**e**) The fabrication process of a regular/electrochemical liquid cell top and (**f**) bottom chip. (**g**) The assembly of a regular liquid cell and an electrochemical liquid cell. (b) and (d) are reprinted with permission from Reference 100. © 2021 Springer Nature. (c) Reprinted with permission from Reference 64. © 2013 Springer Nature.

The step-by-step micro/nanofabrication processes of a regular static SiN_x liquid cell and an electrochemical liquid cell are shown in **Fig. 2.3e** and **f**. Both liquid cells share similar procedures of separated top and bottom chips fabrication. First, the substrates of both the top and bottom chip consist of a Si wafer (reduced thickness of 100-200 μm for the cell mounting) with ultrathin 25 nm SiN_x membrane grown on both sides. The fragile SiN_x/Si/SiN_x substrates are bonded with a standard 500 μm dummy wafer as protector for further fabrication process. Then, photolithography is performed on the top and bottom chips using different masks, followed by reactive ion etching (RIE) and KOH treatment to selectively remove the patterned SiN_x membrane and Si underneath.

An imaging window and two liquid reservoirs are supposed to be created for the top chip, whereas only one imaging window is designed for the bottom chip. The membrane of the viewing windows is kept intact and that of reservoirs can be physically destroyed for later liquid injection. After wet etching, an In spacer (70-100 nm) is needed on the top (or bottom) chip to control liquid thickness, while metal electrodes (Ti or Au) are incorporated onto the bottom chip only for the electrochemical liquid cell. For this purpose, additional photolithography is performed to create patterns for metal deposition through physical vapor deposition (PVD) (e.g., sputtering, evaporation).

Finally, the top and bottom chips can be aligned and assembled into a whole (regular or electrochemical) liquid cell (**Fig. 2.3g**). A heat treatment is needed for In spacer melting and re-solidification to bind top and bottom chips together. Also, epoxy is evenly coated all around the sides of the liquid cell to prevent liquid leakage.

2.3.2 Advances of SiN_x membrane-based liquid cells

Although SiN_x membrane has been widely used for liquid cells, several challenges remain to be addressed. Most notably, the thickness of the SiN_x membrane significantly limits resolution and quantitative analysis. To overcome this issue, researchers have reduced the thickness of the SiN_x window from 100 nm to 10 nm. As illustrated in **Fig. 2.4a**, an ultrathin 10 nm SiN_x membrane was recently developed, where surrounded a Si frame to maintain its superior mechanical integrity[116]. In the fabrication process, Si substrate was selectivity etched into a honeycomb pattern by employing a dopant-dependent method (**Fig. 2.4b**). Moreover, the small imaging window of SiN_x membrane-based liquid cells reduces experimental reproducibility. To address this problem, an approach for expanding the imaging area was introduced, allowing people collect multiple datasets from a single device. This liquid cell creates a 5×5 array of windows, 25 times larger than conventional chips (**Fig. 2.4c** and **d**)[117] and its fabrication process is shown in **Fig. 2.4e**. Bulging of SiN_x membranes is another common problem for liquid cell TEM, which drastically reduces resolution and limits the usable viewing area. To mitigate this issue, a bulge-free SiN_x liquid cell was developed. It was sealed with an internal O-ring that encapsulated the liquid and formed a cavity around the central pillar, accommodating excess liquid upon closure (**Fig. 2.4f** and **g**)[118]. The thickness of pure water inside such liquid cell indicates minimal membrane bulging (**Fig. 2.4h**). Furthermore, a direct wafer bonding process has been used to replace assembly of top and bottom chips, enabling the integration more complex liquid cell designs with reliable bonding quality and the potential for mass production. For example, parylene was utilized as both the bonding layer and nanofluidic channels (**Fig. 2.4i**)[119].

For real-time probing material dynamics under complex electrochemical reactions, fabrication of electrochemical liquid cells for *in situ/operando* TEM has attracted great attention. A flow SiN_x electrochemical liquid cell was demonstrated with a patterned three-electrode configuration, featuring a glassy carbon working electrode, along with Pt reference and counter electrodes (**Fig. 2.4j**)[120]. Meanwhile, various liquid cell designs with distinctive electrode configurations have been made for studying a wide range of electrochemical systems (**Fig. 2.4k** and **l**)[74,121–124], particularly in the field of electrocatalysis, such as CO_2RR[38,70–72,96,125,126],

HER[127,128], OER[36,74,129], and ORR[39,130]. Batteries in electrolyte are also studied in both closed cells[66,67,69,108,124] and open cells[131,132].

Lately, the combination of temperature control was realized within an electrochemical liquid cell (**Fig. 2.4m**)[107,133], which is critical for studying electrochemical processes at certain working conditions (e.g., batteries at extreme temperatures[134,135], industrial electrocatalysis[2,136,137]). In order to enhance the resolution of SiN_x liquid cell for electrochemical quantification, multilayer graphene has been exploded as promising electrode, offering a significantly low-contrast imaging compared with traditional Pt and other metal electrodes (**Fig. 2.4n**)[138]. The exfoliated graphene was transferred onto the existing Pt electrodes of liquid cell chips with enhanced cleanness through a cellulose acetate butyrate (CAB)-assisted method (**Fig. 2.4o**).

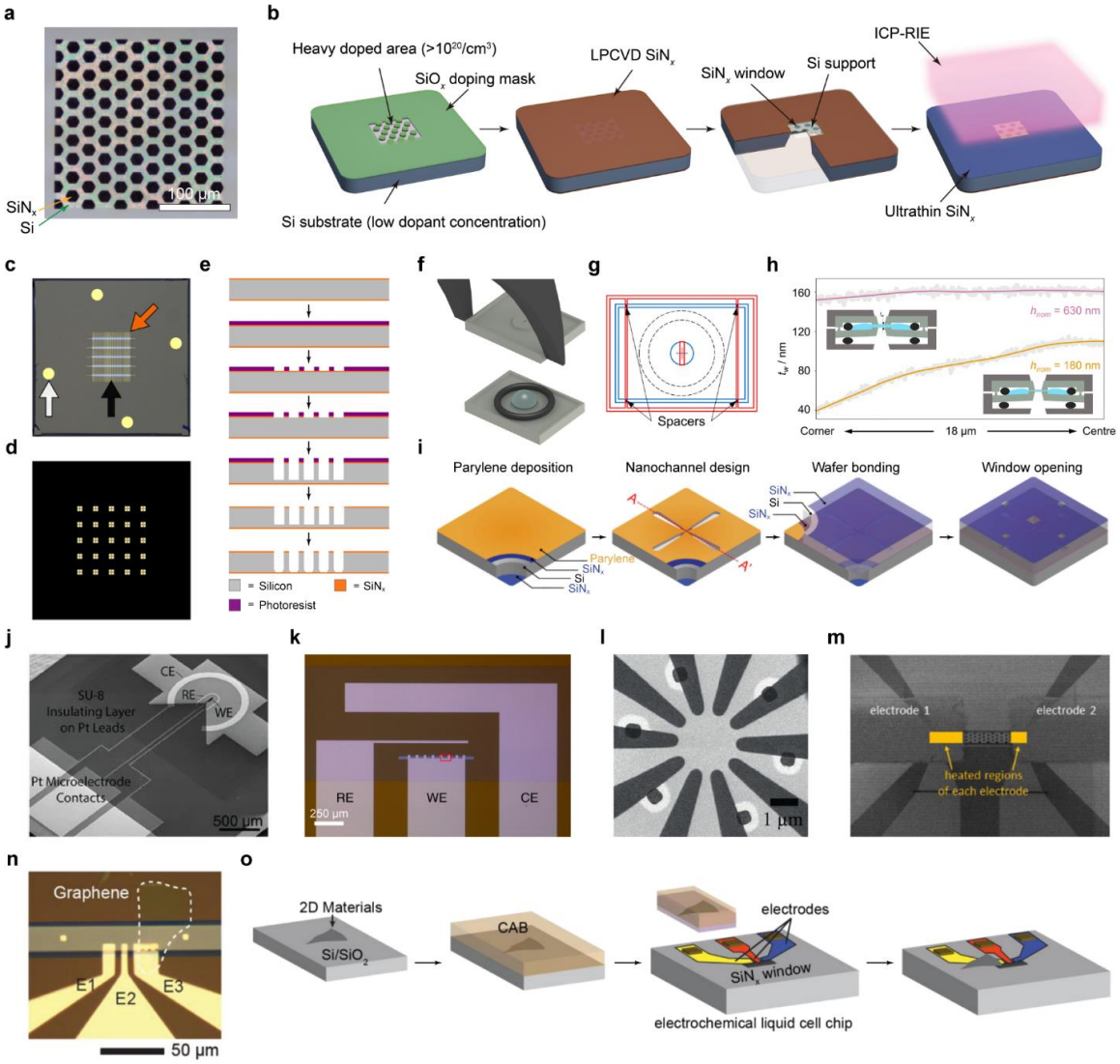

Figure 2.4: Advances of SiN_x membrane-based liquid cells. (**a**) Optical image of an ultrathin SiN_x membrane and (**b**) its fabrication process. (**c**) A flow SiN_x liquid cell chip with Au grid bars.

(**d**) Illustration of available imaging area in the assembled liquid cell and (**e**) its fabrication process. (**f**) Schematic of a bulge-free SiN_x liquid cell and (**g**) its projected view after assembly. (**h**) Quantification of the water layer thickness from the edge to the center of the viewing area. (**i**) Fabrication process of wafer bonding. (**j-l**) SiN_x electrochemical liquid cells with different electrode configurations. (**m**) A heating SiN_x electrochemical liquid cell. (**n**) A SiN_x electrochemical liquid cell with a transferred graphene on Pt electrode and (**o**) its fabrication process. (a-b) Reprinted with permission from Reference 116. © 2024 AAAS. (c-e) Reprinted with permission from Reference 117. © 2018 AAAS. (f-h) Reprinted with permission from Reference 118. © 2023 Royal Society of Chemistry. (i) Reprinted with permission from Reference 119. © 2017 IOP Publishing Ltd. (j) Reprinted with permission from Reference 120. © 2014 Microscopy Society of America. (k) Reprinted with permission from Reference 74. © 2021 Springer Nature. (l) Reprinted with permission from Reference 121. © 2015 IEEE. (m) Reprinted with permission from Reference 133. © 2020 Microscopy Society of America. (n-o) Reprinted with permission from Reference 138. © 2021 Wiley.

2.3.3 Fabrication of 2D membrane-based liquid cells

Graphene is a representative material for 2D membrane-based liquid cell, which exhibits high thermal and electrical conductivity, outstanding mechanical strength, and chemical inertness[139,140]. A monolayer or a few layers of a hexagonal carbon lattice can significantly reduce electron scattering and contrast loss, making it suitable for *in situ/operando* TEM with atomic resolution[21]. For a static graphene liquid cell, the strong van der Waals interaction encapsulates liquid pockets between two graphene sheets (**Fig. 2.5a**)[21,22]. To prepare it, two TEM grids with transferred graphene are first superimposed, and then a droplet of the solution is placed on the top. After removing the extra solution, the remaining liquid is drawn into small pockets between the graphene layers. Later, the top TEM grid is removed by chemical etching (**Fig. 2.5b**)[101]. Since graphene transfer and liquid cell assembly requires careful operations, several approaches have been developed to enhance the fabrication yields. For example, the liquid sample can be firstly placed on a SiN_x support film and coated with a graphene layer (**Fig. 2.5c**)[141]. This graphene-SiN_x hybrid liquid cell increased the stability of supporting liquid and reduced the difficulty of handling graphene films. In addition, a loop can be used to assist manipulating graphene sheets on a liquid droplet (**Fig. 2.5d**)[142,143]. The confined geometry substantially reduces liquid convection and facilitate the positioning of graphene onto the sample. Moreover, a sacrificial polymer layer, such as poly (methyl methacrylate) (PMMA)[144] or CAB (**Fig. 2.4o**)[138] can be applied to reduce the mechanical strain of graphene when transferring it onto the liquid surfaces. According to a recent study, the graphene TEM grids can even be fabricated without a transfer process. A large-area and continuous graphene was grown on a Cu foil followed by directly etching the backside into arrayed grids through photolithography. After rinsing and drying, the graphene membranes were suspended on the spaced holes with an ultraclean surface (**Fig. 2.5e**)[145].

Random formation of liquid pockets between membranes impedes control and prediction of liquid volume, location, and thickness, which makes the system more complex and heterogenous. A microwell graphene liquid cell has been fabricated, which intentionally confined liquid inside artificial cavities[110,115] (**Fig. 2.5f** and **g**).In the fabrication procedure, spacers (hBN or SiN_x) patterned in microwells were first obtained through exfoliation, photolithography, and

reactive ion etching. Then, the graphene sheets were transferred onto both side of the spacer, while a liquid sample is introduced in between (**Fig. 2.5h**)[115]. Another approach to improve controllability and repeatability of graphene liquid cell is producing nanofluidic channels for liquid (**Fig. 2.5i** and **j**)[104,105]. The flow graphene liquid cell combines the benefits of a flow SiN_x liquid cell and a static graphene liquid cell. One strategy is depositing a patterned Pt spacer serving as the flow channel between graphene sheets (**Fig. 2.5k**)[105] and another is making hollow cavities across a single chip performing as both nanofluidic channels and imaging windows (**Fig. 2.5i**)[104]. Innovatively, a double graphene liquid cell was designed to encapsulate two different liquids between stacked graphene and MoS_2 layers. A crack can be created throughout the middle MoS_2 membrane under local electron beam irradiation, allowing mixing of the two liquids and capturing the early stages of reaction *in situ* (**Fig. 2.5l**)[111]. To fabricate the double graphene cell, a monolayer MoS_2 is first transferred onto a graphene-hBN stack, adding a droplet of the liquid in between. Then, a second graphene-hBN stack is similarly transferred with hBN-side down onto the MoS_2, packaging another type of liquid (**Fig. 2.5m**)[111,112].

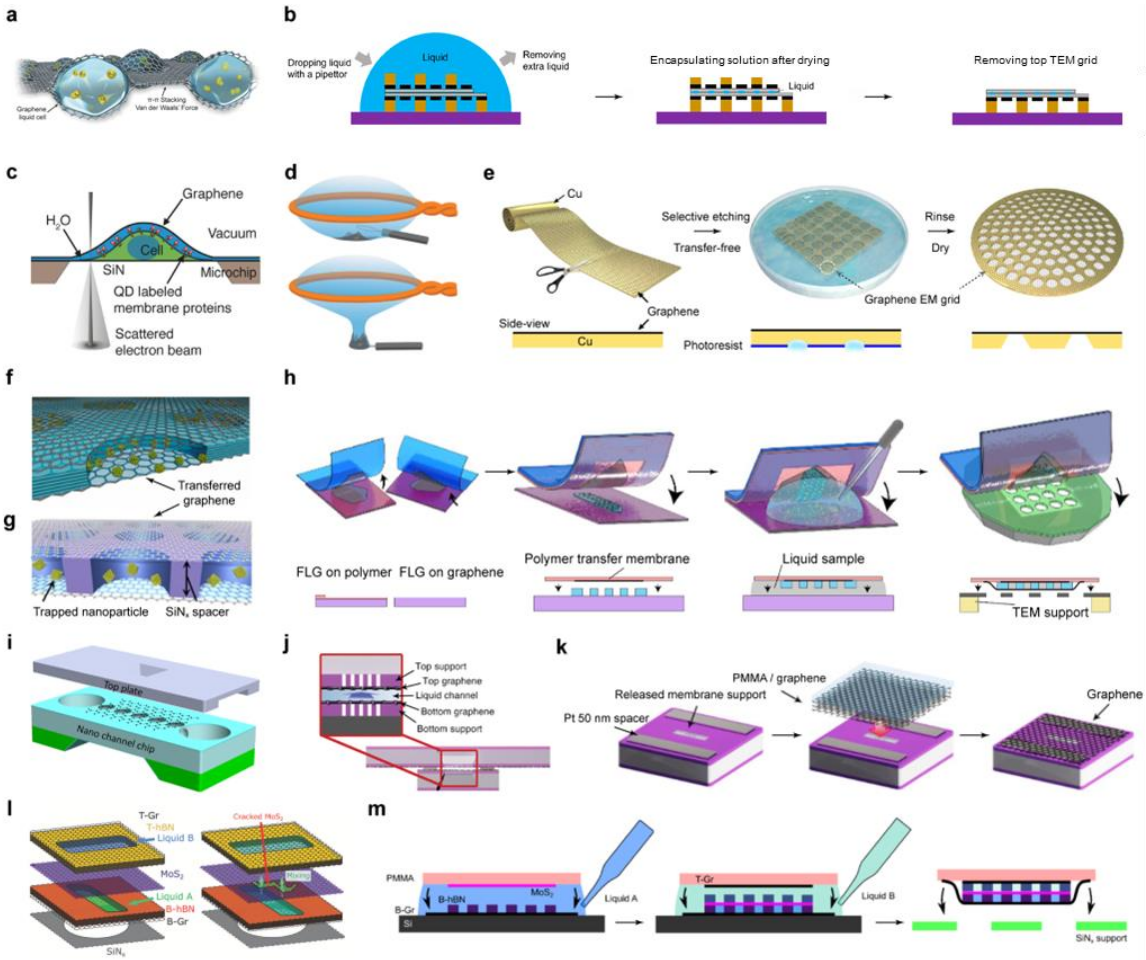

Figure 2.5: Fabrication of graphene-based liquid cells. (**a**) Schematic of a static graphene liquid cell and (**b**) its fabrication process. (**c**) Schematic of a graphene-SiN_x hybrid liquid cell. (**d**) A loop-assisted graphene transfer method for liquid cell assembly. (**e**) Fabrication process of large-scale

graphene TEM grids. (**f-g**) Schematics of microwell graphene liquid cells using (**f**) hBN and (**g**) SiN_x as the spacer. (**h**) Fabrication process of a microwell graphene liquid cell. (**i**) Schematic of a flow graphene liquid cell. (**j**) Schematic of a flow graphene liquid cell and (**k**) its fabrication process. (**l**) Schematic of a double graphene liquid cell before and after liquid mixing and (**m**) its fabrication process. (a) Reprinted with permission from Reference 22. © 2017 Wiley. (b) Reprinted with permission from Reference 101. © 2023 American Chemical Society. (c) Reprinted with permission from Reference 141. © 2017 American Chemical Society. (d) Reprinted with permission from Reference 142. © 2013 IUCr. (e) Reprinted with permission from Reference 145. © 2020 Springer Nature. (f) and (h) are reprinted with permission from Reference 115. © 2018 American Chemical Society. (g) Reprinted with permission from Reference 110. © 2016 Wiley. (i) Reprinted with permission from Reference 104. © 2020 American Chemical Society. (j-k) Reprinted with permission from Reference 105. © 2020 Wiley. (l-m) Reprinted with permission from Reference 111. © 2021 Wiley.

2.3.4 Advances of 2D membrane-based liquid cells

Currently, diverse types of 2D membranes have been developed as the liquid cell window materials. First, liquid cells can be assembled using commercial TEM grids with thin amorphous carbon film, which largely simplified the fabrication processes and lowered the entry barrier for *in situ/operando* liquid cell TEM studies. To prepare a carbon film liquid cell, a droplet of solution is sandwiched by two TEM grids and then left under atmosphere until the extra liquid volatized and later transferred into the TEM (**Fig. 2.6a**)[34]. Moreover, some other 2D materials can offer unique advantages when they are used in a liquid cell. For example, MoS_2 can be served as a functional substrate as well as the membrane window of liquid cell for the study of heterostructures growth of nanoparticles (**Fig. 2.6b**)[146]. A polymer-free MoS_2 transfer process was proposed, including steps of MoS_2 preparation on SiO_2/Si wafer through CVD, attachment of TEM grids onto the MoS_2 sheets, and the selective etching of the SiO_2 layer using HF solution (**Fig. 2.6c**). In addition, hBN liquid cell provides the ability to study the vibrational spectroscopy of water with high spatial resolution (**Fig. 2.6d**)[147]. The fabrication of hBN liquid cells can be achieved by simply touching the lacey carbon-coated side of the grid to a floating piece of hBN.

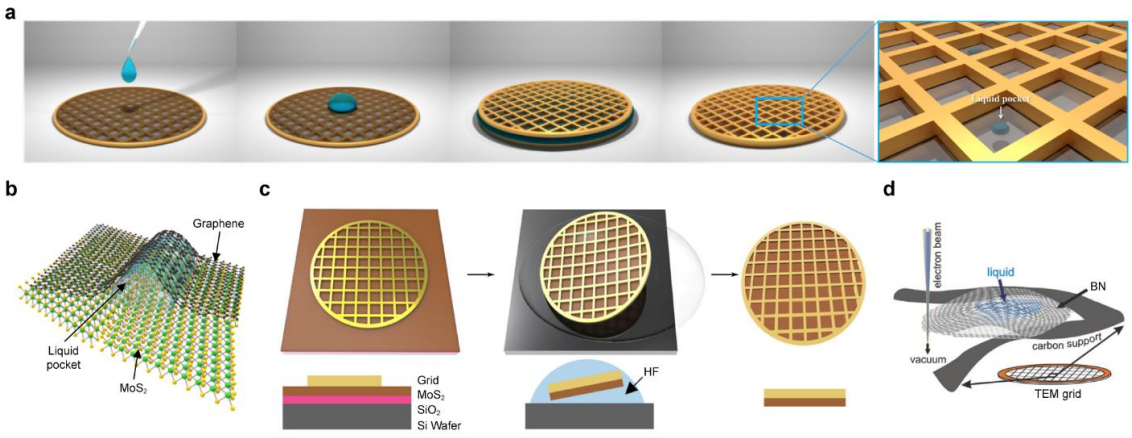

Figure 2.6: Advances of 2D membrane-based liquid cells. (**a**) The fabrication process of a carbon film liquid cell. (**b**) Schematic of a MoS_2 liquid cell. (**c**) The HF-assisted transferring process of MoS_2 membrane. (**d**) Schematic of an hBN liquid cell. (a) Reprinted with permission from Reference 34. © 2018 Springer Nature. (b-c) Reprinted with permission from Reference 146. © 2019 American Chemical Society. (d) Reprinted with permission from Reference 147. © 2018 Wiley.

For control and observation of nanoscale reactions, nanoreactors can be introduced into a liquid cell. Recently, gold-coated liposome nanocapsules were used as nanoreactors to study the nanobubbles generation process through water radiolysis (**Fig. 2.7a**)[148], allowing for *in situ* mixing and precise control of reagent in volumes and concentrations. To construct nanocapsules inside liquid cell, a thin layer of liposome sample was sandwiched between two TEM grids with amorphous film. The grids were then treated with ultraviolet ozone cleaning, followed by adding the liposome-containing sample. Most of the liquid is then wiped away, leaving a thin layer of the liposome. A second TEM grid was finally placed on the top, creating a sandwiched structure that encapsulated liquid sample (**Fig. 2.7b**).

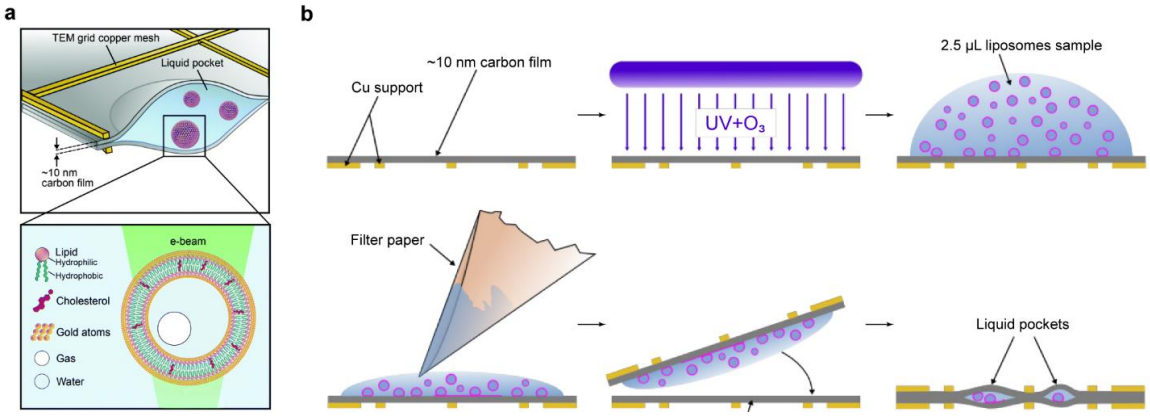

Figure 2.7: **Nanoreactors inside liquid cells.** (**a**) Schematic of Au-coated liposome nanocapsules for liquid cell TEM and (**b**) the fabrication process. Reprinted with permission from Reference 148. © 2020 Royal Society of Chemistry.

2.4 Understanding liquid behaviors within liquid cells

Understanding the physical and chemical properties of liquid inside a liquid cell is important not only for the experimental purpose, but also for the improvement of instrumental design. Therefore, theoretical and experimental approaches have been developed for mapping thickness, temperature, diffusion, and current distribution within liquid cells. For mapping and controlling liquid layer thickness, a model SiN_x liquid cell with a budging window has been studied (**Fig. 2.8a** and **b**)[149]. The liquid thickness can be determined through a mass-thickness contrast (MTC) method (**Fig. 2.8c**) or using EELS for estimation (**Fig. 2.8d**). In addition, the temperature

profile of a heating liquid cell with a Mo microheater (**Fig. 8e**)[33,150] can be obtained by finite element model (FEM) simulations (**Fig. 2.8g**) and luminescence intensity mapping of Er^{3+}/Yb^{3+}-doped nanoparticles after applying corrections (**Fig. 2.8f** and **h**). Moreover, a contrast variation method was used to track the liquid transportation velocity inside a flow cell (**Fig. 2.8i**)[151]. The time-dependent concentration curves in **Fig. 2.8j** show the improved solution replacement with a diffusion cell design based on the experimental results. As for electrochemical liquid cells, FEM simulations were performed on two distinctive electrode geometries (**Fig. 2.8k** and **l**)[152]. An inhomogeneous current distribution was observed in the first design, while the second one produced a more uniform current distribution, indicating the design and geometry of electrochemical chips is essential for reliable measurements in liquid cells.

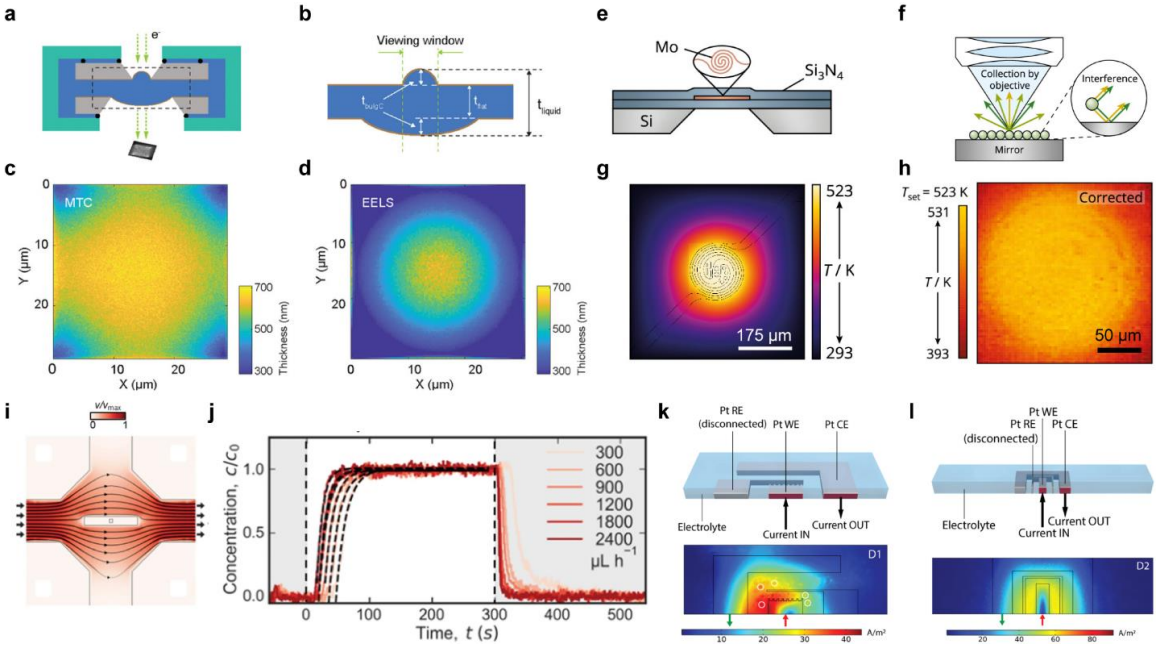

Figure 2.8: **Understanding the physical and chemical properties of liquids inside liquid cells.** Schematic of (**a**) a model SiN_x liquid cell and (**b**) its bulging region. Liquid layer thickness map obtained from (**c**) the mass-thickness contrast method and (**d**) EELS measurements. (**e**) Schematic of a microheater SiN_x chip. (**f**) Schematic of luminescence method for temperature detection. (**g**) Simulated temperature profile and (**h**) the corrected temperature map obtained by the luminescence results. (**i**) Liquid velocity mapping in a flow liquid cell. (**j**) Time-dependent concentration curves. (**k-l**) Simulated current density of the electrolyte for electrochemical liquid cells. (a-d) Reprinted with permission from Reference 149. © 2021 Wiley. (e-h) Reprinted with permission from Reference 150. © 2021 American Chemical Society. (i-j) Reprinted with permission from Reference 151. © 2024 Springer Nature. (k-l) Reprinted with permission from Reference 152. © 2021 IOP.

2.5 Development of polymer membrane-based electrochemical liquid cells for *in situ/operando* TEM studies on electrocatalysis

With the growing world population and expanding industrialization, the over-reliance on fossil fuels brings human crucial challenges of energy shortage, environmental pollution and climate change[153]. In the face of these threats, it is of global importance to develop sustainable, fossil-free pathways to produce fuels and chemicals we use on daily basis. One prospective way is to develop electrochemical conversion processes to convert molecules in the atmosphere into higher-value products through electrocatalysis using abundant renewable electricity[19]. The electroreduction of carbon dioxide helps close the carbon cycle and supplies value-added chemicals[154]. Additionally, the water splitting reaction generates hydrogen and oxygen which can be used to produce clean electricity in fuel cells[155].

Electrocatalysts play a key role in electrocatalytic CO_2RR as well as water splitting reaction. Reactions take place at the active sites on the surface of electrocatalysts, and thus, catalyst structure largely determines activity and selectivity of relevant chemical transformations[156]. Under the influence of electrolyte and applied bias, electrocatalysts often undergo structural transformations, including change of particle size, element distribution or morphology, which are reflected in their evolving catalytic performance[157–160]. Therefore, a fundamental understanding of the dynamic phenomena of electrocatalysts is vital for scientific design of better catalytic materials. One promising way to track these dynamic behaviors is through *in situ/operando* characterization[83]. *In situ* X-ray absorption spectroscopy (XAS)[93,161,162], *in situ* XRD[163], and *in situ* Raman spectroscopy[164] have been employed to study dynamic processes of electrocatalysts. However, spectroscopies reflect average information rather than specific situation of local positions, incapable of probing spatial information of an identical nanocatalyst at the atomic level.

Recently, *in situ/operando* EC-TEM has been applied for capturing morphological evolution and phase transformation of electrocatalysts[73,93–95]. This technique is capable for direct investigation of structural dynamics occurring on nanoparticles within the electrolyte in real time, which provides valuable information assisting the fundamental understanding of underlying mechanisms and catalysts design. However, the current electrochemical liquid cell TEM techniques have poor spatial resolution due to the thick membrane, limiting our understanding of electrocatalysts dynamics under operation condition.

Here, we developed the high-resolution polymer membrane-based electrochemical liquid cells to study the dynamic phenomena of electrocatalysts during electrocatalytic reactions at the atomic level.

2.5.1 Fabrication of two-electrode polymer membrane-based electrochemical liquid cells

The polymer membrane-based electrochemical liquid cells are built with a bottom and a top chip capsuling the multiple liquid pockets in between. The bottom and top chips are fabricated based on the commercial Cu or Au TEM grids (200 square mesh, Electron Microscopy Sciences). The grids are first coated with 250 nm of electrically insulating aluminum oxide (Al_2O_3) by sputter deposition (AST-sputter, Berkeley Marvell NanoLab). Subsequently, a 10 nm-thick insulating polymer (0.25% Formvar solution in 1,2-dichloroethane (≥99.0%, Sigma-Aldrich)) film is transferred onto the grids. Then, 10 nm-thick Pt interdigital electrodes are deposited onto the bottom chips using the e-beam evaporation (Semicore-evaporator, Molecular Foundry, LBNL)

through a specially designed shadow mask, enabling electrochemical reaction in the micro-electrochemical system (**Fig. 2.9**).

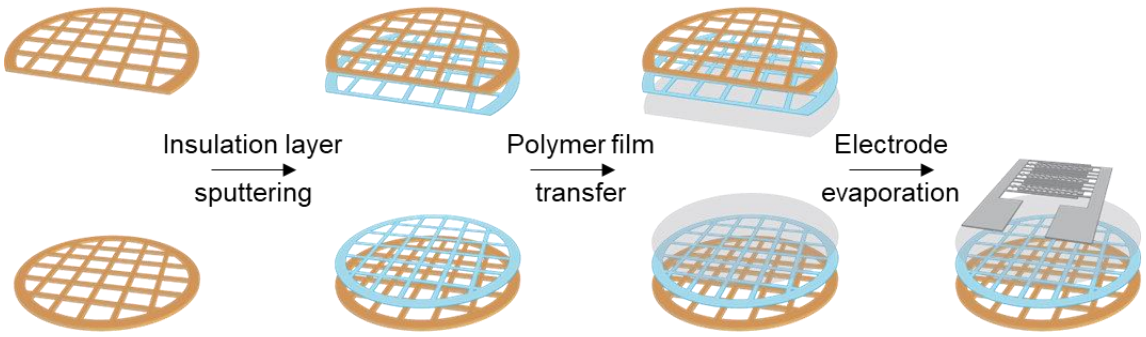

Figure 2.9: Fabrication process of the polymer membrane-based electrochemical liquid cells.

2.5.2 Characterization of polymer membrane-based electrochemical liquid cells

The electrode configuration design for a polymer membrane-based liquid cell is shown in **Fig. 2.10a** with a two-electrode system. The interdigital electrodes enable electrochemical reactions inside the liquid pockets. The different shape design of the working electrode (WE) and counter electrode (CE) makes it possible to distinguish between them during *in siu/operando* TEM imaging. The optical microscopy image of an electrochemical liquid cell bottom chip is shown in **Fig. 2.10b**, indicating uniform covering of polymer membrane and well deposition of electrodes. The grids are 3.05 mm in diameter.

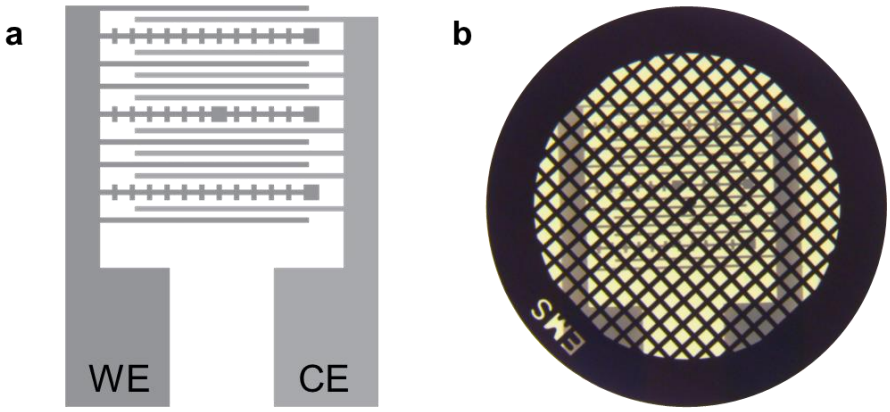

Figure 2.10: Characterization of two-electrode polymer membrane-based electrochemical liquid cells. (**a**) Electrode configuration design for a polymer membrane-based liquid cell. (**b**) Optical microscopy image of an electrochemical liquid cell bottom chip.

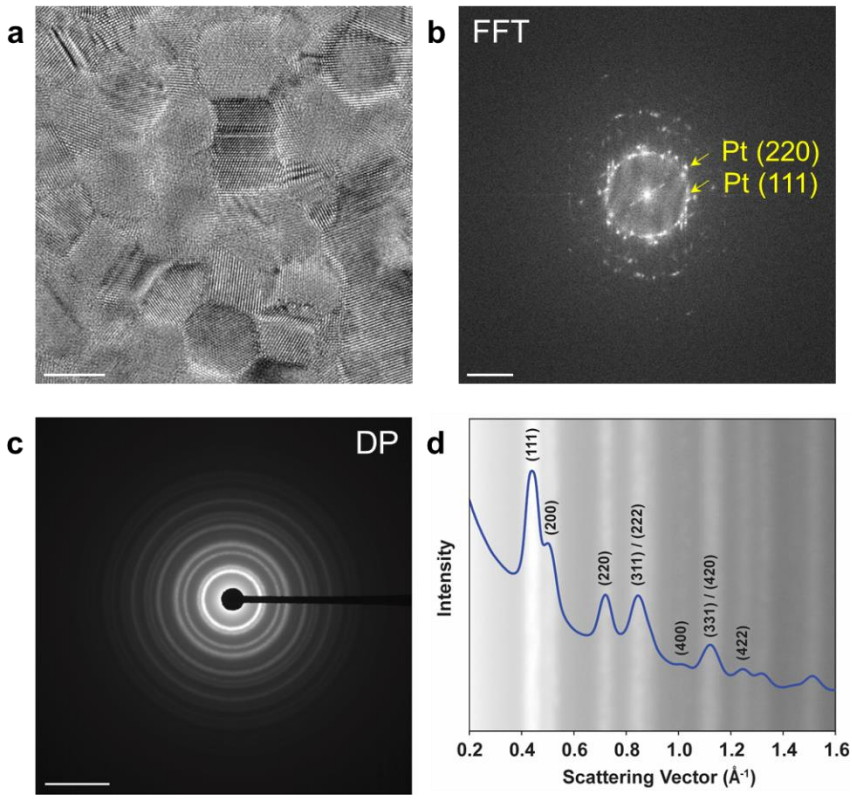

Figure 2.11: Characterizations on the Pt electrodes for polymer membrane-based liquid cells. (**a**) HRTEM image of 10 nm thick Pt electrodes. Scale bar, 5 nm. (**b**) Corresponding FFT pattern of (a). Scale bar, 5 nm^{-1}. (**c**) DP of the Pt electrodes and (d) corresponding radial RDF.

Characterizations on the Pt electrodes for polymer membrane-based liquid cells are shown in **Fig. 2.11**. High-resolution TEM (HRTEM) image of the10 nm thick Pt electrodes shows polycrystalline Pt structure with good connectivity. Corresponding fast Fourier transform (FFT) pattern of with marked spots correlated to the Pt (111) and Pt (220). Electron diffraction pattern (DP) of the Pt electrodes and corresponding radial distribution function (RDF) match with the polycrystalline Pt structure.

2.5.3 Operation of polymer membrane-based electrochemical liquid cells

When performing *in situ/operando* EC-TEM experiments, the catalysts are first drop-cast onto the bottom chip of liquid cell. Then, 1 μL of electrolyte is added onto the bottom chip. Finally, the bottom chip is covered by the top chip, completing the liquid cell assembly. Multiple liquid pockets are able to form inside the liquid cell. The liquid cell is able to connect with the electrical biasing TEM holder and potentiostat for further electrochemical measurements. As shown in the illustration, the electrochemical liquid cell is mounted on a Hummingbird Scientific electrical biasing holder (**Fig. 2.12**). The enlarged part shows the tip of the holder, where the electrochemical liquid cell is connected with the holder with silver conducting paste on a home-made contact board. The cell is fixed by a copper clamp.

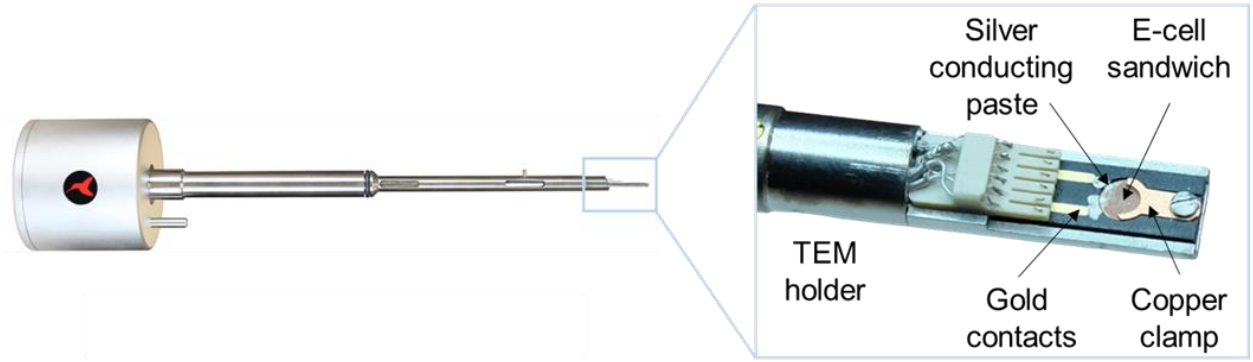

Figure 2.12: Illustration of the TEM holder and its connection between the liquid cell.

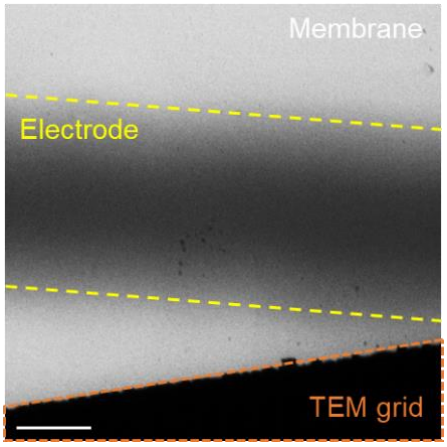

Figure 2.13: **TEM image of a local area inside an electrochemical liquid cell during EC-TEM experiments.**

TEM image shows a local area inside an electrochemical liquid cell during EC-TEM experiments (**Fig. 2.13**). Different regions with different contrasts are marked as TEM grid, electrode, and membrane, respectively. This new design of electrochemical liquid cell provides a large viewing window for the EC-TEM observations.

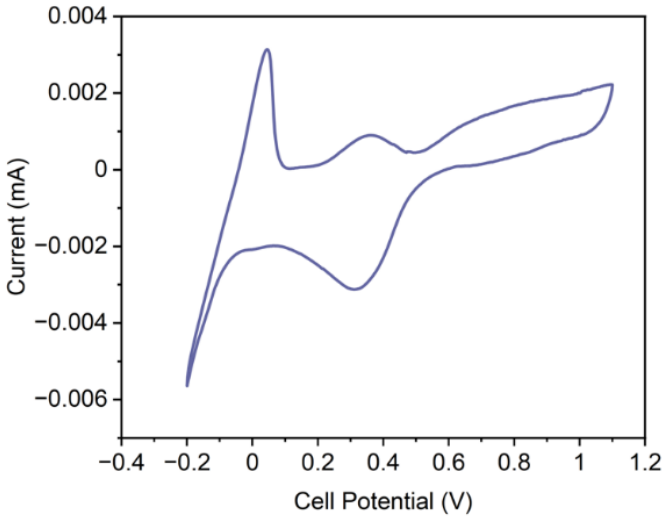

Figure 2.14: **CV profile of commercial Pt nanoparticles loaded in the EC-TEM liquid cell in 0.1 M $HClO_4$ electrolyte.**

The cell potential is calibrated by the underpotential deposited hydrogen peak in 0.1 M perchloric acid in the electrochemical liquid cell[165], indicating -0.28 V vs. Pt is correlated to 0 V vs. standard hydrogen electrode (SHE) (**Fig. 2.14**). This new electrochemical liquid cell design benefits from a thin polymer membrane, enabling observation of materials inside TEM at atomic resolution. It can also provide possibility for elemental composition analysis, including EDS and EELS. Therefore, this new polymer-membrane-based electrochemical liquid cell can meet all required conditions for electrocatalytic reactions, which is suitable for studying the dynamic phenomena of electrocatalysts.

2.5.4 Fabrication of three-electrode polymer membrane-based electrochemical liquid cells

The electrochemical liquid cell with two-electrode system enables the measurement of electrocatalytic reactions, however, its counter-electrode potential may drift over the course of the experiment, which limits the stability and reproducibility. The three-electrode system which comprises a reference electrode (RE) allows for a specific reaction to be studied with confidence and accuracy[166]. RE acts as a reference in measuring and controlling the WE without passing any current, which is commonly used in electrochemical experimentation[167].

Ag/AgCl is commonly used as the reference electrode material in the bulk electrochemical system because of its stable and reproducible potential, non-polarizability, corrosion resistance in chloride environments, and cost-effectiveness. However, when operating at the nano/microscale, the fabrication process becomes challenging. Therefore, Cu, Pt, and Au are usually chosen as the nano/microscale pseudo reference electrodes. Nevertheless, several limitations exist for their application during electrochemical process. Frist, these electrodes are lack of the thermodynamic equilibrium; therefore, one cannot calculate their potential. Second, because these are not ideally

nonpolarizable electrodes, there is a shift of their potential during the measurements, which depends on the current density applied. Third, most pseudo-reference electrodes work over a limited range of conditions such as pH or temperature; outside of this range the electrodes' behavior becomes unpredictable.

Hence, we design and fabricated the polymer membrane-based electrochemical liquid cell with three-electrode system using Ag/AgCl as the reference electrode. Similar as the two-electrode electrochemical liquid cell design, the three-electrode one contains bottom and top chips, both of which involves the deposition of insulating layer and polymer membrane transfer process (**Fig. 2.15a and b**). Differently, a multi-step deposition method was employed for the three-electrode pattern fabrication. Ag was deposited onto the bottom chip as the first layer of RE and Pt was then deposited as both WE and CE through two specially designed shadow masks. Finally, the Ag/AgCl electrode was obtained by chemical oxidation chlorination of Ag using $FeCl_3$ solution (**Fig. 2.15b**).

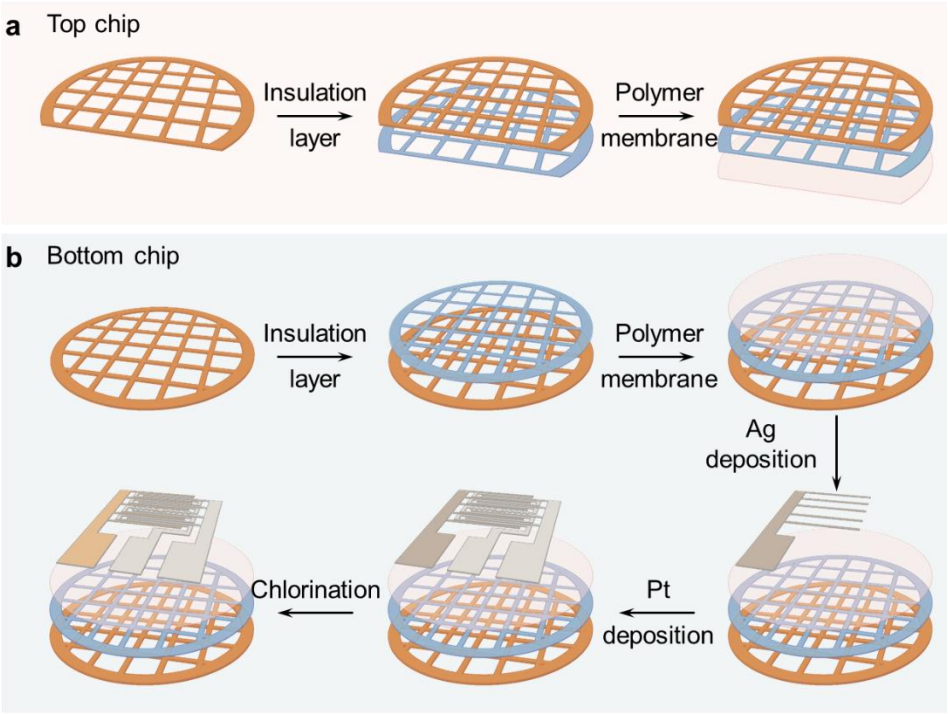

Figure 2.15: Fabrication process of three-electrode polymer membrane-based electrochemical liquid cells. (**a**) A top chip workflow and (**b**) a bottom chip workflow.

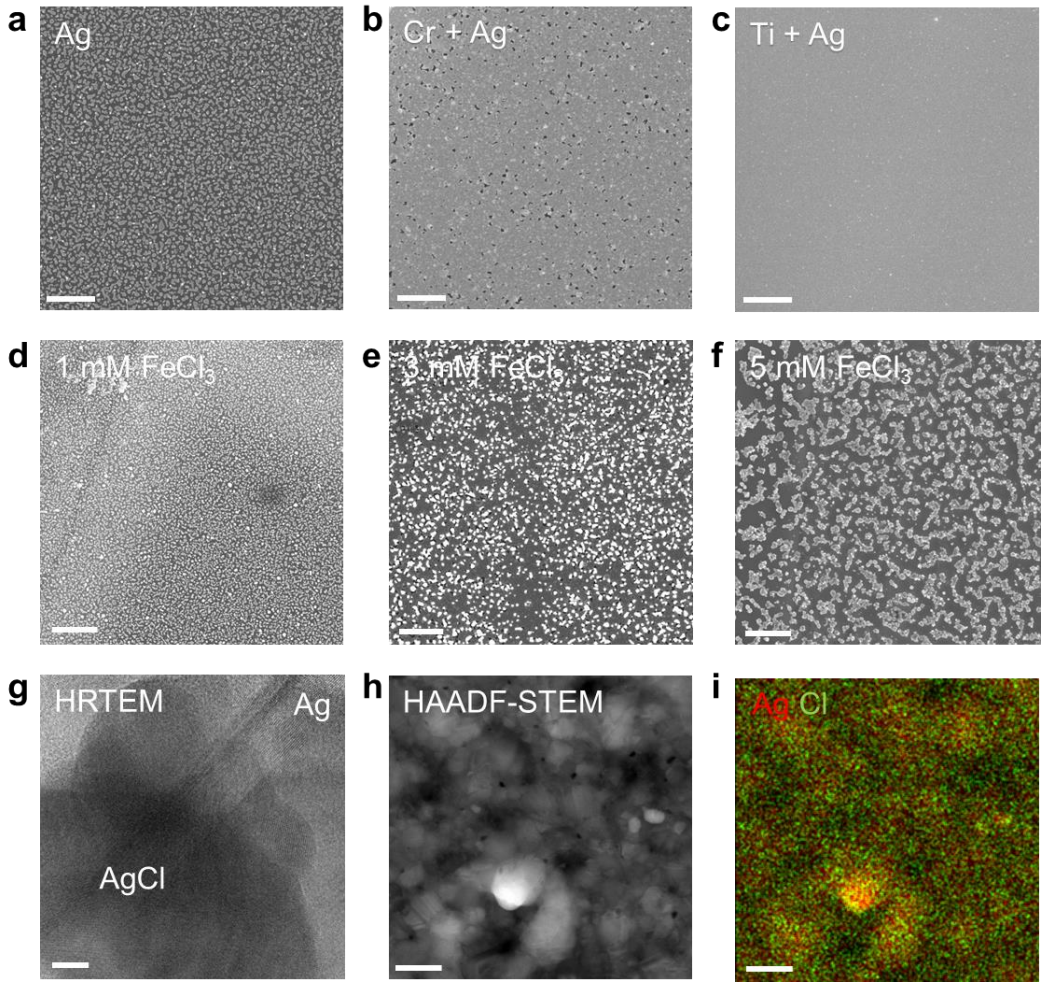

Figure 2.16: Optimization and characterization of Ag/AgCl reference electrode. (**a-c**) Optimization of the parameters of Ag deposition. Scanning electron microscopy (SEM) images scale bar, 5 µm. (**d-f**) Optimization of the parameters of $FeCl_3$ etching to form AgCl. SEM images scale bar, 5 µm. (**g-i**) Characterization of Ag/AgCl electrode using HRTEM, HAADF-STEM, and EDS mapping. (**g**) HRTEM image of AgCl on Ag. Scale bar, 5 nm. (**h**) HAADF-STEM of AgCl on Ag. Scale bar, 2.5 µm. (**i**) EDS mapping of corresponding Ag and Cl. Scale bar, 2.5 µm.

To fabricate a suitable Ag/AgCl electrode, several parameters were optimized. First, both Cr and Ti were investigated as the adhesion layer for Ag deposition, as Ag alone would produce a discontinuous pattern under evaporation (**Fig. 2.16a**). Compared with Cr, Ti helped produce a more uniform and continuous Ag film (**Fig. 2.16b and c**). Second, the concentration of $FeCl_3$ solution during etching process was studied. While using 1 mM $FeCl_3$ solution generated a small portion of AgCl particles on Ag film (**Fig. 2.16d**) and using 5 mM $FeCl_3$ solution produced discontinuous Ag/AgCl islands (**Fig. 2.16f**), 3 mM $FeCl_3$ solution etching formed a well-distributed highly concentrated AgCl particles on Ag film (**Fig. 2.16e**), and therefore the parameters were chosen as the standard recipe for Ag/AgCl electrode fabrication. HRTEM image of Ag/AgCl electrodes shows polycrystalline AgCl particles formed on polycrystalline Ag film (**Fig. 2.16g**) and high-

angle annular dark-field scanning TEM (HAADF-STEM) image with EDS mapping result demonstrates the existence of both Ag and Cl elements at a larger scale (**Fig. 2.16h and i**), which proves the successful fabrication of Ag/AgCl nano-electrode.

The design of three-electrode configuration is shown in **Fig. 2.17a**. The interdigital electrodes enable electrochemical reactions inside the liquid pockets. The WE has many rectangular grids in the middle, which helps distinguish the electrodes during *in siu/operando* TEM imaging. In addition, the optical microscopy image shows the uniform covering of polymer membrane and well deposition of electrodes.

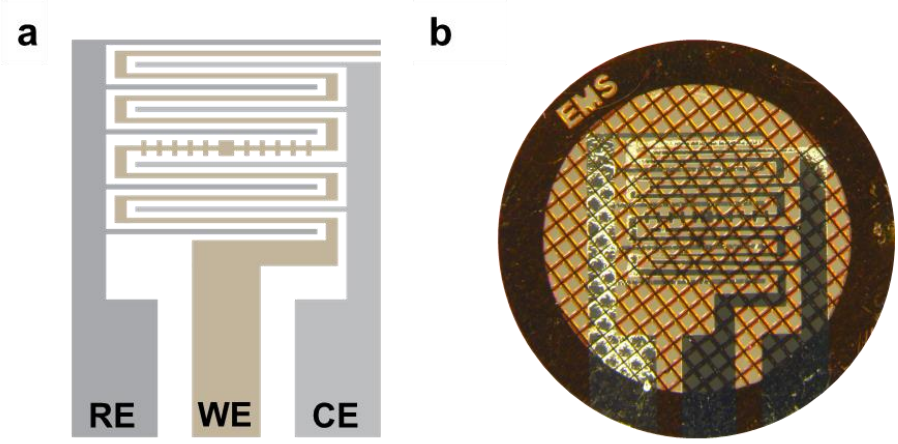

Figure 2.17: Characterization of three-electrode polymer membrane-based electrochemical liquid cells. (**a**) Electrode configuration design for a three-electrode polymer membrane-based liquid cell. (**b**) Optical microscopy image of a three-electrode electrochemical liquid cell bottom chip.

2.6 Conclusions

In conclusion, as the key component of *in situ/operando* liquid cell TEM techniques, liquid cells have made significant advancements over their 80-year history. By modifying membrane materials and developing new liquid cell structures, researchers can now explore more complex dynamic problems in physics, chemistry, and biology with high spatiotemporal resolution.

Here, we developed two-electrode and three-electrode polymer membrane-based electrochemical liquid cells, which enable the study of dynamic phenomena in electrocatalysts during electrocatalytic reactions at the atomic level. The new design provides a large viewing window for the EC-TEM observations and the possibility for elemental composition analysis, including EDS and EELS. We also integrated flexible electrode configurations and materials into the nano/microdevices for better versatility. The three-electrode system provides an advanced platform to investigate a specific reaction with more confidence and accuracy. We hope it can provide valuable insights for future development of *in situ/operando* TEM.

Chapter 3

Operando probing of nanocracking in CuO-derived Cu during CO_2 electroreduction

Identifying and controlling active sites in electrocatalysis remains a grand challenge due to restructuring of catalysts in the complex chemical environments during operation[168–170]. Inactive precatalysts can transform into active catalysts under reaction conditions, such as oxide-derived Cu (OD-Cu) for CO_2 electroreduction displaying improved production of multicarbon (C_{2+}) chemicals[171–173]. Revealing the mechanism of active site origin in OD-Cu catalysts requires in situ/operando characterizations of structure, morphology, and valence state evolution with high spatial and temporal resolution[174,175]. Applying newly developed EC-TEM combined with XAS, our multimodal operando techniques unveil the formation pathways of OD-Cu active sites from CuO bicrystal nanowire precatalysts. Rapid reduction of CuO directly to Cu within 60 seconds generates a nanocrack network throughout the nanowire, via formation of "boundary nanocracks" along the twin boundary and "transverse nanocracks" propagating from the surface to the center of the nanowire. The nanocrack network further reconstructs, leading to a highly porous structure rich in Cu nanograins, with a boosted specific surface area and density of active sites for C_{2+} products. These findings suggest a means to optimize active OD-Cu nanostructures through nanocracking by tailoring grain boundaries in CuO precatalysts. More generally, our advanced operando approach opens new opportunities for mechanistic insights to enable improved control of catalyst structure and performance.

This chapter is adopted from Jiawei Wan *et al* 's work entitled "*Operando* probing of nanocracking in CuO-derived Cu during CO_2 electroreduction" from reference 38, with permission to reproduce it in this dissertation from the co-authors. In this work, the XAS characterization was performed by Dr. Ershuai Liu and Dr. Walter S. Drisdell. The performance testing was performed by Dr. Woong Choi, Dr. Keon-Han Kim and Prof. Alexis T. Bell. DFT calculation was performed by Dr. Buyu Zhang and Prof. Mark Asta. Electron tomography was performed by Dr. Meng Zhang and Dr. Han Xue.

3.1 Introduction

Cu is the only metallic catalyst for the CO_2RR that produces significant C_{2+} chemicals[176–178]. Among various Cu-based materials, the OD-Cu exhibits enhanced electrocatalytic activity and it is easy to prepare at low cost for potential practical applications[171–173]. Although diverse types of grain boundaries[179,180] and residual Cu^+ species[172,181] from precatalyst reconstruction have been reported as the active sites, the formation mechanisms and design principles for OD-Cu catalysts remain lacking. A major hurdle is the inability to directly monitor the structural evolution of OD-Cu catalysts under operating conditions[174] due to the fast, complex dynamic transformation behavior of precatalyst activation during CO_2RR[173,182]. Although advancements have been made recently in *in situ/operando* microscopy and spectroscopy studies of Cu-based catalysts during electrocatalytic reactions[71,72,96,125,183–185], tracking both morphological and compositional evolutions with high spatiotemporal resolution is needed to resolve the origin and evolution of OD-Cu active sites.

Here we report *operando* studies of OD-Cu catalysts evolution from CuO bicrystal nanowires during CO_2RR using a multimodal platform coupling the newly developed high-resolution EC-TEM with time-resolved and high energy resolution fluorescence detected (HERFD-) XAS. We discover the formation pathways of catalytically active sites through nanocracking of CuO bicrystal nanowire precatalysts during rapid reduction to metallic Cu (**Fig. 3.1a**). Electrocatalytic performance testing in reactors of different scales (EC-TEM liquid cell, H-type cell, and membrane electrode assembly (MEA)), coupled with complementary ex situ structural characterizations, suggest the nanocracking behavior is general across all relevant operating conditions and is critical for enhanced C_{2+} activity.

3.2 Experimental setup and characterization

3.2.1 Preparation of CuO nanowire precatalysts

CuO nanowires were synthesized through a typical thermal oxidation method[186] with an optimized procedure. First, Cu substrates (0.1 mm Cu foils, ≥99.9%, Thermo Scientific Chemicals) were cleaned with an aqueous 1.0 M HCl solution (Sigma-Aldrich) for 60 minutes, followed by rinsing with deionized water and dried with N_2 gas. Then, the Cu substrates were immediately put into a box furnace (Thermo Scientific Lindberg/Blue M) maintained at 450 ℃ for 90 minutes at ambient pressure, giving rise to the CuO nanowire growth on the substrate. Next, CuO nanowires were separated from the substrates by sonication in ethanol for 120 minutes and supernatants were collected after centrifuging (Eppendorf) at 3000 rpm for 10 minutes. Finally, purified CuO nanowires were collected by centrifuging at 9500 rpm for 10 minutes and dried in vacuum for further use.

3.2.2 Fabrication of electrochemical liquid cells

The electrochemical liquid cells for quasi-*operando* EC-TEM were built with a bottom and a top chip capsuling multiple liquid pocket in between. The bottom and top chips were fabricated based on the commercial Cu or Au TEM grids (200 square mesh, Electron Microscopy Sciences). The grids are first coated with 250 nm of electrically insulating aluminum oxide (Al_2O_3) by sputter deposition (AST-sputter, Berkeley Marvell NanoLab). Subsequently, a 10 nm-thick insulating

polymer (0.25% Formvar solution in 1,2-dichloroethane (≥99.0%, Sigma-Aldrich)) film was transferred onto the grids. Then, 10 nm-thick Pt interdigital electrodes were deposited onto the bottom chips using the e-beam evaporation (Semicore-evaporator, Molecular Foundry, LBNL) through a specially designed shadow mask, enabling electrochemical reaction in the micro-electrochemical system.

3.2.3 Quasi-*operando* EC-TEM measurements

Quasi-*operando* EC-TEM measurements were performed in CO_2-saturated 0.1 M $KHCO_3$ electrolyte (99.95%, Sigma Aldrich) within the self-fabricated electrochemical liquid cells using a FEI ThemIS aberration-corrected TEM at 300 keV (NCEM, LBNL). To assemble a liquid cell, CuO bicrystal nanowire precatalysts were drop-cast onto the electrodes (bottom chip), followed by adding 1 μL electrolyte and covered with the top chip. An electrical biasing holder (Hummingbird Scientific) coupled with a home-made contact board and a potentiostat (Biologic SP-200) were used for connecting liquid cells and providing electrochemical measurements in EC-TEM. Quasi-*operando* EC-TEM videos were acquired at a speed of 500 ms per frame (2,048 × 2,048 pixels) at a beam dose rate of about 400 $e^- Å^{-2} s^{-1}$, which ensured the absence of beam-induced damage on the precatalyst materials. A beam dose control experiment was performed before the EC-TEM video experiments. Amount of electrolyte and CO_2 reactant was also discussed. Based on the multiple experimental results and analysis from different aspects, the EC-TEM measurements apply catalytically relevant potentials and environments. We are not able to directly detect the catalytic products during EC-TEM experiments, due to the limitation of equipment configuration, therefore, we consider the measurements as quasi-*operando*. HAADF-STEM images and EDS were performed for chemical identification.

3.2.4 Precatalyst electrodes preparation

The CuO nanowire precatalyst inks for both H-type cell and MEA testing were prepared by bath sonicating a mixture of 50 mg of as-synthesized CuO nanowire and 50 mg of Nafion solution (5 wt%, Ion power, D521) in 25 mL of isopropyl alcohol (HPLC-grade, Aldrich) for 1 h. For the H-type cell experiments, the CuO nanowire precatalyst electrodes were fabricated by hand spray coating of the as-prepared ink on the gas diffusion layer (Sigracet 39BB) using an airbrush gun (RichPen GP-1). The precatalyst loading amount was controlled by the sprayed ink amount from 0.05 mg cm^{-2} to 1.0 mg cm^{-2} and measured by X-ray fluorescence spectroscopy (XRF, Bruker). The active areas of the electrodes were confined to 1 cm^2 and the rest of the electrode area was masked on both sides using insulating tape. The same CuO nanowire precatalyst ink and gas diffusion layer were employed for MEA cell testing. However, the Sono-Tek spray coater was used at 120 kHz sonication with 0.2 mL min^{-1} of ink injection rate for coating CuO nanowire on the 5 cm^2 of gas diffusion layer (Sigracet 39BB).

3.2.5 *Operando* XAS measurements

The electrode inks for the XAS electrodes were composed of 18.2 MΩ purity deionized water (Millipore), isopropyl alcohol (HPLC-grade, Aldrich), 5 wt% EW1100 Nafion solution (Aldrich), and the synthesized CuO precatalyst powder. The ink was hand-sprayed onto a Sigracet

39BB carbon paper. The final precatalyst loading was measured by XRF. The *operando* XAS experiments were conducted at room temperature in a home-made spectro-electrochemical H-type cell made from PEEK, with 0.1 M $KHCO_3$ electrolyte (99.95%, Sigma Aldrich) purged with Ar or CO_2. Potentiostat control was maintained with BioLogic SP-300 potentiostat. Before each measurement, the cell was held for 2-3 minutes to reach a pseudo-steady current density. Data collection was then performed at the chosen potentials. Time-resolved experiments started at the same time the potentials were applied. All of the data were collected at Cu K-edge under fluorescence mode. The corresponding reference foils to aid in energy alignment and normalization were collected simultaneously for *ex situ* measurements. For *operando* experiments, reference foil data were collected before and after *operando* measurements. HERFD-XAS data were collected at Cu K-edge, with the spectrometer calibrated at the Cu-$K_{\alpha 1}$ emission line (8047.8 eV) using a Si (444) crystal. The data were processed and fit using the IFEFFIT-based Athena[187] and Artemis[188] programs. Scans were calibrated, aligned, normalized, and background corrected, using the IFEFFIT suite[189]. The $\chi(R)$ were modeled using single scattering paths calculated by FEFF6[190].

3.2.6 Electrochemical CO_2RR measurements in H-type cells

Electrochemical CO_2RR testing in H-type cells was performed by a custom-made three-electrode H-type cell system. A Pt plate and Ag/AgCl (3 M KCl) were used as the counter and the reference electrodes, respectively. Cathode and anode chambers were separated with anion-exchange membrane (Selemion AMV-N, Asahi Glass) and filled with 1.8 mL of CO_2-saturated 0.1 M $KHCO_3$ (99.95%, Sigma Aldrich) solution. During the CO_2RR testing, the cathode chamber was continuously sparged with CO_2 gas (99.999%, Airgas) with a 5 cc min^{-1} flow rate, controlled by a mass flow controller (Alicat). The out-line gas from the cathode chamber was directly connected to gas chromatography (SRI Instruments) for gas product analysis.

The CO_2RR was carried out by applying step-wised potential from -1.5 V to -2.5 V (vs. Ag/AgCl) with a 0.5 V interval for 30 minutes. After CO_2RR at each potential, 0.2 mL of catholyte and anolyte was collected and mixed with 0.1 mL of D_2O (99.9 atom% D, Sigma Aldrich), containing 10 mM of dimethyl sulfoxide (DMSO) as an internal standard for quantification of liquid products by proton nuclear magnetic resonance (^{1}H-NMR, Bruker Ascend 500 MHz instrument).

The cell resistance was measured by electrochemical impedance spectroscopy (EIS) at open circuit potential. The applied potentials were converted to the reversible hydrogen electrode (RHE) using the following equation.

$$E\ (\text{vs. RHE}) = E\ (\text{vs. Ag/AgCl}) + 0.224\ \text{V} + 0.0591 \times \text{pH} - iR$$

Where i and R represent current and cell resistance from EIS measurement.

Faradaic efficiency (FE) of each product was calculated using the following equation.

$$FE_{product} = \frac{n_{product} \times F \times N}{i_{tot}} \times 100$$

Where i_{tot} is current, $n_{product}$ is the moles of product generated per second quantified by gas chromatography or ^{1}H NMR, F is Faraday constant, and N is a number of electrons to generate products from CO_2.

3.2.7 Electrochemical CO_2RR measurements in MEA

The anode catalyst ink was prepared by bath sonicating a mixture of 150 mg of IrO_2 powder (Alfa Aesar) and 600 mg of PiperION A ionomer solution (5 wt%, Versogen) in 1 mL deionized water and 9 mL n-propanol for 1 h. The anode was fabricated by hand spray of as-prepared IrO_2 catalyst ink on a laser-cut 5 cm^2 platinized Ti porous transport layer (Mott Corp.) using an airbrush gun. IrO_2 loading amount was 1.3 mg cm^{-2}, which was measured by the electronic balance. The anion exchange membrane (PiperION A, 40 μm thickness, Versogen) was pre-activated in 1 M KOH solution at least 24 hours before use.

A single MEA electrolyzer system (Fuel Cell Technology, FCT) with a single serpentine channel graphite flow field on the cathode and a single serpentine channel Pt-coated Ti flow field on the anode was used for CO_2RR measurements. The cell was assembled by stacking the as-prepared anode, membrane, and cathode, and subsequently compressed to 40 in-lbs in 10 in-lbs increments to form an MEA configuration. 20% and 0% compression of the cathode gas diffusion layer (GDL) and anode porous transport layers (PTL) was achieved by controlling the ethylene tetrafluoroethylene (ETFE) gasket thickness.

During the CO_2RR testing, humidified CO_2 gas (99.999%, Airgas) at room temperature was continuously passed through the cathode flow field at 200 cc min^{-1}, and 0.1 M $KHCO_3$ electrolyte was circulated with a rate of 20 mL min^{-1} using a peristaltic pump. The gas outlet was connected to gas chromatography (SRI Company) through a water trap containing 20 mL of deionized water. Anolyte volume was confined to 20 mL. The CO_2RR was carried out by applying step-wise cell potentials from 3 V to 4 V in 0.5 V increments. Gas chromatography data were collected after 5 minutes and 20 minutes of applying each potential. After 30 minutes of each potential application, 0.2 mL of sample from the water trap and anolyte was collected and liquid products were quantified by ^{1}H nuclear magnetic resonance (NMR) similar to the H-type cell experiments. FE of each product was calculated using the equation noted above.

3.2.8 Electrochemical active surface area measurements

The electrochemical active surface area (ECSA) of CuO nanowires on the cathode was measured by the underpotential deposition (UPD) of Pb. Cyclic voltammetry (CV) of each cathode, after different reaction times for CO_2RR, was recorded from -0.15 V to 0 V (vs. RHE) with a scan rate of 10 mV s^{-1} in 0.1 M $HClO_4$ / 0.05 M KCl / 0.5 mM $PbCl_2$ aqueous solution as an electrolyte. The ECSA was obtained by integrating the Pb UPD peaks in the range of -0.15 V to 0 V in the CV and dividing by the Cu surface conversion factor of 310 μC cm^{-2}. The roughness factor was calculated by dividing the ECSA of the cathode at each condition by the ECSA of the pristine cathode.

3.2.9 Cryo-ET measurements

The cryogenic transmission electron tomography (cryo-ET) images of CuO nanowire-derived Cu samples were collected via a Krios microscope at the Cal-Cryo facility, Berkeley QB3 Institute. This setup achieved a magnification of approximately 50,000x, translating to 1.67 Å per micrograph pixel, in super-resolution and correlated double sampling mode. Tilt series were recorded from -51° to +51° at 3° increments, with an automated manual operation for data collection, maintaining a ~2.0 μm defocus, and accumulating a total dose ranging from ~120-180 e- $Å^{-2}$ across 8 frames per angle, each with a 0.25 s exposure. Following acquisition, the tilt series underwent preprocessing using MotionCor2 to correct beam-induced motion. The 3D reconstruction was achieved using a patch tracking function implemented in IMOD. The cross-section photograph was analyzed through Chimeral UCSF.

3.2.10 Oxygen vacancy calculations

Density functional theory (DFT) calculations were performed using Vienna ab initio simulation package (VASP) to calculate the diffusion barrier between different vacancy sites. All the calculations were performed spin-polarized, employing the Perdew-Burke-Ernzerhof (PBE) generalized gradient approximation (GGA) to describe the electron exchange and correlation interactions[191,192]. The DFT+U method was employed with U = 7 eV and J = 0 eV[193,194]. The optimized structural parameters using the bulk CuO model are a = 0.449 nm, b = 0.367 nm, c = 0.512 nm, β = 96.1°[195], respectively. Monkhorst-Pack k-point grids for the Brillouin-zone integration were applied with linear k-point density higher than 29 per $Å^{-1}$ along each periodic direction[196]. The cut-off energy for the plane wave basis was 400 eV. The bicrystal grain boundary structure is a low-index and symmetrical (002)/(002) tilt boundary. Along z axis, there are 8 Cu layers and 7 O layers, plus 12 Å vacuum. O vacancies are created by deleting the O atoms and the system is relaxed to get the energy. Diffusion barriers between different O vacancies are calculated using the Nudged Elastic Band (NEB)[197,198] method in VASP with 4 additional images apart from initial and final sites. Convergence of the spatial dependence of the oxygen vacancy formation energy is also verified using a larger supercell.

3.3 Characterization of CuO bicrystal nanowire precatalyst

CuO nanowires are prepared using a thermal oxidation method[186], with an optimized purification procedure. (**Fig. 3.2**). TEM measurements show the typical morphology of a CuO nanowire with the growth direction of $[1\bar{1}0]$ and bicrystal structure with the (002) twin plane in the middle (**Fig. 3.1b, 3.3** and **3.4**)[199,200]. HRTEM image confirms its monoclinic crystalline structure with the $(1\bar{1}\bar{1})$ and $(\bar{1}\bar{1}1)$ lattice (*d* spacing ~2.51 Å) mirror reflected along the (002) twin plane (*d* spacing ~2.52 Å) (**Fig. 3.1c**). X-ray absorption near-edge structure (XANES) of Cu K-edge of the as-prepared CuO nanowires and corresponding references demonstrate dominant CuO phase in the precatalysts (**Fig. 3.1d**). The Fourier transform of extended X-ray absorption fine structure (FT-EXAFS) reveals the characteristic peaks at 1.5 Å and 2.4 Å, which correspond to the Cu-O and Cu-Cu scattering paths in CuO, similar to the CuO standard spectra (**Fig. 3.1e**). Assisted by multifarious techniques (**Fig. 3.5** and **3.6**), we conclude that CuO bicrystal nanowires are obtained as precatalysts for CO_2RR.

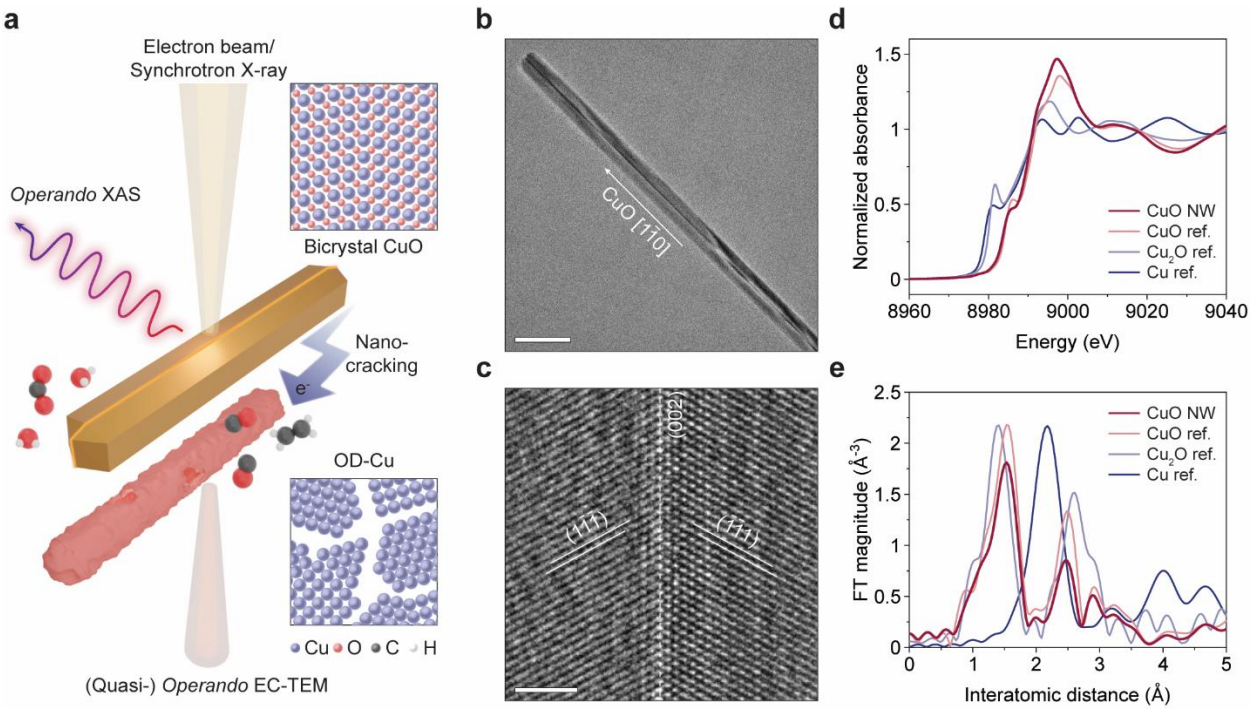

Figure 3.1: The *operando* electrocatalytic platform used to study structural dynamics of nanocatalysts for CO_2RR and characterizations of CuO bicrystal nanowire precatalysts. (**a**) Schematic illustration of the *operando* electrocatalytic platform employed in this study to track the dynamic behaviors of CuO precatalysts under CO_2RR conditions. Quasi-*operando* EC-TEM uncovers the morphological and local structural changes of individual working catalysts (TEM setup limits direct detection of catalytic products), while *operando* XAS unveils the valence state evolution of the ensemble catalysts. (**b**) TEM image shows the typical morphology of an as-prepared CuO bicrystal nanowire, which is divided by the twin boundary parallel to the nanowire's growth direction. Scale bar, 100 nm. (**c**) HRTEM image of the local area on a CuO bicrystal nanowire, showing the atomic twinned structure. Scale bar, 2 nm. (**d**) XANES and (**e**), FT-EXAFS spectra of Cu K-edge for the as-prepared CuO nanowire (NW) precatalysts and the corresponding references (CuO, Cu_2O, and Cu), revealing characteristic structure of CuO phase.

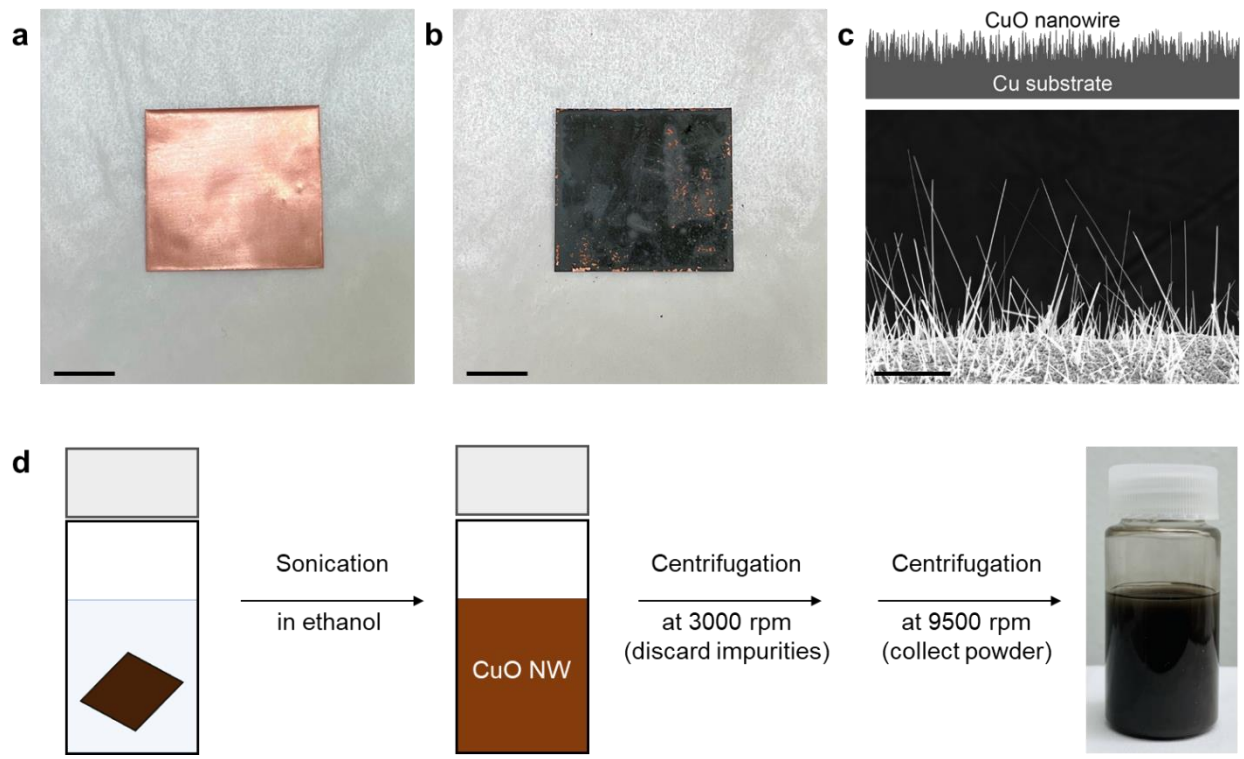

Figure 3.2: Synthesis of CuO bicrystal nanowire. Optical images of a Cu foil substrate (**a**) before and (**b**) after thermal. Scale bar, 1 cm. (**c**) SEM image of CuO nanowires prepared by heating the copper foils in (b). The nanowires grew vertically on the substrate. Scale bar, 1 μm. (**d**) Illustration of purification process of exfoliation CuO nanowires from Cu substrates. First, substrates after thermal oxidation were sonicated in ethanol and the CuO nanowires would disperse into the solution. Then, the solution was centrifuged at 3000 rpm for 10 minutes and the liquid supernatant was collected for further centrifugation at 9500 rpm for 10 minutes. Next, the CuO nanowires were collected in sediment and stored in ethanol for further use.

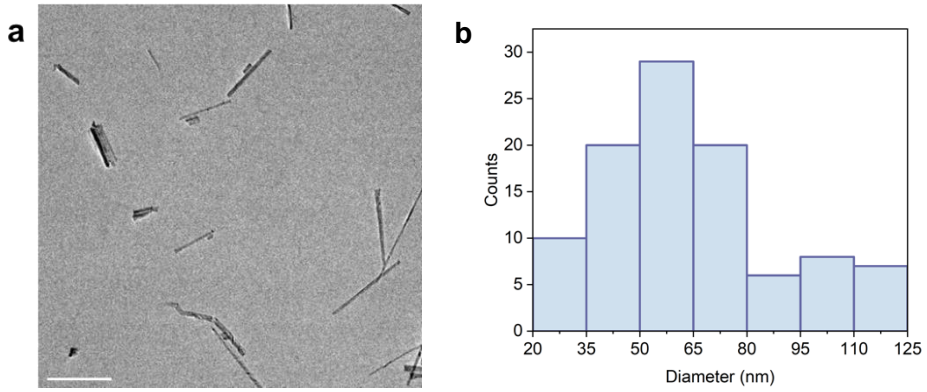

Figure. 3.3: TEM characterization of CuO bicrystal nanowire. (**a**) TEM image of CuO nanowire precatalysts after exfoliation and purification processes from Cu substrates in Fig. 3.2d. The morphology of CuO represented nanowire shape with different length. Scale bar, 1 μm. (**b**)

Diameter distribution histogram of 100 CuO nanowires, showing an average width of ~60 nm in diameter.

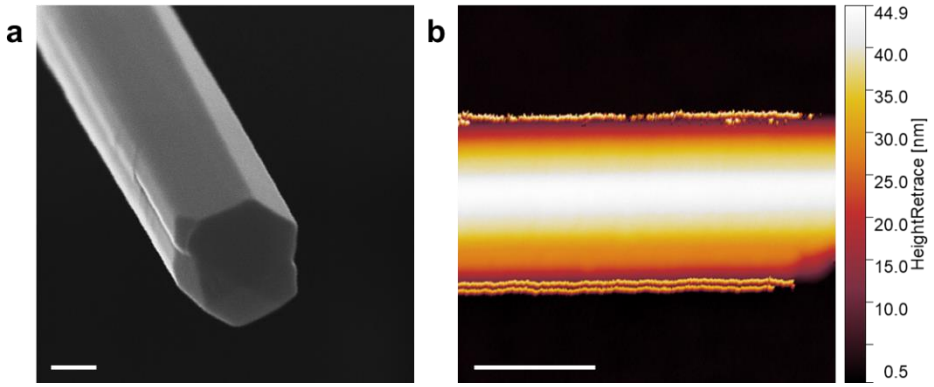

Figure 3.4: SEM and AFM characterization of CuO bicrystal nanowire. (**a**) SEM image showing the morphology of an individual CuO nanowire with raised ridge and polygonal cross section. Scale bar, 100 nm. (**b**) Atomic force microscopy (AFM) image showing the ridge in the middle. Scale bar, 100 nm. These results confirm the bicrystal structure with a boundary plane in the middle.

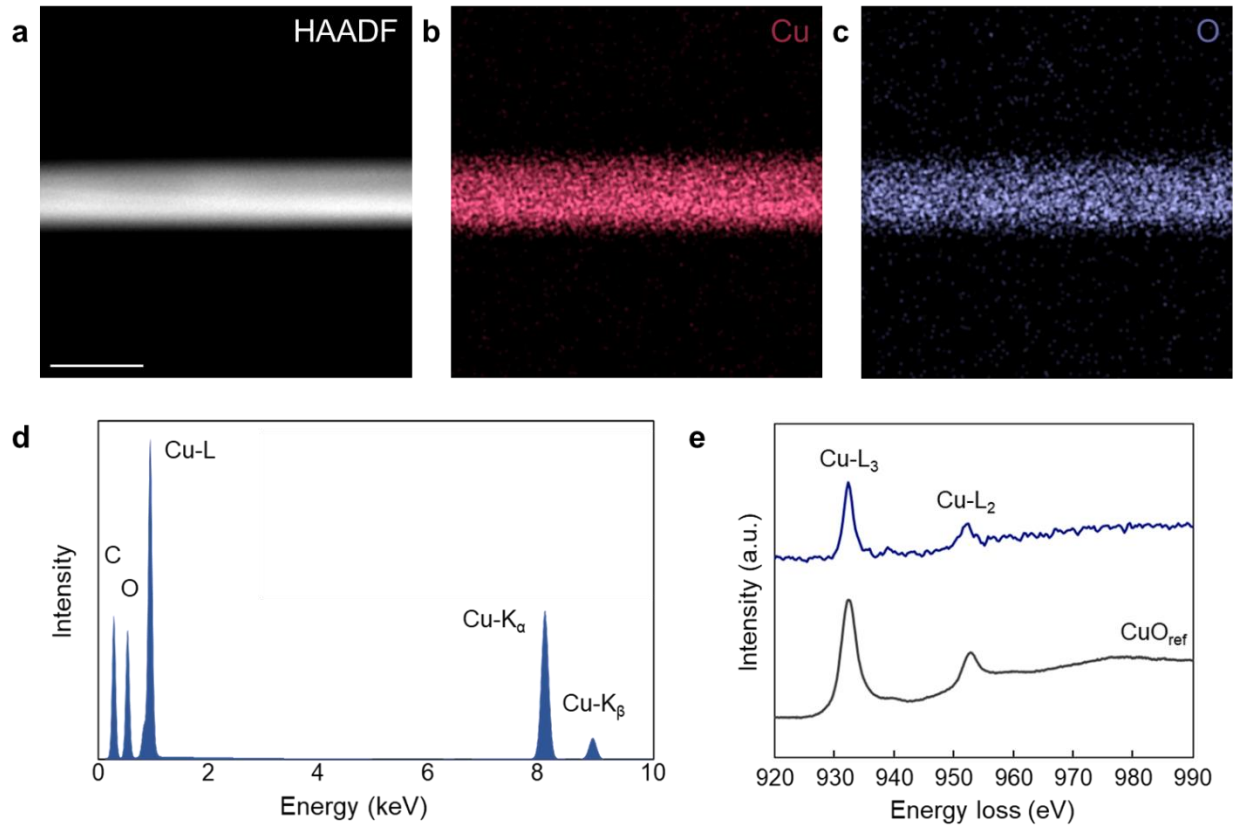

Figure 3.5: EDS and EELS characterization of CuO bicrystal nanowire. (**a**) HAADF-STEM image of an as-synthesized CuO nanowire. Corresponding EDS elemental maps of Cu (**b**) and O (**c**), showing the uniform distribution of Cu and O elements. Scale bar, 100 nm. (**d**) EDS spectra showing corresponding peaks of Cu and O. (**e**) EELS spectra measured on an individual CuO nanowire and corresponding CuO reference spectra. Cu-L_3 and L_2 edges are marked in the figure. The nanowire spectrum matches well with the CuO standard spectra, indicating successful synthesis of the CuO phase.

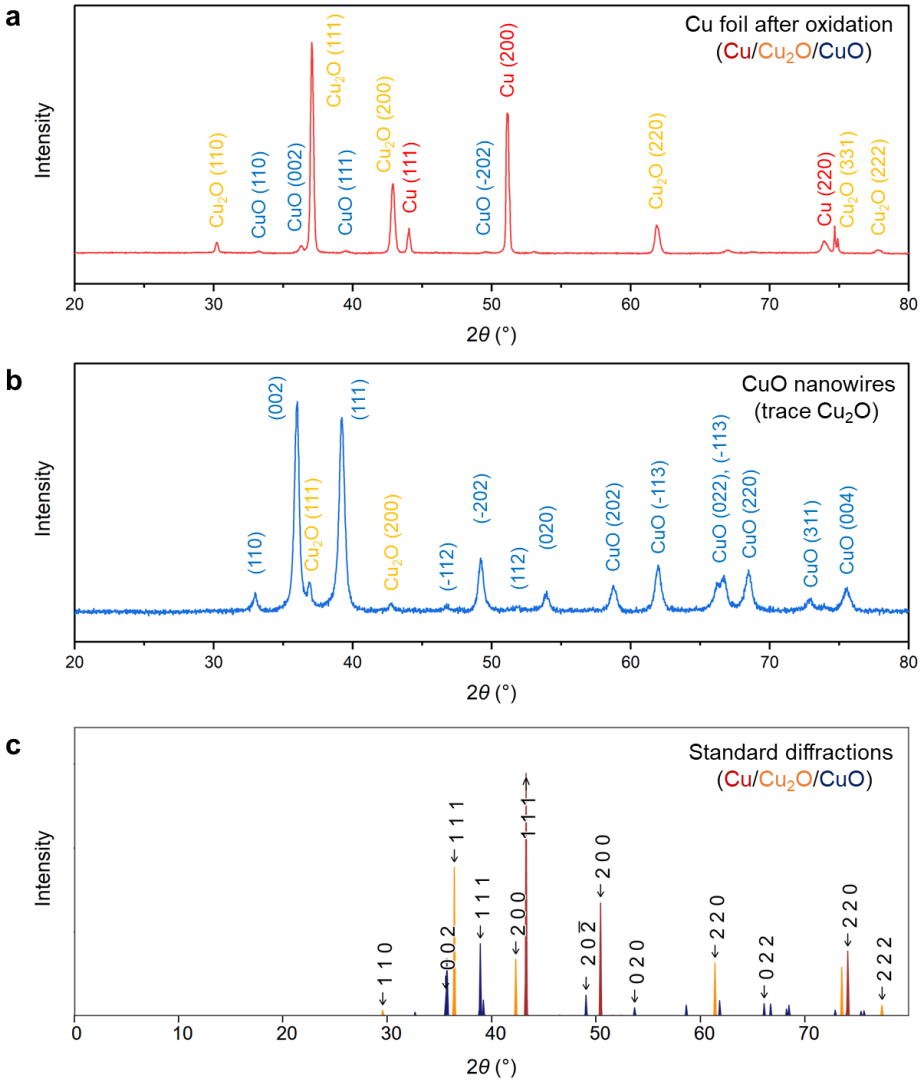

Figure 3.6: X-ray Diffraction (XRD) characterization of CuO bicrystal nanowire. (**a**) XRD result of the Cu substrate after thermal oxidation at 450 °C for 90 minutes, showing compositions of Cu, Cu_2O, and CuO. The majority Cu_2O and Cu phases show high intensity signal, while the CuO phase is trace amount. (**b**) XRD result of the CuO nanowire precatalysts after purification procedure in Fig. 3.2d. It shows the successful collection of CuO bicrystal nanowire precatalysts

with dominant phase of CuO and the coexistence of Cu_2O traces. (**c**) Standard XRD of Cu, Cu_2O, and CuO.

3.4 Visualizing nanocracking in catalyst restructuring by quasi-*operando* EC-TEM

We track the CuO nanowire precatalyst evolution under CO_2RR conditions by quasi-*operando* EC-TEM measurements using our newly developed high-resolution electrochemical liquid cell[70]. Both top and bottom chips of the liquid cell are insulated and covered with electron transparent polymer membranes, while the interdigital Pt electrodes are deposited onto the bottom chip as the WE and CE (**Fig. 3.7a**, and **Fig. 2.9-2.11**). The as-synthesized CuO nanowires are drop-cast onto the Pt electrodes, followed by loading liquid electrolyte (CO_2-saturated 0.1 M $KHCO_3$) and liquid cell assembly. It can form multiple thin (<100 nm) liquid pockets encapsulated by the thin polymer membranes (**Fig. 3.7a**, **Fig. 3.8, Fig. 2.12,** and **2.13**), which allows imaging of electrocatalyst evolution with unprecedented structural and compositional details with atomic/nanoscale resolution[70,100]. The cell potential is calibrated by the underpotential deposited hydrogen peak in 0.1 M perchloric acid in the electrochemical liquid cell[165], indicating -0.28 V vs. Pt is correlated to 0 V vs. SHE (**Fig. 2.13**). A cell potential of -2.0 V vs. Pt (-1.32 V vs. RHE) is applied on the CuO nanowires in quasi-operando conditions that we simulate the CO_2RR electrocatalytic reactions without directly measuring the reaction products.

The CuO bicrystal nanowire dramatically changes its structure and generates nanocracks while being reduced to Cu in 30 seconds under the operating conditions, which is observed from EC-TEM (**Fig. 3.9**). The formation and propagation of nanocracks within the CuO nanowire precatalysts under CO_2RR conditions follow two different pathways: "boundary nanocracking" along the twin plane, and "transverse nanocracking" perpendicular to the surface/twin plane, as illustrated in **Fig. 3.7b**. Sequential images from the EC-TEM video show structural dynamics of an individual CuO nanowire on the Pt WE at the edge-on position with high spatiotemporal resolution (**Fig. 3.9**, **Fig. 3.7c**). Nanocracks are highlighted using a ridge detection method[201] and overlaid on the false-colored images of the nanowire, which clearly show the evolution and distribution of both boundary and transverse nanocracks.

Distinct characteristics of the nanocracking dynamics during CuO precatalyst electroreduction are observed, as shown in **Fig. 3.7c**. First, both boundary and transverse nanocracks are initiated immediately after applying potential, manifesting as nanocavities (0 s). Then, the transverse nanocracks propagate from the surface to the interior of the nanowire (8.5 and 10.0 s), while the boundary nanocracks emerge and expand as nanocavities continuously coalescing on the twin plane (26.0 s), as depicted in **Fig. 3.7b**. Finally, the transverse nanocracks encounter the larger/wider boundary nanocracks at the middle of the nanowire (30.0 s) as CuO is fully reduced, introducing an OD-Cu structure with a nanocrack network. Continuously, evolution of the nanocracks involves rich dynamic fluctuations of expansion and contraction (e.g. The boundary nanocrack dramatically opens at 50.0 s and partially heals at 60.0 s in **Fig. 3.9**), which occur constantly via an intricate process of OD-Cu catalysts self-reconstructions[71,72,96,183].

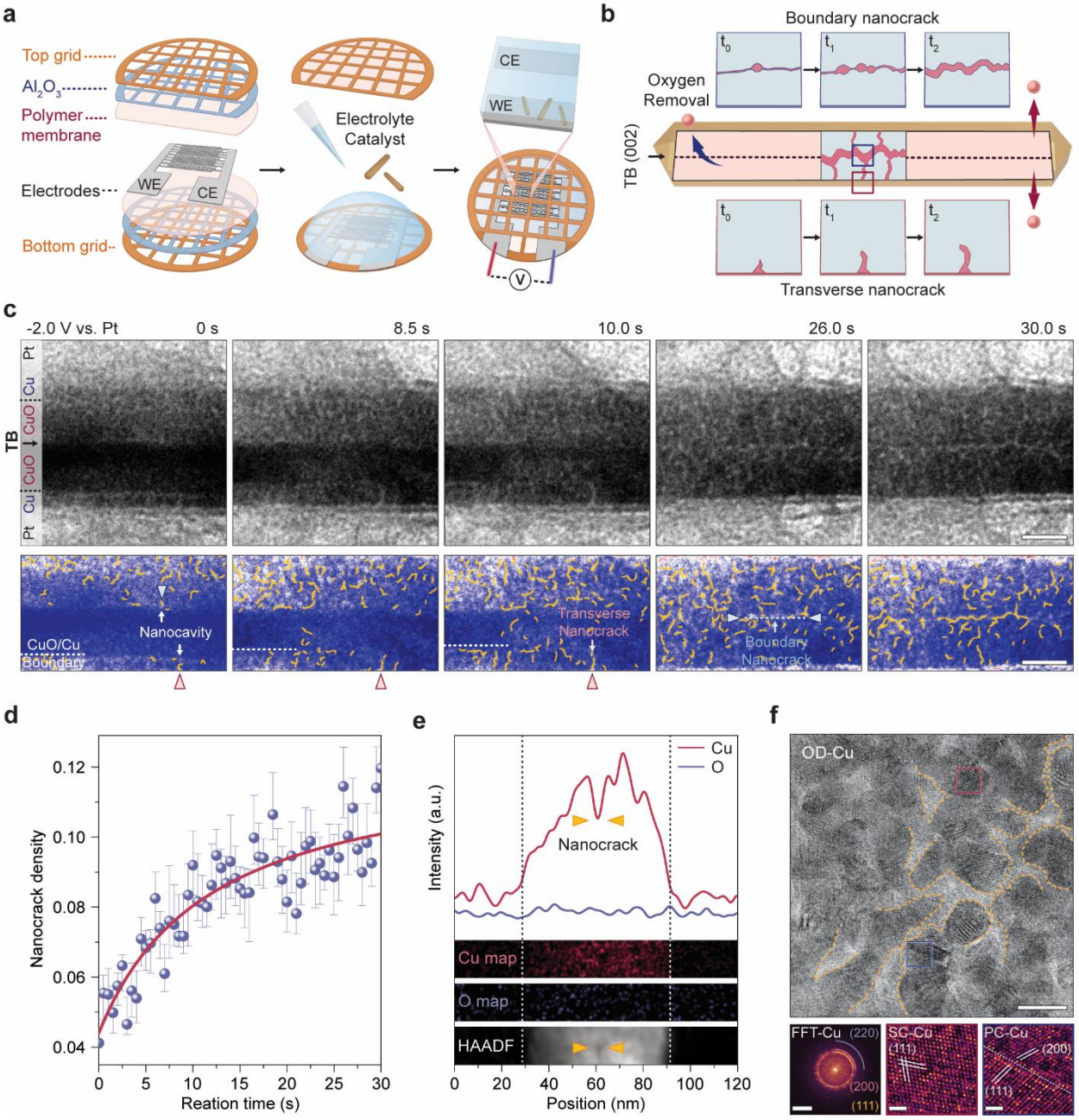

Figure. 3.7: Real-time probing of nanocracking in CuO bicrystal nanowire precatalysts under CO_2RR conditions using quasi-*operando* EC-TEM. (**a**) Schematic of fabrication and assembly processes of an EC-TEM liquid cell with the capability of enabling electrochemical measurements and simultaneously tracking the structural changes at nanoscale resolution. (**b**) Schematic illustration of nanocracking within a CuO nanowire during electroreduction, boundary (blue box) and transverse (red box) nanocracks grow and propagate on a projected plane consisted with EC-TEM. (**c**) Selected quasi-*operando* EC-TEM video frames of the morphological evolution of a CuO bicrystal nanowire at -2.0 V vs. Pt (-1.32 V vs. RHE) under CO_2RR conditions, and corresponding distribution of nanocracks (highlighted in yellow) on false-color images of CuO

nanowire (derived Cu). Transverse (red arrow) and boundary nanocracks (blue arrow), and CuO/Cu phase propagation (white dash line) are observed. Scale bar, 20 nm. (**d**) Nanocrack density evolution in the first 30 s under CO_2RR conditions. Systemic error may be introduced from detection under different contrast thresholds. (**e**) *In situ* elemental analysis of CuO nanowire-derived Cu in c after restructuring. HAADF image, Cu, and O maps, and corresponding intensity profiles of Cu K-edge and O K-edge show existence of metallic Cu and nanocracks. (**f**) *In situ* HRTEM image of cracked Cu after EC-TEM measurements. Scale bar, 10 nm. Nanocracks are highlighted in yellow dash line. FFT rings match with Cu (111), (200), and (220) facets, indicating dominated Cu phase. Scale bar, 5 nm^{-1}. Enlarged areas represent single crystalline (SC, red box) and polycrystalline (PC, blue box) Cu nanograins. Scale bar, 1 nm.

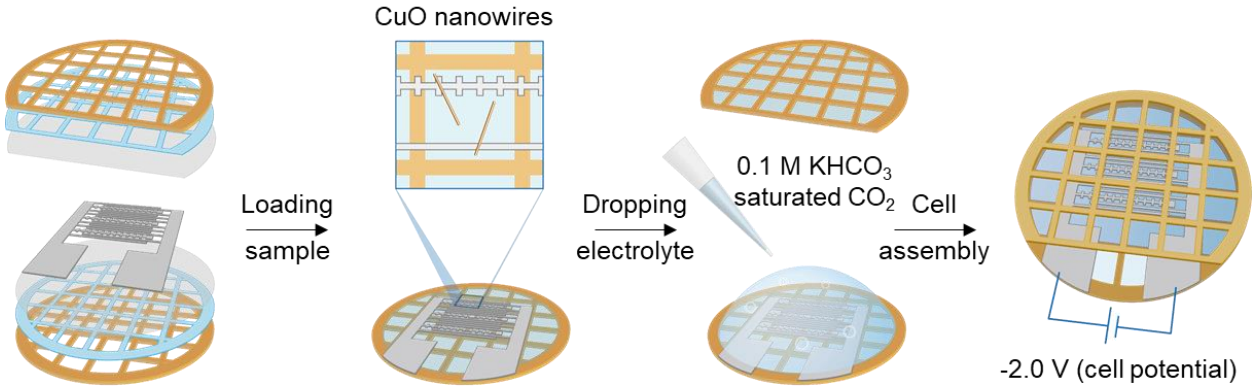

Figure. 3.8: Experimental setup of the quasi-*operando* EC-TEM measurements for electrocatalytic studies. The CuO nanowire precatalysts were first drop-cast onto the bottom chip of liquid cell. Then, 1 µL of electrolyte (CO_2-saturated 0.1 M $KHCO_3$) was added onto the bottom chip. Finally, the bottom chip was covered by the top chip, completing the liquid cell assembly. Multiple liquid pockets were able to form inside the liquid cell. The liquid cell was able to connect with the electrical biasing TEM holder and potentiostat for further electrochemical measurements.

As the electroreduction reaction proceeds, a rapid increase in nanocrack density (estimated by the measured total area of nanocracks divided by the area of the nanowire at a given reaction time) is observed, starting from 0.04 to 0.08 within 10 seconds, and reaching a relatively stable stage of 0.10 in 30 seconds (**Fig. 3.7d**). It is worth noting that the propagation of the CuO/Cu phase boundary (from surface to the center) (**Fig. 3.7c**) and the shrinking volume (~30%) from CuO to Cu shown in the EC-TEM results (**Fig. 3.10**) indicates the phase transition during the electroreduction of CuO. The formation of gas bubbles at catalyst surface is also observed via EC-TEM (**Fig. 3.9** and **Fig. 3.7c**), which can be attributed to the formation of gas phase species like carbon monoxide and hydrogen under the applied potential, indicating the on-going electrocatalytic reactions[176,177].

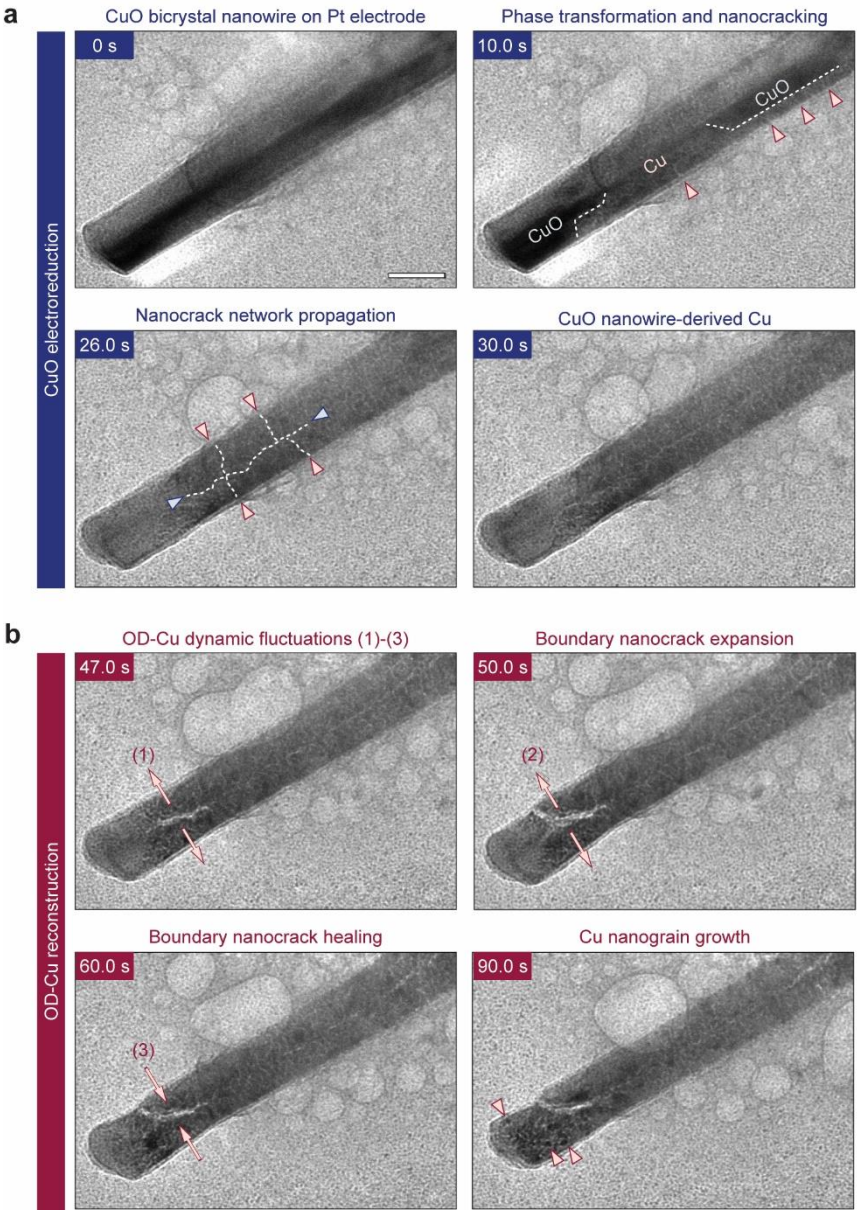

Figure. 3.9: Quasi-*operando* EC-TEM monitoring electroreduction of an individual CuO bicrystal nanowire and the reconstruction of OD-Cu. Selected quasi-operando EC-TEM video frames show (**a**) morphological evolution and phase transformation of a CuO bicrystal nanowire at -2.0 V vs. Pt (-1.32 V vs. RHE) under CO_2RR conditions. A nanocrack network is generated while CuO being reduced to OD-Cu within 30.0 s. (**b**) The OD-Cu continuously reconstructs and the nanocracks involve rich dynamic fluctuations. The boundary nanocracks dramatically expand and open at 50.0 s while they partially heal at 60.0 s (red arrows). The reconstructed Cu nanoparticles are also found (90.0 s). Scale bar, 50 nm.

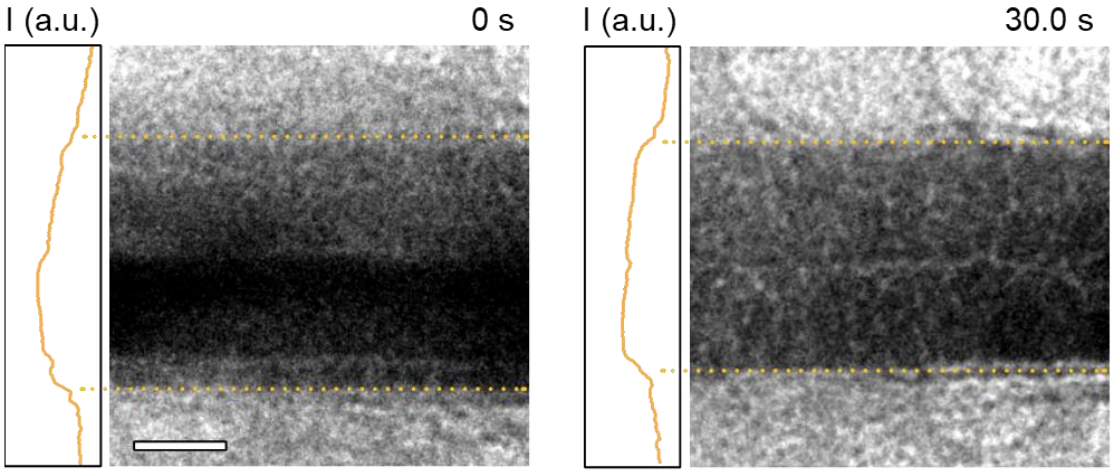

Figure. 3.10: Volume evolution of CuO nanowire-derived Cu catalysts. Selected quasi-*operando* EC-TEM video frames in Fig. 2c at 0 s and 30 s showing the shrunken volume of an individual CuO nanowire at -2.0 V vs. Pt (-1.32 vs. RHE) in CO_2-saturated 0.1 M $KHCO_3$. Scale bar, 20 nm. Cu has a smaller volume compared with CuO. Based on the density difference between CuO (6.31 g cm^{-3}) and Cu (8.96 g cm^{-3}), the volume would decrease ~40 % theoretically after electroreduction. Based on the contrast difference in intensity profiles, the dimeter of the nanowire decreased ~10 % from 0 s to 30 s. We estimate the decreased volume of OD-Cu by supposing CuO shrinks uniformly in three dimensions (~10 %), which would result in a volume decrease of ~30 %. The difference between estimation and theoretical value is originated from the porous nanocracks inside the OD-Cu structure.

In situ EDS and HRTEM measurements are performed on the CuO nanowire-derived Cu catalysts inside liquid cell after the EC-TEM imaging without introducing artifact from sample transfer, providing complementary information on the real active species. HAADF image and integral Cu and O elemental intensity profiles from corresponding EDS mapping reveal the boundary nanocrack within OD-Cu nanostructure, with no detectable signal of oxides (CuO and Cu_2O) (**Fig. 3.7e** and **Fig. 3.11**). The HRTEM image and corresponding FFT pattern also confirm the dominant metallic Cu phase that is fully reduced from CuO precatalyst (See standard diffractions in **Fig. 3.6**). The atomic structures show diverse Cu nanograins (single/poly-crystal) separated by the porous nanocrack network (**Fig. 3.7f**).

The restructuring mechanisms of CuO precatalyst during reduction (**Fig. 3.7b**) are further studied with DFT and NEB method, showing preferential O removal on the boundary plane, leading to boundary nanocracks formation (**Fig. 3.12**). Among the different diffusion pathways in CuO, it is energetically favorable for O to be removed perpendicular to the (002) twin boundary plane, which creates the transverse nanocracks. The reconstructed OD-Cu consists of edges, corners, and grain boundaries (**Fig. 3.7f**), all of which may improve the CO_2RR performance[179,180]. The connection between the wide center boundary nanocrack and the numerous smaller transverse nanocracks that compose the nanocrack network results in a highly porous structure with increased specific surface area and exposure of catalytic active sites, as well as providing efficient channels for reactant/product transport[202]. It may also improve activity through confinement effects[203,204].

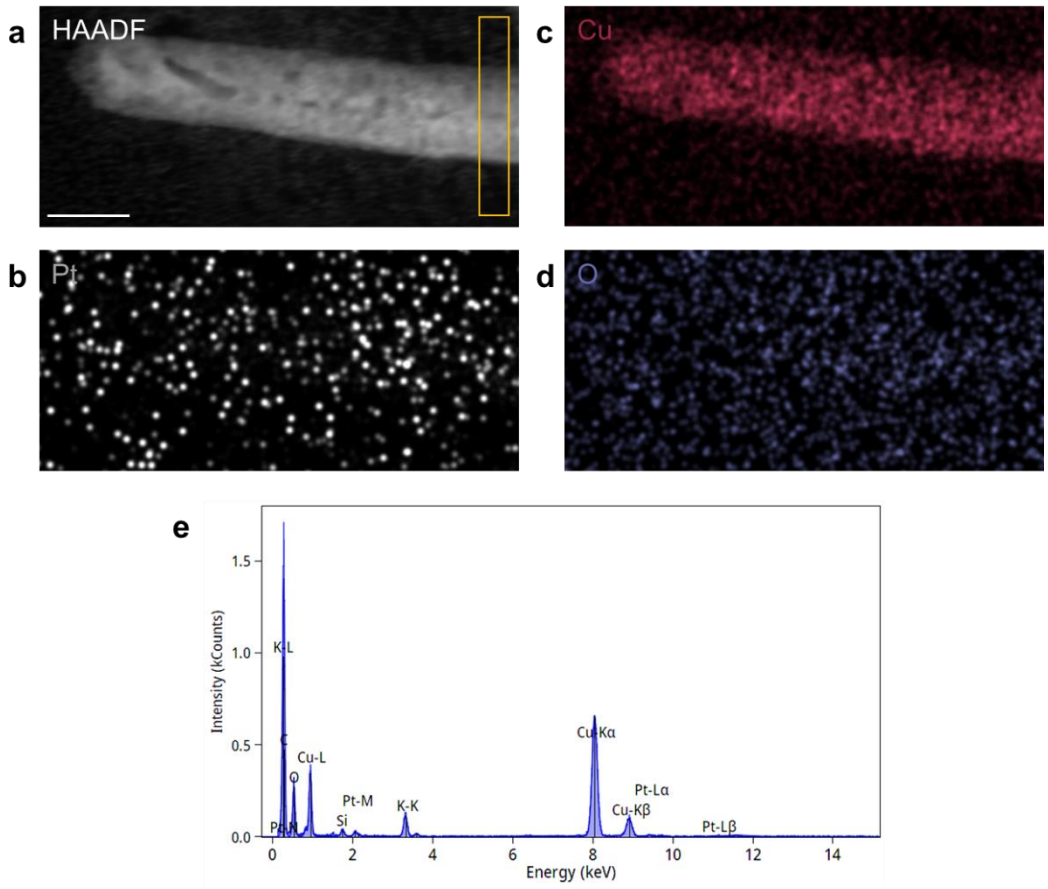

Figure. 3.11: *In situ* EDS measurements of CuO nanowire-derived Cu catalysts. (**a**) In situ HAADF-STEM image and EDS mapping of (**b**) Pt, (**c**) Cu, and (**d**) O of an individual CuO nanowire-derived Cu nanoparticle after quasi-operando EC-TEM experiments inside an electrochemical liquid cell. The Pt signal is due to the catalyst materials being seated on the Pt electrode and the oxygen signal is from background or electrolyte. The yellow box marked in (a) represents the area for line scan analysis of EDS intensity in Fig. 2e. Scale bar, 50 nm. (**e**) EDS spectra from the whole region of (a).

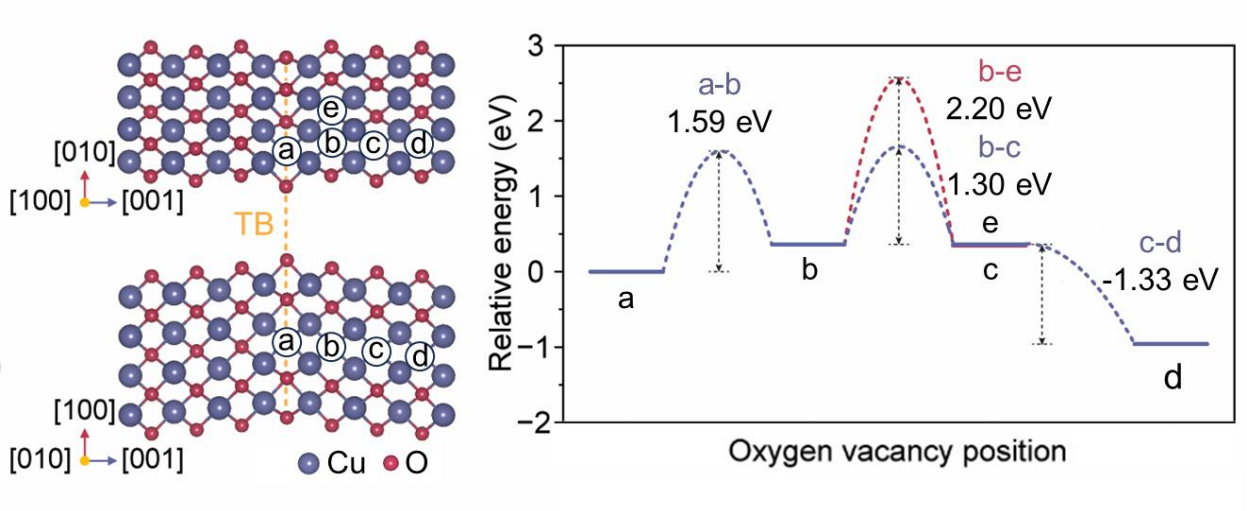

Figure. 3.12: Theoretical calculations of O vacancy diffusion in CuO reduction. DFT calculation results show energy of different O vacancy sites: (**a**) on the twin boundary (TB), (**b**) one atom away, (**c**) two atoms away perpendicular to twin boundary, and (**d**) on the surface. O vacancy prefer the sites at twin boundary and near surface, with relatively lower energy. This implies that O vacancies prefer to segregate at the boundary and will lead to the cracks along the twin boundary. NEB calculations further evaluate the energy barrier of different diffusion paths. We compare two paths: one is O vacancy diffuses perpendicular to the twin boundary (b)-(c) and the other one is O vacancy diffuses parallel to the twin boundary (b)-(e). The O vacancy diffusion barrier of (b)-(c) (1.3 eV) is smaller than that of (b)-(e) (2.2 eV), indicating O vacancy prefer to diffuse perpendicular to the twin boundary/surface, which can lead to formation of transverse cracks. Blue, red, and white balls represent Cu, O, and O vacancy, respectively.

3.5 Tracking ensemble valence state evolution by *operando* time-resolved XAS

Since the nanocracking process is induced by reduction of the CuO bicrystal nanowire precatalysts into metallic Cu, we employ *operando* time-resolved XAS to comprehensively study the reduction kinetics and valence state evolution across a range of electrochemical conditions including CO_2RR. These measurements are highly sensitive to the ensemble average oxidation state, and are conducted in an H-type cell similar to those typically used for catalytic testing[205] (**Fig. 3.13**). First, time-resolved XANES/EXAFS is applied for CuO nanowires at selected potentials based on the linear sweep voltammetry (LSV) (**Fig. 3.14**). All the potentials are converted to the RHE scale with *iR* correction unless noted otherwise. At -0.65 V (CO_2RR onset potential), initial reduction of CuO to Cu is observed within 30 s and is more dramatic after 60 s, indicated by the evolution of characteristic XANES features (pre-edge and white line intensity) (**Fig. 3.15a** and **b**) as well as diminishment of the Cu-O scattering path at 1.5 Å and emergence of Cu-Cu path of metallic Cu phase at 2.2 Å in FT-EXAFS (**Fig. 3.15c**). Around 120 s, the ensemble valence state stabilizes, closely matching the spectra at 1 h. It is noteworthy that the FT-EXAFS peak at 4.0 Å, representing the second shell of Cu-Cu scattering in metallic Cu, also increases in intensity with time, indicating that metallic Cu is becoming the dominant species after 120 s. At -1.0 V (C_{2+} production potential), the complete reduction of CuO occurs within 60 s (**Fig. 3.15d**

and **e**). The FT-EXAFS spectrum at 90 s under -1.0 V shows a negligible signal of Cu-O scattering peak at 1.5 Å, unlike the prominent shoulder peak observed at 90 s under -0.65 V, indicating a more thorough metallic phase formation (**Fig. 3.15f**). At all catalytically relevant potentials, the reduction of CuO occurs within 120 s, and the dominant species afterwards is metallic Cu (**Fig. 3.16**). We also find more negatively below the thermodynamic CuO electroreduction potential can lead to a faster reduction (**Fig. 3.15g**). This fast reduction kinetics is consistent with quasi-operando EC-TEM measurements under -1.32 V on an individual nanowire, showing nanocracking and OD-Cu phase propagation, implying the CuO is fully reduced to Cu within 30 s (**Fig. 3.7c**). This suggests that the nanocracking behavior observed with EC-TEM also occurs at all catalytically relevant potentials in an H-type cell.

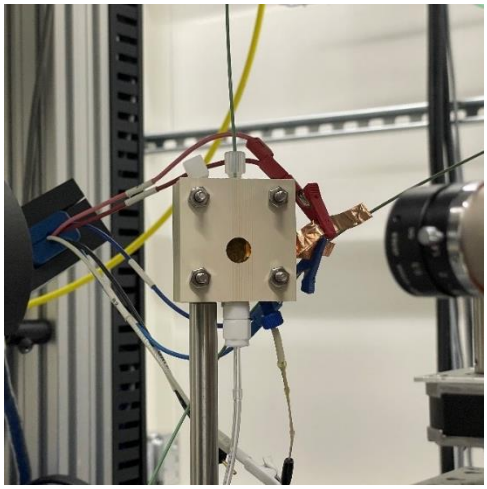

Figure 3.13: Configuration of the home-made H-type cell used for *operando* time-resolved and HERFD-XAS experiments. This cell is similar to those typically used for the CO_2RR testing. It was modified by introducing a transparent window for the synchrotron X-ray detection.

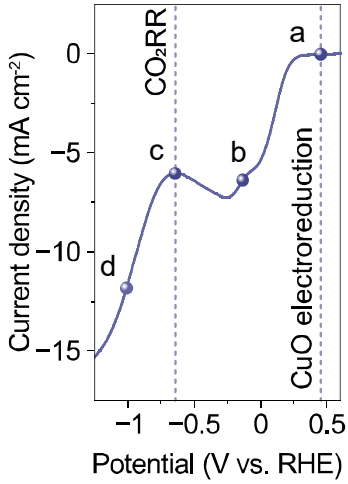

Figure 3.14: LSV profile of CuO nanowires in the electrolyte of 0.1 M $KHCO_3$ sparged with CO_2 inside the *operando* XAS cell. The points mark out regions under different potentials: (**a**) thermodynamic CuO electroreduction potential (0.45 V vs. RHE), (**b**) an intermediate CuO electroreduction potential (-0.1 V vs. RHE), (**c**) CO_2RR onset potential (-0.65 V vs. RHE), and (**d**) optimized potential for CO_2RR towards C_{2+} products (-1.0 V vs. RHE).

Next, we investigate whether the CuO nanowire ensemble reduces directly to metallic Cu, or whether the reduction pathway includes intermediate oxides (e.g. Cu_2O). For this we employ operando HERFD-XAS, which has increased energy resolution that increases sensitivity to small changes in XANES pre-edge features[206] (**Fig. 3.17** and **3.18**). Sequential potentials between 0.45 V and -1.0 V are applied, with HERFD-XAS collected after current density stabilized at each potential (2-3 minutes) (**Fig. 3.15h**). Above 0.25 V, the CuO nanowire ensemble shows stable XANES features that match the CuO standard spectra (**Fig. 3.18**), indicating that reduction is not yet triggered. At 0.15 V, the decrease in the major white line peak (8997 eV) and growth of the pre-edge peak (8980 eV) indicates the phase transformation to metallic Cu (**Fig. 3.19** and **3.20**). The observed transition to metallic Cu is consistent with the formation of Cu nanograins observed with EC-TEM (**Fig. 3.7f**). Significant evolution of the edge feature at 0.05 V (**Fig. 3.15h** inset) indicates significant metallic Cu contributions. The 1st derivative XANES also shows an unambiguous major peak shift from 8984 eV (0.15 V) to 8979 eV (0.05 V) (**Fig. 3.15i**)[125], indicating the direct reduction of CuO into metallic Cu, which occur before the onset potential of CO_2RR catalysis. As the applied potential enters the CO_2RR regime (down to -1.0 V), more complete reduction is shown on the timescale of the HERFD-XAS measurement (**Fig. 3.15h** and **i**). It is noteworthy that small Cu^+ signal is also found (8980.5 eV) in the 1st derivative XANES at open-circuit voltage (OCV) (**Fig. 3.15i**), which could be ascribed to the residual Cu_2O in the as-prepared CuO precatalysts[186] (**Fig. 3.6**). However, this signal does not increase, suggesting that Cu_2O is not formed as an intermediate from CuO, and disappears below 0.05 V through full reduction towards metallic Cu.

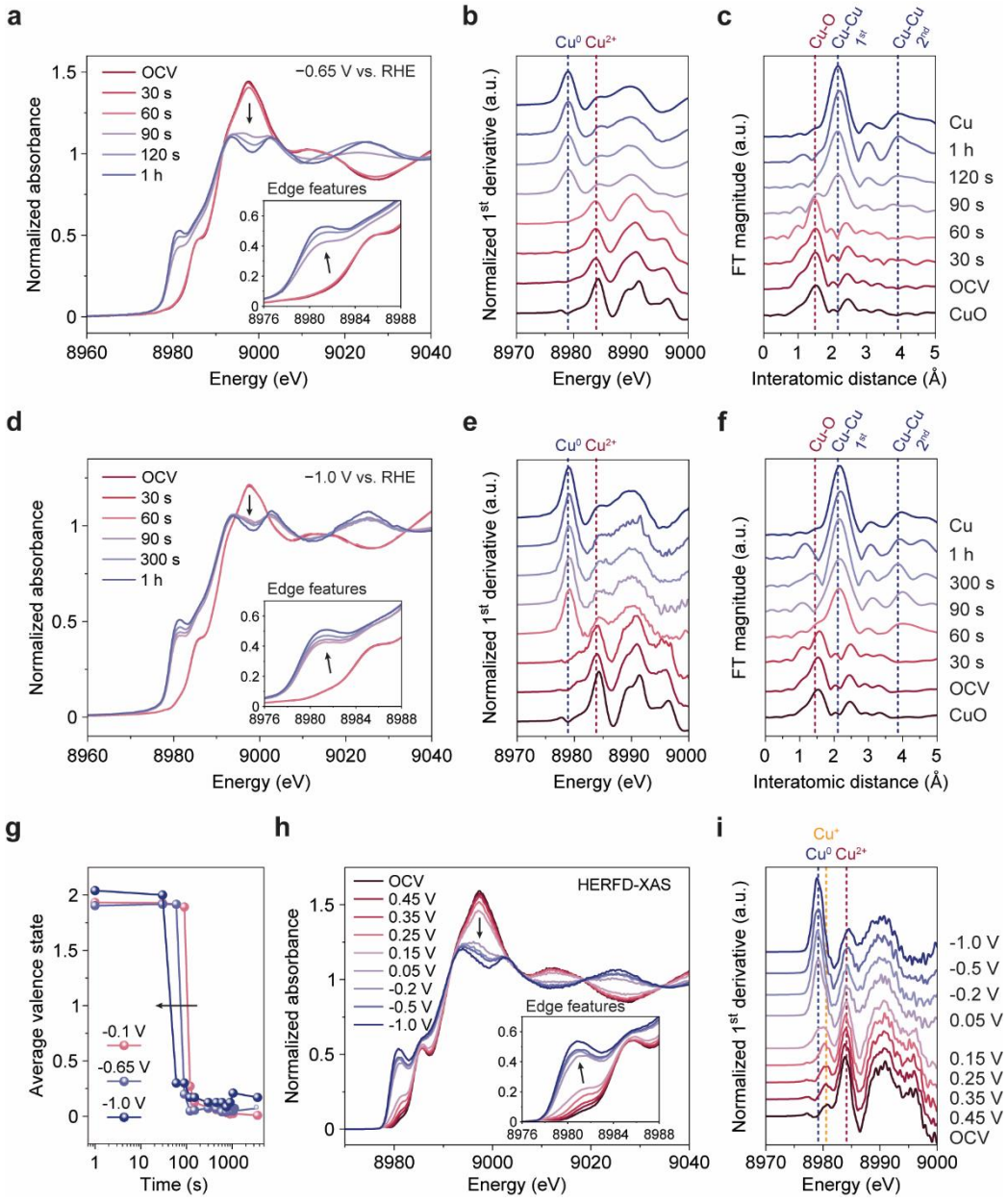

Fig. 3.15: *Operando* time-resolved (HERFD-) XAS studies of ensemble CuO bicrystal nanowire precatalysts under CO_2RR conditions. (**a**) Operando time-resolved conventional XANES spectra, (**b**) corresponding 1st derivative spectra, and (**c**) FT-EXAFS spectra of CuO nanowire precatalysts at -0.65 V vs. RHE under CO_2RR conditions. (**d**) Operando time-resolved conventional XANES spectra, (**e**) corresponding 1st derivative spectra, and (**f**) FT-EXAFS spectra of CuO nanowire precatalysts at -1.0 V vs. RHE under CO_2RR conditions. (**g**) Ensemble valence state evolution at different potentials. (**h**) Potential dependence of operando Cu K-edge HERFD-XANES spectra of the CuO nanowire precatalysts under CO_2RR in 0.1 M CO_2-saturated $KHCO_3$ using chronoamperometry (CA) for 2-3 minutes and (**i**) the corresponding 1st derivative spectra.

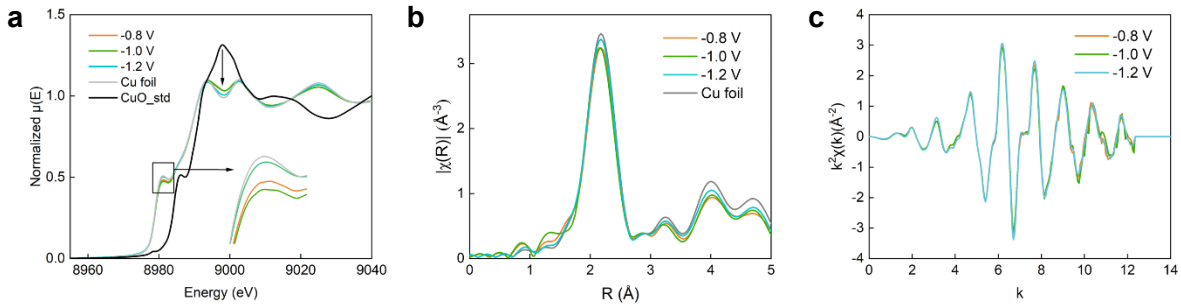

Figure 3.16: *Operando* XAS measurements of CuO nanowire at different potential. *Operando* (**a**) XANES spectra and FT-EXAFS spectra in (**b**) R space and (**c**) K space of the CuO nanowire-derived Cu catalysts under -0.8 V, -1.0 V and -1.2 V vs. RHE. All spectra were collected in the CO_2-saturated 0.1 M $KHCO_3$ electrolyte.

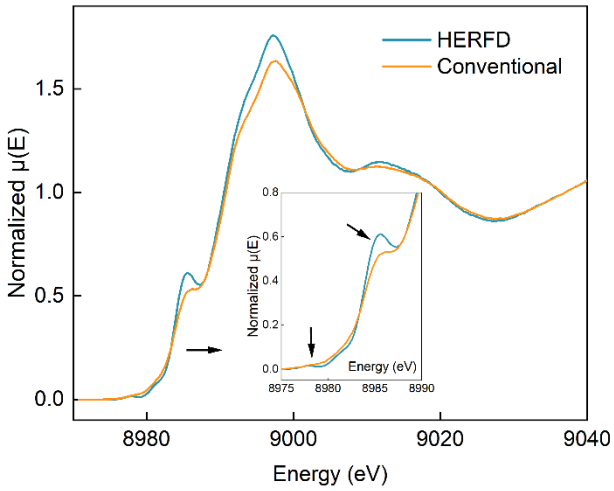

Figure 3.17: Comparison of HERFD-XAS and conventional XAS of the CuO nanowire precatalysts in the XANES region. The HERFD-XAS provides a higher resolution at the pre-edge peaks (8979 eV and 8985 eV, inset) and the major peak (8995 eV). Data was collected at Cu K-edge in the N_2-purged 0.1 M $KHCO_3$ electrolyte under open-circuit potential.

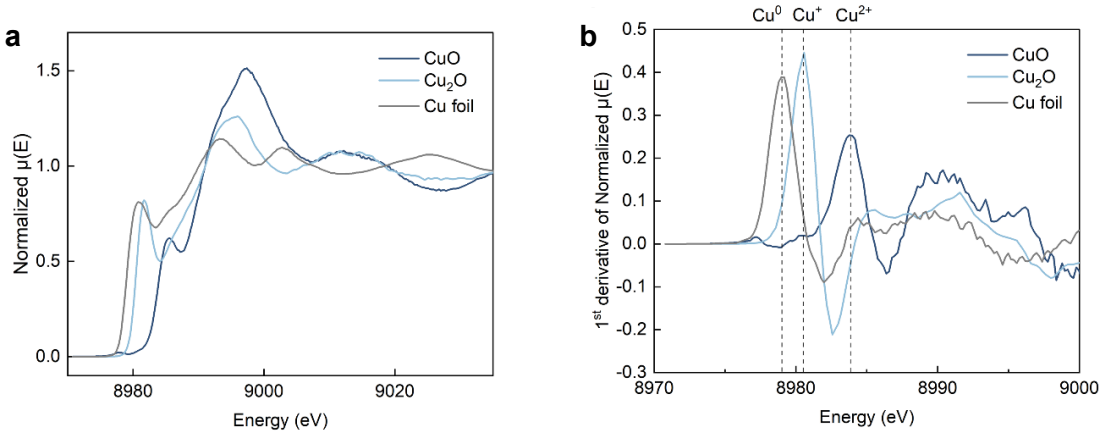

Figure 3.18: Comparison of standard samples of CuO, Cu_2O and Cu foil in the HERFD-XAS mode. (**a**) HERFD-XANES spectra of aforementioned Cu standards (Due to the high density of the Cu foil, self-adsorption was inevitable.) (**b**) The first derivative of normalized HERFD-XANES spectra of (a). The feature peaks of Cu^0, Cu^+ and Cu^{2+} locate at 8979 eV, 8980.5 eV and 8984 eV, respectively.

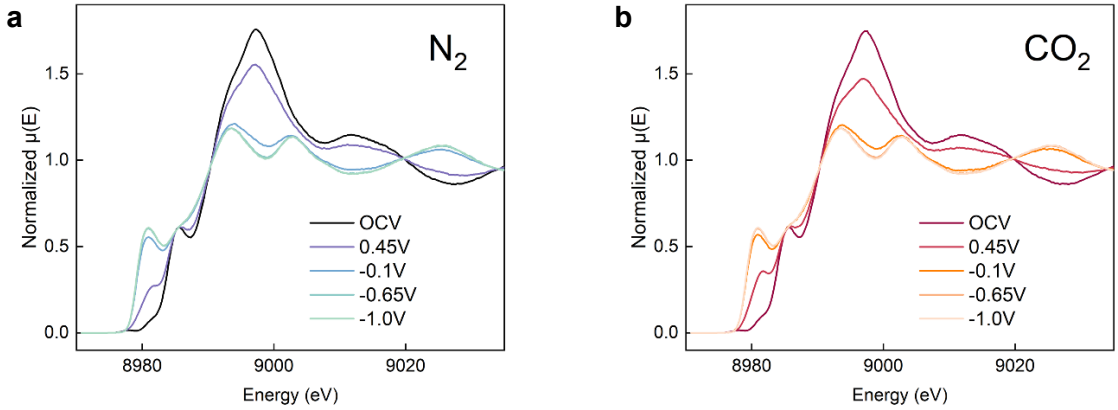

Figure 3.19: CuO nanowire precatalysts and the derived Cu catalysts under different potentials collected in the HERFD-XAS mode, in (**a**) N_2 and (**b**) CO_2-purged 0.1 M $KHCO_3$ electrolyte. In general, the spectra collected in N_2 are similar to that in CO_2 except at 0.45 V vs. RHE. The difference between N_2 and CO_2 could be ascribed to the pH value of CO_2-saturated 0.1 M $KHCO_3$ (~6.8) is lower than that in N_2-saturated electrolyte (~8.3).

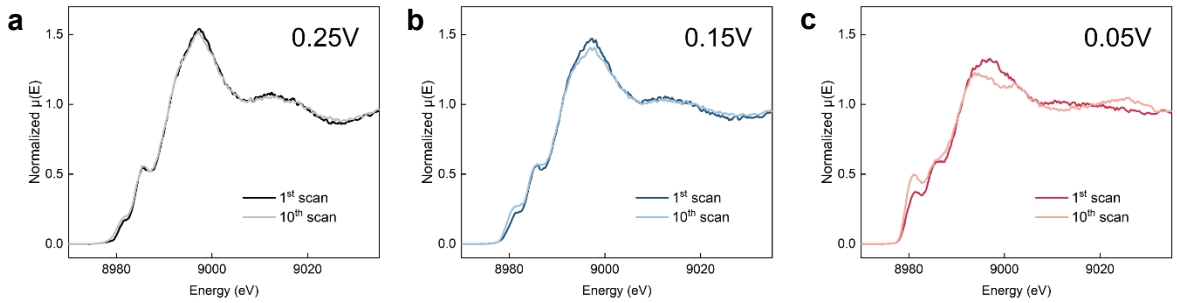

Figure 3.20: The comparison between the first scan and the tenth scan of the CuO nanowire-derived Cu catalysts under different potentials, collected in the HERFD-XAS mode, at (**a**) 0.25 V, (**b**) 0.15 V and (**c**) 0.05 V vs. RHE. At 0.25 V, there was no clear change, but the spectral evolution was clear for 0.15 V and prominent at 0.05 V. These results suggest that the oxide reduction was triggered at 0.15 V, and accelerated at more reductive potentials.

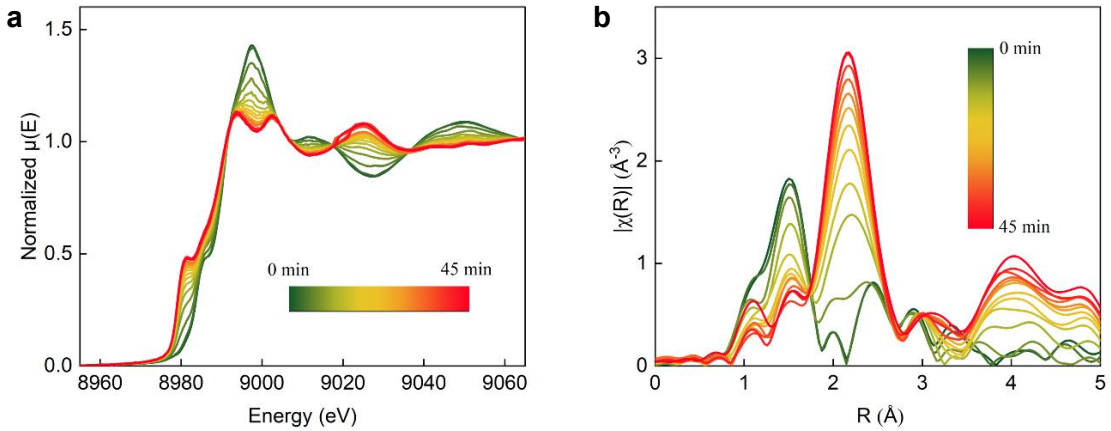

Figure 3.21: *Operando* XAS measurements of CuO nanowire at 0.45V. *Operando* time-resolved (**a**) XANES spectra and (**b**) FT-EXAFS spectra in R space of the CuO nanowire-derived Cu catalysts under 0.45 V vs. RHE from 0 minutes to 45 minutes. All spectra were collected in the CO_2-saturated 0.1 M $KHCO_3$ electrolyte. 0.45 V vs. RHE is the thermodynamic CuO electroreduction potential. Compared with the applied potential of -0.1 V, -0.65 V, and -1 V in Fig. 3.15g, CuO exhibited a considerable slow reduction kinetic under 0.45 V vs. RHE.

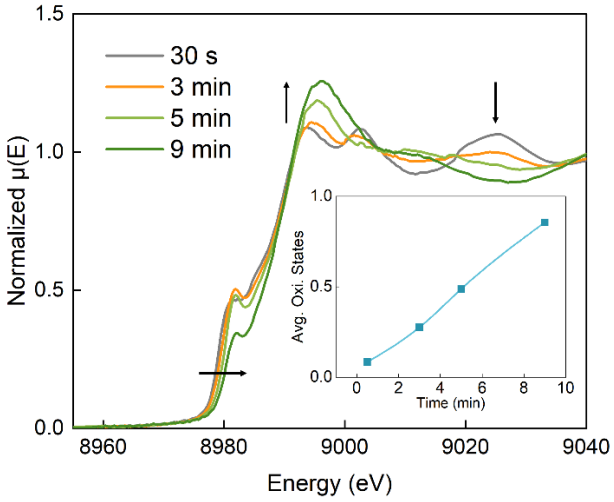

Figure 3.22: *Operando* time-resolved XANES spectra of the CuO nanowire-derived Cu catalysts after chronoamperometry at 0.45 V vs. RHE from 45 minutes. The black arrows indicate the changes at pre-edge, white line intensity and post edge of the spectra. Although all spectra were collected at open-circuit potential in CO_2-saturated 0.1 M $KHCO_3$ electrolyte, the OD-Cu catalysts still gradually oxidized to Cu_2O with average of +0.9 oxidation state after 9 minutes.

There is currently some debate in the field regarding the active sites for oxide-derived Cu catalysts for CO_2RR, with some studies claiming that such catalysts are fully reduced to metallic Cu during operation[180,207,208], and others positing that Cu^+ species are stabilized in the catalyst and serve as active sites for C_{2+} product formation[172,181]. The specific behavior may depend on the precise state of the precatalysts in question. We propose that the reduction of CuO precatalysts is easier than that of Cu_2O, with a lower apparent activation energy, and it reduces directly to metallic Cu without formation of an intermediate or suboxide because the system can reach metastable states instead of forming Cu_2O[209,210]. The boundary of the bicrystal CuO nanowire provides additional oxygen diffusion pathways, which also boosts the reduction kinetics (**Fig. 3.12**). This is consistent with our conclusion that the active sites in the CuO nanowire-derived Cu catalyst are metallic Cu sites formed from the nanocracking process induced by the pristine oxide reduction (**Fig. 3.7** and **3.15**). We also note that signatures of oxide reappear quickly after the potential is released (**Fig. 3.21** and **3.22**), emphasizing the need for operando studies to identify the valence state during operation.

3.6 Structure-performance correlation in CO_2RR

To establish the correlation between our observed catalysts structural dynamics and CO_2RR performance, we conduct electrolysis of the CuO nanowire precatalysts in CO_2-satuated 0.1 M $KHCO_3$ aqueous electrolyte in the same H-type cell design[205] used for XAS measurements (**Fig. 3.23**). Different precatalyst loadings (0.05 to 1 mg cm^{-2}) are evaluated under ambient conditions. The stepwise chronoamperometry measurements reveal that the optimal potential for C_{2+} chemical production is -1.0 V for low loading samples of 0.05 and 0.1 mg cm^{-2} (**Fig. 3.24**). The maximum Faradaic efficiency for the C_{2+} production (FE_{C2+}) and C_{2+}/C_1 product ratios are recorded as ~43% and 1.8 for a catalyst loading of 0.1 mg cm^{-2} (**Fig. 3.25a**). However, both FE_{C2+} and C_{2+}/C_1 ratios decrease significantly for loadings above 0.2 mg cm^{-2} (**Fig. 3.25b** and **Fig. 3.26**). The decrease in C_{2+} product selectivity at higher precatalyst loadings can be explained by the mitigation of CuO reduction due to thicker and less conductive layers, as demonstrated in the post-mortem TEM measurements (**Fig. 3.27**). The precatalyst loading effect implies that the electroreduction of pristine oxide is indispensable for activating OD-Cu for C_{2+} selectivity by creating electrocatalytic active sites[172,173,180,211]. To evaluate the initial process of catalyst activation and its effects on CO_2RR performance, the ECSA and roughness factor of the CuO nanowire-derived Cu catalysts are measured over time for 0.1 mg cm^{-2} loading at -1.0 V (**Fig. 3.25c**). Both the ECSA and roughness factor of the OD-Cu catalysts gradually increase to double their starting values in 30 minutes of operation, concomitant with an improvement of CO_2RR/HER FE ratio. This indicates that, following the initial nanocrack network formation within 30 seconds (**Fig. 3.7c**), the OD-Cu continues to restructure on a longer timescale, which is consistent with the frequently reported Cu restructuring during CO_2RR[71,72,96,183]. As a control experiment, we test pure Cu nanowire catalysts performance in the same H-type cell under 0.1 mg cm^{-2} catalyst loading, and find the FE for C_{2+} products (9.4%) significantly lower than that of the OD-Cu (43%) (**Fig. 3.28**).

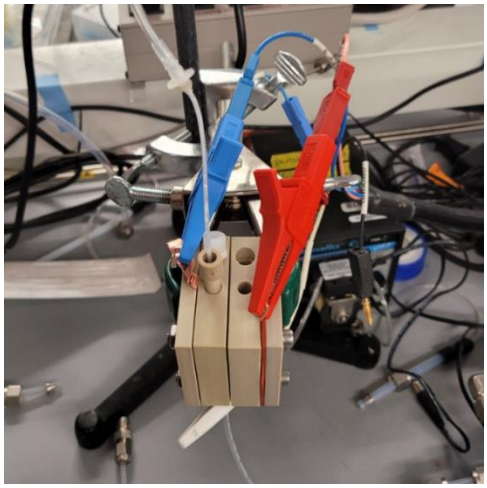

Figure 3.23: Configuration of the H-type cell used for CO_2RR performance testing.

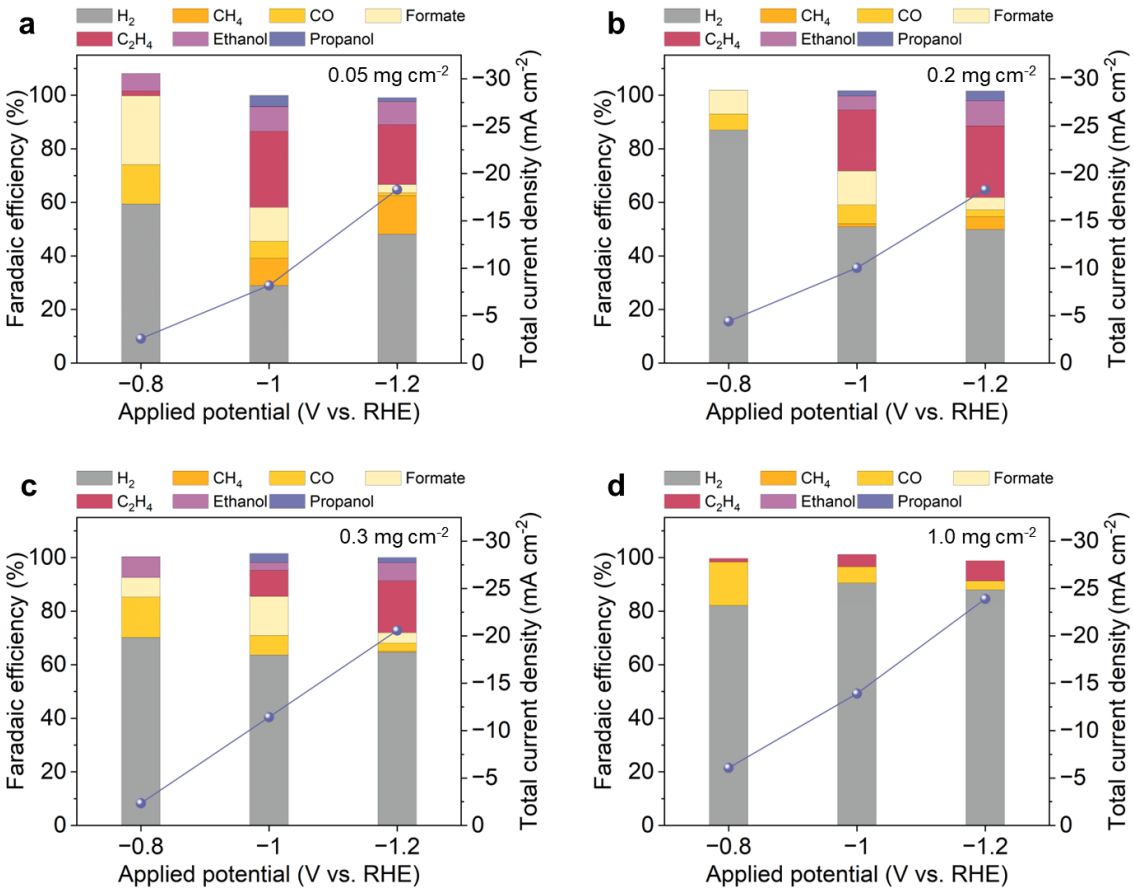

Figure 3.24: Faradaic efficiency and total current density for all CO_2RR products obtained from CuO nanowire-derived Cu catalysts at -0.8 V, -1 V, and -1.2 V vs. RHE with different precatalyst loadings of (**a**) 0.05 mg cm^{-2}, (**b**) 0.2 mg cm^{-2}, (**c**) 0.3 mg cm^{-2}, and (d) 1.0 mg cm^{-2} in an H-type cell.

The 3D morphology of the CuO nanowire-derived Cu catalysts after H-type cell measurements, obtained by cryo-ET, shows a nanowire with highly roughened surface (**Fig. 3.25e**). Segmentation from the 3D structure in **Fig. 3.25e** displays the interior nanocrack network morphology (**Fig. 3.25f**). The nanocracks appear to be larger than EC-TEM results in **Fig. 3.7**, suggesting that propagation of nanocracks and nanocavities has occurred during Cu restructuring. Nevertheless, both boundary and transverse nanocracks are still maintained and observed in the final structure. Additional TEM and EDS confirm the existence of nanocracks (**Fig. 3.29** and **3.30**). By contrast, pure Cu nanowires display less surface roughening after operation, and no nanocracks (**Fig. 3.31**). This suggests that the initial nanocrack formation from reduction of CuO precatalysts provides an important framework for further OD-Cu restructuring that yields more active sites for CO_2RR towards C_{2+} products.

We note that Cu_2O is frequently found from our *ex situ* TEM experiments (**Fig. 3.30**), but is not detected in the *operando* EC-TEM (**Fig. 3.7f** and **g**) or XAS (**Fig. 3.15**) at catalytically relevant potentials. This can be attributed to the inevitable re-oxidation of Cu catalysts as soon as

they are out of operating condition. Indeed, we observe the formation of Cu^+ by operando XAS after releasing the cathodic potential (**Fig. 3.22**), similar to our previous studies[185]. This underscores the importance *of in situ/operando* studies for accurate identification of the catalyst active sites.

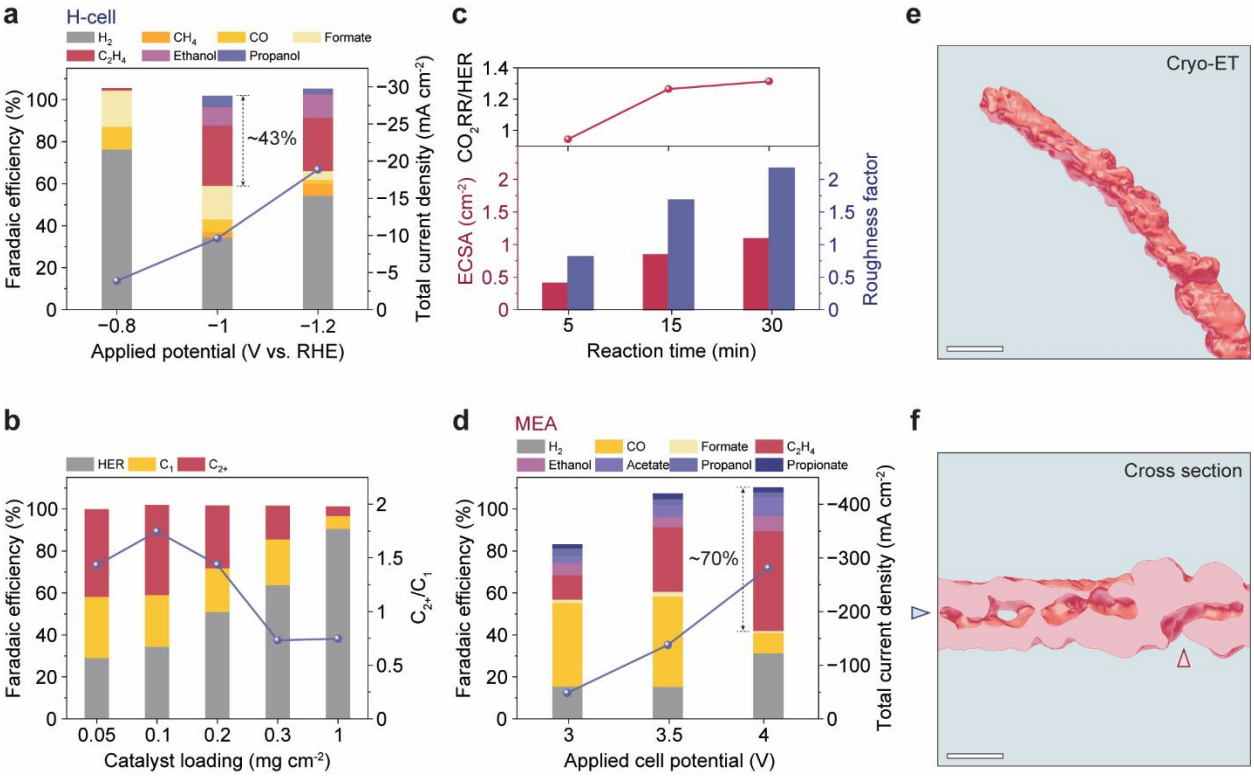

Figure 3.25: Electrochemical CO_2RR performance and structural characterizations of CuO nanowire-derived Cu catalysts. (**a**) FEs for all CO_2RR products and total current density obtained from ensemble of CuO nanowire-derived Cu catalysts with precatalyst loading of 0.1 mg cm^{-2} as a function of the applied electrode potential in an H-type cell. (**b**) FEs for all CO_2RR products grouped as C_{2+} products, C_1 products and H_2 obtained from ensemble catalysts as a function of the precatalyst loading at -1.0 V vs. RHE in an H-type cell. (**c**) Ratio of CO_2RR and HER, ECSA, and roughness factor of as a function of reaction of time with catalyst loading of 0.1 mg cm^{-2} at -1.0 V vs. RHE in an H-type cell. (**d**) FEs for all CO_2RR products and total current density obtained from ensemble catalysts as a function of the applied cell potential in an MEA electrolyzer. (**e**) Cryo-ET reconstruction of an individual CuO nanowire-derived Cu nanoparticle obtained after CO_2RR performance testing in an H-type cell. Scale bar, 100 nm. (**f**) Segmentation of an enlarged area in e showing the porous interior structure with both boundary (blue arrow) and transverse (red arrow) nanocracks. Scale bar, 50 nm.

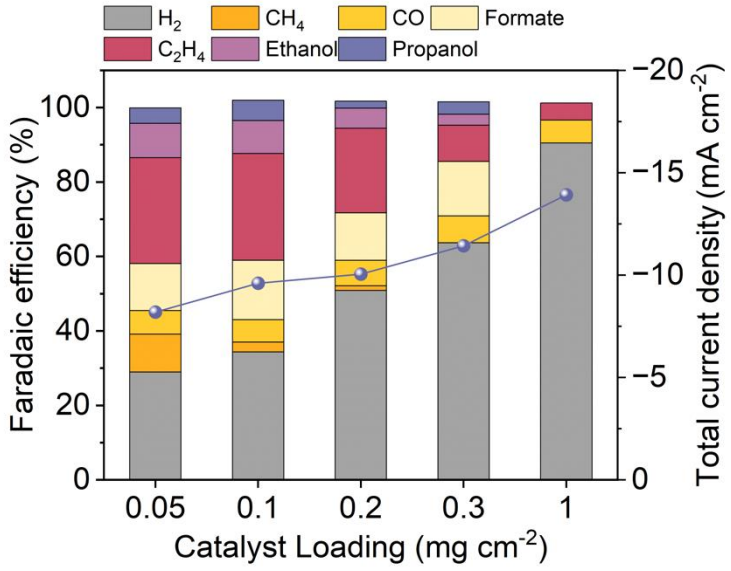

Figure 3.26: Faradaic efficiency and total current density for all CO_2RR products obtained from CuO nanowire-derived Cu catalysts at -1 V vs. RHE with different loading of 0.05 mg cm^{-2}, 0.1 mg cm^{-2}, 0.2 mg cm^{-2}, 0.3 mg cm^{-2}, and 1.0 mg cm^{-2} in an H-type cell.

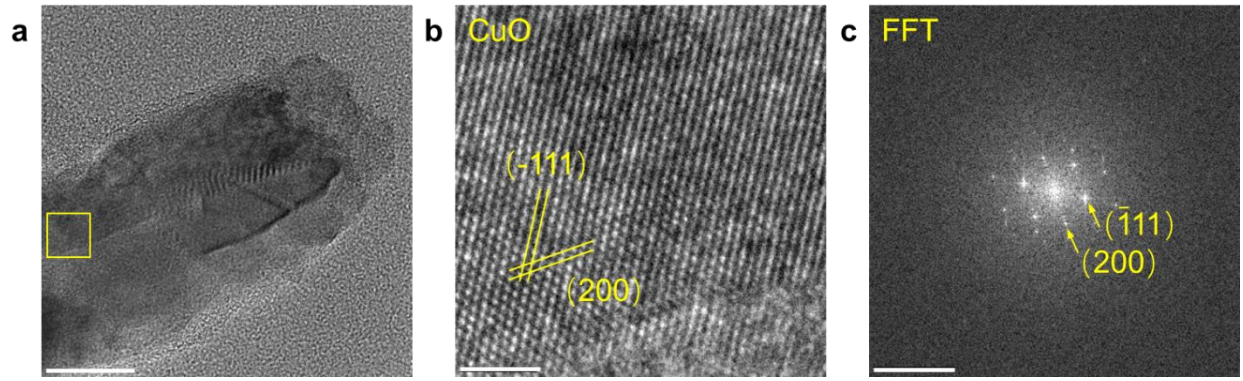

Figure 3.27: Ex situ characterization of CuO nanowire-derived Cu catalysts with high loading. (**a**) Post-mortem TEM measurements of CuO nanowire-derived Cu catalysts with a loading of 1.0 mg cm^{-2} tested in an H-type cell. Scale bar, 20 nm. (**b**) HRTEM image of selected area in (a), showing atomic structure of CuO phase. Scale bar, 2 nm. (**c**) Corresponding FFT patten of (b). Scale bar, 10 nm^{-1}. These results show inadequate reduction of CuO nanowires under a high catalyst loading condition.

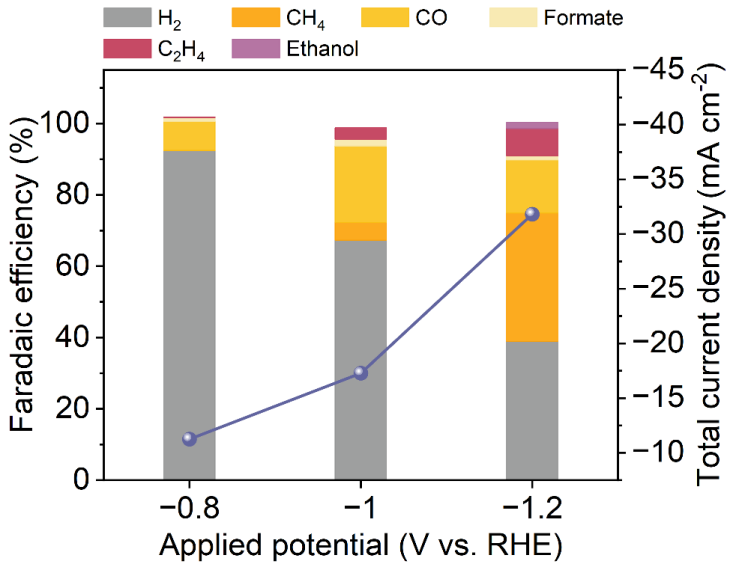

Figure 3.28: Faradaic efficiency and total current density for all CO_2RR products obtained from the Cu nanowire catalysts at -0.8 V, -1 V, and -1.2 V vs. RHE with loading of 0.1 mg cm^{-2} in an H-type cell. Cu nanowires were synthesized using an established method[212].

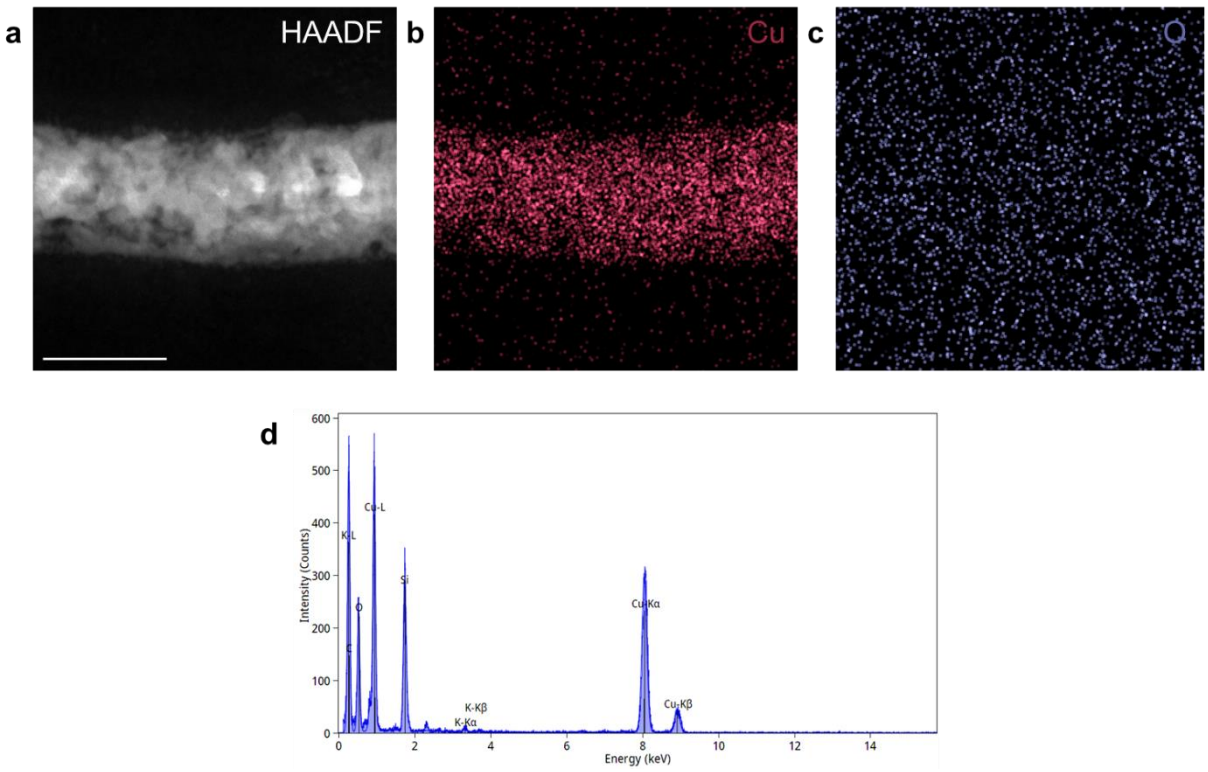

Figure 3.29: EDS measurements of CuO the nanowire-derived Cu catalysts in H-type cell. (**a**) Post-mortem HAADF-STEM image and EDS mapping of (**b**) Cu and (**c**) O of CuO the nanowire-derived Cu catalysts with a loading of 0.1 mg cm^{-2} tested in an H-type cell. Scale bar,

50 nm. (**d**) Corresponding EDS spectra collected from (a). These results show the reduction of CuO nanowire, generating nanocracks with formation of Cu nanograins.

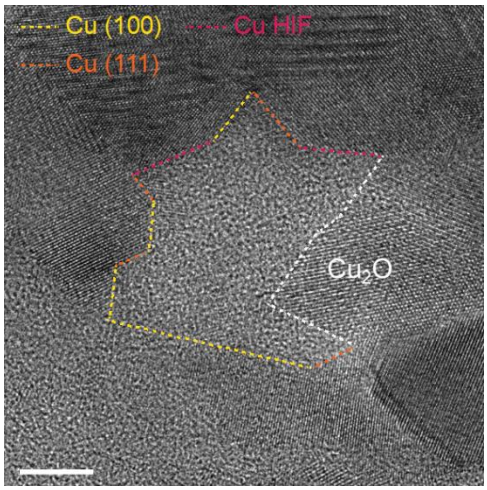

Figure 3.30: Post-mortem HRTEM images of CuO nanowire-derived Cu catalysts with a loading of 0.1 mg cm^{-2} tested in an H-type cell. Scale bar, 5 nm. The morphology of nanocracks is similar to that in the EC-TEM results (Fig. 2f). The metallic Cu nanograins contain different types of facets, including (100), (111), and high index facets (HIF). Additionally, Cu_2O was also detected, which resulted from the inevitable re-oxidation of the OD-Cu catalysts after CO_2RR.

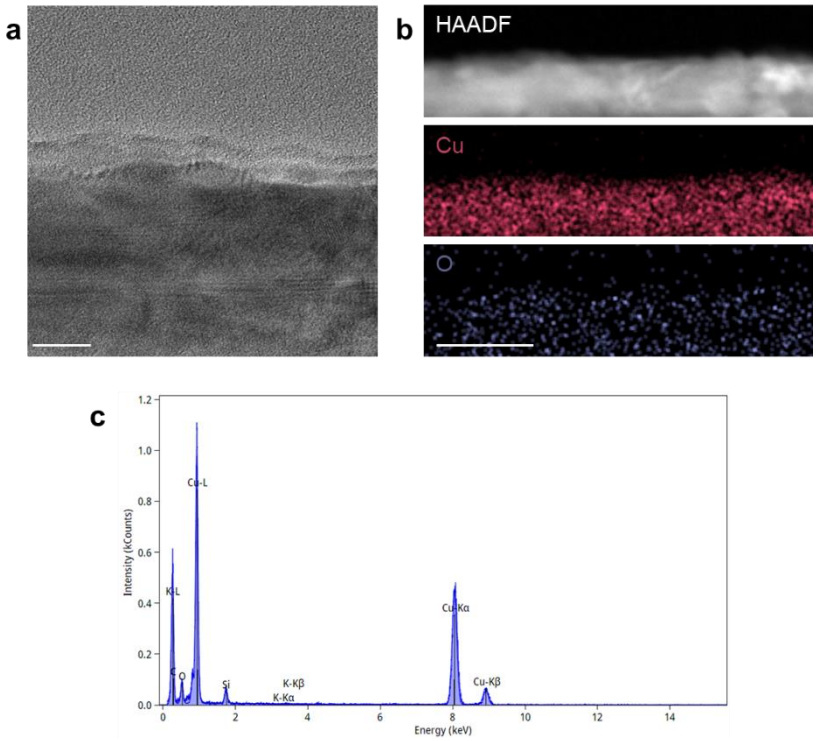

Figure 3.31: EDS measurements of Cu nanowire catalysts. Post-mortem (a) HRTEM image, scale bar 10 nm, (b) HAADF-STEM image and EDS mapping of Cu and O, scale bar, 50 nm, and (c) corresponding spectra of Cu nanowire catalysts with a loading of 0.1 mg cm^{-2} tested in an H-type cell. The Cu nanowires display less surface roughening after CO_2RR operation, with no nanocracks.

To further evaluate the application potential of CuO nanowire-derived Cu catalysts for industrial CO_2RR, we measure their catalytic performance in a 5 cm^2 MEA electrolyzer, which is the next generation electrolysis system (**Fig. 3.32**). The CuO nanowire-derived Cu exhibits ~70% FE_{C2+} selectivity at the optimal current density of ~300 mA cm^{-2} at 4 V (total cell voltage) in the MEA (**Fig. 3.25d**). Such C_{2+} selectivity improvement compared to H-type cells can be ascribed to the working environment that facilitates thorough reduction and activation of CuO inside MEA[213]. The superb performance of CuO nanowires in the MEA with low cost and easy preparation highlights their potential towards CO_2RR in industrial applications. Post-mortem TEM measurements of OD-Cu (**Fig. 3.33**) suggest the nanocracking behavior is general across all catalytically relevant conditions and reactors, including the EC-TEM liquid cell, H-type cell, and MEA.

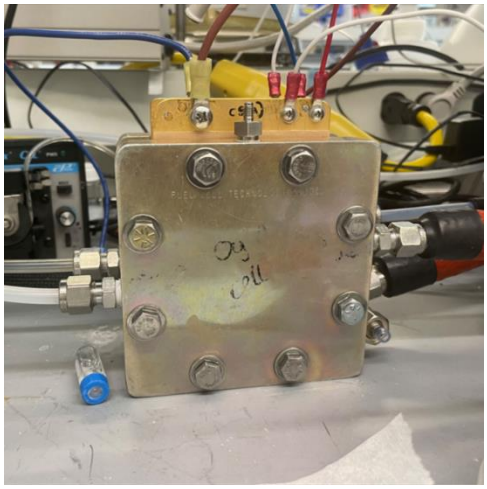

Figure 3.32: Configuration of the MEA electrolyzer used for CO_2RR performance testing.

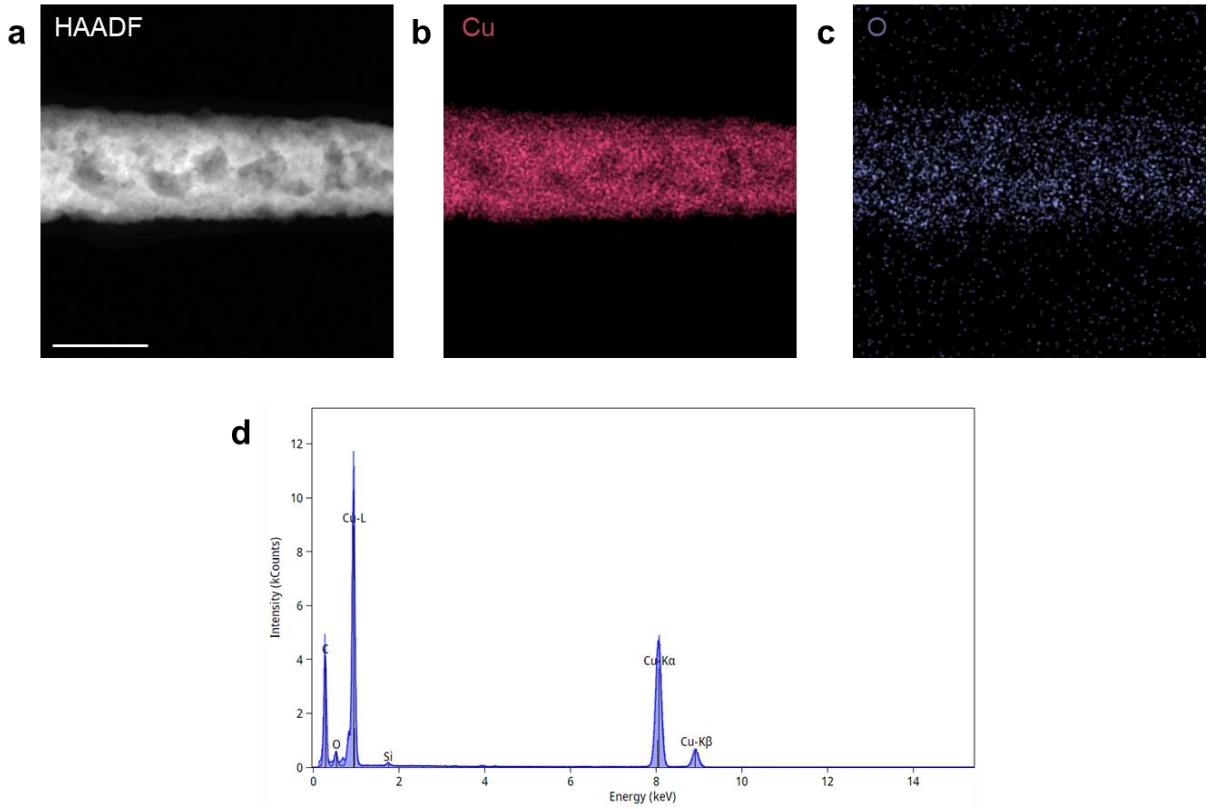

Figure 3.33: EDS measurements of CuO the nanowire-derived Cu catalysts in MEA. Post-mortem (**a**) HAADF-STEM image, EDS mapping of (**b**) Cu and (**c**) O, scale bar, 100 nm, and (**d**) corresponding spectra of CuO nanowire-derived Cu catalysts with a loading of 0.3 mg cm^{-2} tested in an MEA electrolyzer. The nanocracks were still maintained, suggesting the nanocracking behavior is general across all catalytically relevant potentials and reactors.

3.7 Conclusions

In summary, this study systematically uncovers the dynamic structural reconstruction of CuO nanowire-derived Cu, from individual nanowires to ensemble catalysts, through advanced multimodal operando techniques under CO_2RR working conditions. The OD-Cu structures are rich in nanocracks that dictate further dynamic restructuring, generating active sites for C_{2+} products. The formation of nanocrack network during reduction of CuO bicrystal nanowire suggests a means to control catalyst structure. For example, polycrystalline CuO rich in diverse types of grain boundaries can be used as starting materials to generate an intricate architecture of predictable enriched boundary and transverse nanocracks during CO_2RR, boosting the performance by increasing the catalytic active sites. Similar strategies could also apply to other catalytic systems, such as sulfide/halide-derived Cu or others. This work demonstrates an innovative solution towards spatiotemporally resolving the complex and dynamic nature of precatalysts in electrochemical systems, and emphasizes the crucial relevance of applying complementary operando methods such as electron microscopy and X-ray spectroscopy for understanding structure-performance correlations.

Chapter 4

Influence of sub-zero temperature on nucleation and growth of Cu nanoparticles in electrochemical reactions

Cu metal nanostructures have attracted wide interest of study as catalysts for CO_2 reduction reaction and other applications. Controlling the structure and morphology of the nanostructures during synthesis is crucial for achieving the desired properties. Here, we study the temperature effects on the electrochemical deposition of Cu nanoparticles. We found that the size, morphology, nucleation density, and crystallinity of Cu nanoparticles are strongly influenced by the low temperature process. The electrodeposition at low temperature (-20 ºC) results in clusters of assembled small Cu nanoparticles, which is distinctly different from the large individual highly crystalline Cu nanoparticles (~16 nm) obtained from the room temperature process. The differences in Cu nanoparticle morphology and crystallinity are attributed to the variations in reduction reaction rate and surface diffusion. At the low temperature, the reduced reaction rate promotes the formation of multiple nuclei, and low surface diffusion induces poor crystallinity. This study deepens our understanding of low-temperature effects on electrochemical processes assisting the design of diverse hierarchical catalytic materials.

This chapter is adopted from Qiubo Zhang, Jiawei Wan *et al* 's work entitled "Influence of sub-zero temperature on nucleation and growth of copper nanoparticles in electrochemical reactions" from reference 65, with permission to reproduce it in this dissertation from the co-authors.

4.1 Introduction

Cu-based materials have emerged as exciting catalysts for electrochemical CO_2RR, which converts CO_2 into renewable fuels and feedstocks[177,212,214–216]. A variety of C_{2+} products can be achieved during CO_2RR, such as ethylene, ethanol and propanol[217]. The efficiency and selectivity of these catalysts are dependent on the structure and morphology of the Cu catalysts, e.g., the nanoparticle sizes[218,219], configurations[220], crystallinity[221] and oxidation states[222]. Therefore, understanding and controlling of Cu nanomaterials formation during synthesis is essential in order to optimize their catalytic performance.

Compared to many other methods, electrodeposition avoids the high-temperature synthetic procedures, thus it has been considered as an ideal way for the preparation of hierarchically structured catalysts[223,224]. In electrodeposition, there are many factors that may affect the nucleation and growth of nanocrystals and result in diverse structure and morphology of the final products[225]. For example, the current density can affect the nucleation density, size and shape of the deposited nanocrystals[226], while the pH value affects the structure and properties of the metal deposits. Additives in the solution can inhibit the formation of lithium dendrites during battery operation[68]. Although there have been reports on temperature impacts on electrodeposition[227,228], it is not well understood how low temperature affects the nucleation and growth of Cu nanoparticles. This may arise from two main reasons. First, it is difficult for general electrolytes to maintain a liquid state and good electrical conductivity at low temperatures. Second, it is challenging to characterize the products since they may change after being removed from the low temperature environment.

Here, we synthesize hierarchical Cu nanostructures with Cu nanoparticles attached to the Cu nanowires at both sub-zero temperature (-20 ºC) and room temperature (20 ºC). The Cu nanostructures are characterized using TEM with different techniques, including liquid cell electron microscopy, cryo-EM, etc. We found that sub-zero temperature impacts the crystallinity and morphology of the Cu nanoparticles. The different growth modes of Cu nanoparticles at the low temperature, such as nucleation and assembly of multiple small Cu nanoparticles to form Cu nanoclusters, are attributed to the reduced reaction rate. The low surface diffusion rate of adsorbed atoms at the low temperature is considered as the main factor responsible for the poor crystallinity.

4.2 Experimental setup and characterization

4.2.1 Chemicals

Copper (II) chloride ($CuCl_2$, 99.999%), D-(+)-glucose (≥99.5%), hexadecylamine (98%), ethanol (≥99.0%), hexane (95%) and commercial electrolyte (1 M lithium hexafluorophosphate ($LiPF_6$) in ethylene carbonate (EC) and dimethyl carbonate (DEC) solution (volume ratio 1:1)) were all purchased from Sigma-Aldrich. All the chemicals were used without purification. An ultrapure purification system (Milli-Q advantage A10) produced the deionized water (18.2 MΩ cm) used to make the solutions.

4.2.2 Preparation of Cu nanowires

In a standard synthesis of the Cu nanowires, 17 mg of $CuCl_2$, 50 mg of D-(+)-glucose and 180 mg of hexadecylamine were mixed with 10 ml of deionized water in a glass vial. The final solution was sonicated for 30 min at room temperature. The vial was then transferred into an oil bath and heated at 100 °C for 6 h under magnetic stirring. The synthesized Cu nanowires were washed five times with hexane/ethanol (1:1 volume) and collected by centrifuge at 9500 rpm for 5 min.

4.2.3 TEM imaging

The TEM experiments were performed on a FEI ThemIS aberration-corrected TEM at the Molecular Foundry (MF), Lawrence Berkeley National Laboratory (LBNL). The microscope was operated at 300 keV with a Super-X energy dispersive EDS detector, allowing for rapid chemical identification. The cryo-EM imaging was performed by using a Gatan 915 cryo-transfer holder.

4.3 Electrodeposition performed at room and sub-zero temperature

We conducted the experiments with a well-designed device to realize electrochemical and sub-zero temperature control. The schematic illustration of the experimental setup is shown in **Fig. 4.1a**. First, Cu nanowires were prepared in advance and loaded onto a carbon film-supported TEM copper grid. Then, the copper grid was connected to the platinum anode, and the cathode was made with copper. The two electrodes were connected to an electrochemical workstation and immersed into a 5 mL commercial electrolyte of 1.0 M $LiPF_6$ in ethylene carbonate/diethyl carbonate (EC/DEC=50/50 (v/v)). We choose EC/DEC mixed solution as the electrolyte because of its lower freezing point compared to aqueous solution[229], which helps to maintain a liquid state and good electrical conductivity even at sub-zero temperature. After that, we sealed the electrolyte in a ceramic container surrounded by an insulating device made of polystyrene to control the temperature. Liquid nitrogen was used to cool down the insulation device to a desired sub-zero temperature, at which can be maintained for a few minutes because of the low thermal conductivity of polystyrene (0.033 W/(m·K)).

In the experiments, we use constant voltage operations at 2 V for 90 seconds for experiments at room temperature (20 ℃) and sub-zero temperature (-20 ℃). The temperature was measured in real time with an electric thermal detector. As shown in **Fig. 4.1b**, the current is stable at 0.007 mA at 20 ℃ and 0.002 mA at -20 ℃. Current density is lower at the low temperature because ion migration slows down in the electrolyte.

To further find out the differences in electrolyte structure at different temperatures, we used liquid cell TEM combined with cryo-EM techniques to image electrolytes at 20 ℃ and -20 ℃. TEM images and selected area electron diffraction (SAED) patterns of the electrolyte at 20℃ and -20 ℃ are shown in **Fig. 4.1c** and **d**. We loaded a droplet of electrolyte (1.0 M $LiPF_6$ in EC/DEC=50/50 (v/v)) on one carbon film and it was sandwiched by another carbon film to form thin liquid cell. At room temperature, no diffraction spot is found in the diffraction pattern which suggests the electrolyte presents a homogeneous liquid structure. To achieve the low temperature for liquid cell TEM imaging, we used the cryo-EM sample stage that can be cooled down and stabilized at -20 °C. The TEM image shows phase separation of the electrolyte at -20 °C, which consists of both liquid and solid phases. The corresponding diffraction spots match the {111} and

{022} crystal facets of solid EC. At low temperatures, solid EC precipitates out of the liquid phase electrolyte and the electric conductivity of the electrolyte decreases.

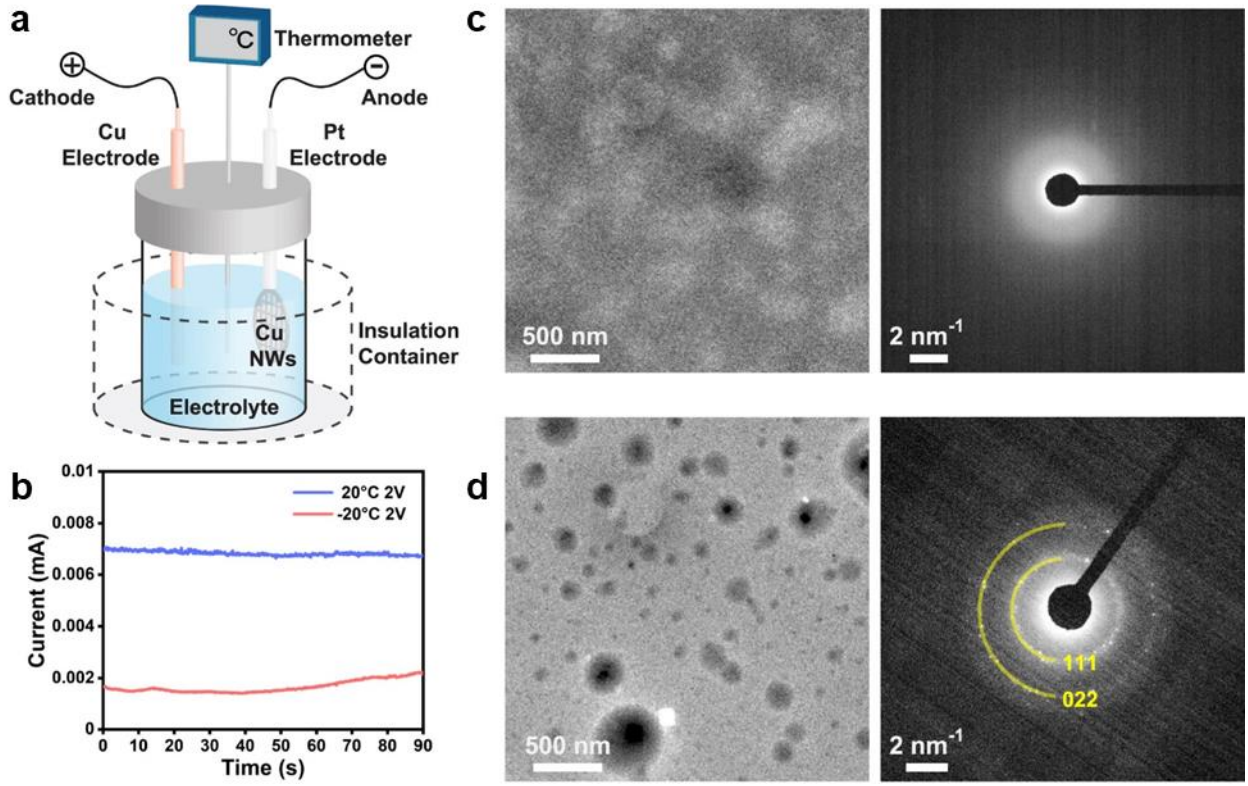

Figure 4.1: Experimental setup and characterization of electrolyte at room temperature (20 ºC) and sub-zero temperature (-20 ºC). (**a**) A schematic diagram of experimental setup. (**b**) Current vs. time plots of the electrodeposition processes at different temperatures. (**c**) TEM and electron diffraction images of the electrolyte in a carbon film liquid cell at 20 ℃. (**d**) TEM and electron diffraction images of the electrolyte in a carbon film liquid cell at -20 ℃. Solid precipitations are found in the electrolyte.

4.4 Structural characterization of as-prepared Cu nanowires

We characterized the as-prepared Cu nanowires to facilitate the comparison of samples before the electrodeposition (**Fig. 4.2**). The synthesized Cu nanowires typically display a fivefold twin with the <110> axial direction and {100} side facets[212,230]. A low magnification TEM image demonstrates its one-dimensional wire structure with an average diameter of about 30 nm (**Fig. 4.2a** and **Fig. 4.3**). The length of the Cu nanowires ranges from hundreds of nanometers to several micrometers. **Fig. 4.2b** is the HRTEM image of the Cu nanowires. The atomic resolution image (**Fig. 4.2c**) is enlarged from the inset box in **Fig. 4.2b**. It shows the lattice spacing of Cu {111}, {002} and {200}, which is consistent with the <110> axial-growth direction of the Cu nanowires. Also, FFT pattern of the yellow square area showing Cu single crystalline structure (**Fig. 4.4**). HAADF-STEM image and EDS mapping (**Fig. 4.2d**) also confirms the successful synthesis of Cu

nanowires. We focus on chemical mapping of the distribution of copper (Cu), carbon (C), and oxygen (O), which shows nanowires of pure copper without noticeable oxidation.

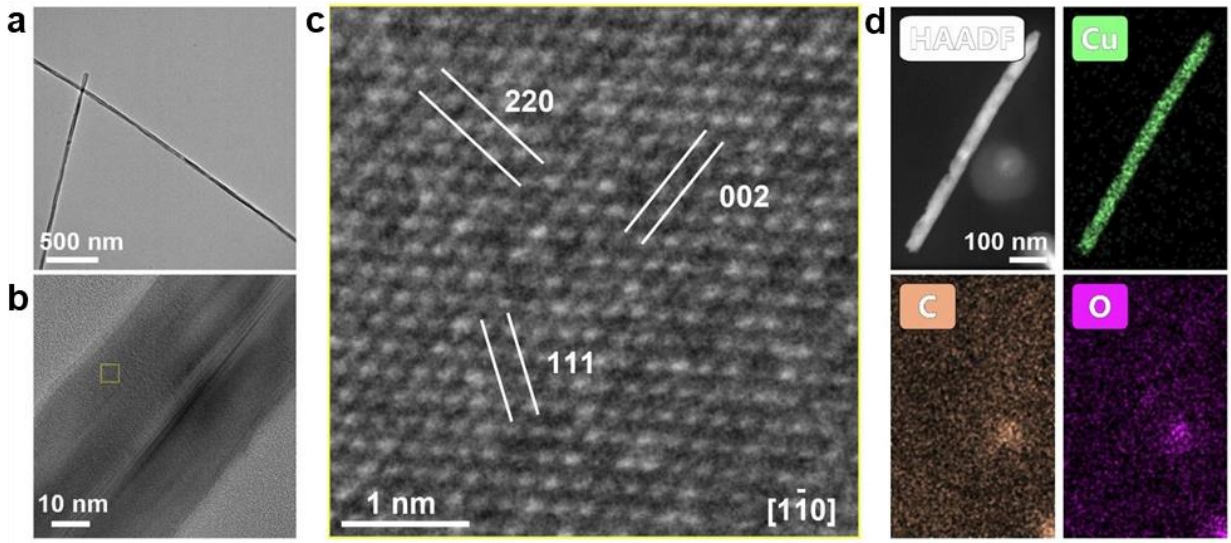

Figure 4.2: Structural characterization of the as-prepared Cu nanowires. (**a**) Low magnification TEM image of the Cu nanowires. (**b**) HRTEM image of one Cu nanowire. (**c**) The zoom-in image of the yellow box area in (b) showing the crystal orientation of the nanowire. The zone axis is [110]. (**d**) STEM and EDS elemental mapping of Cu nanowire: HAADF image, Cu map, C map and O map.

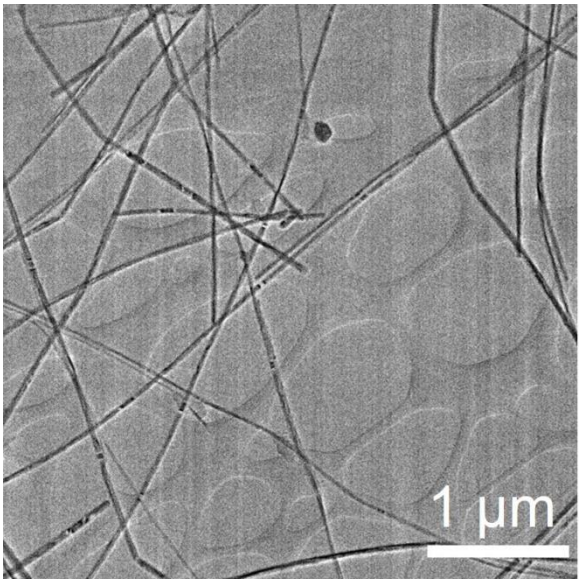

Figure 4.3: Low resolution TEM image of the Cu nanowires.

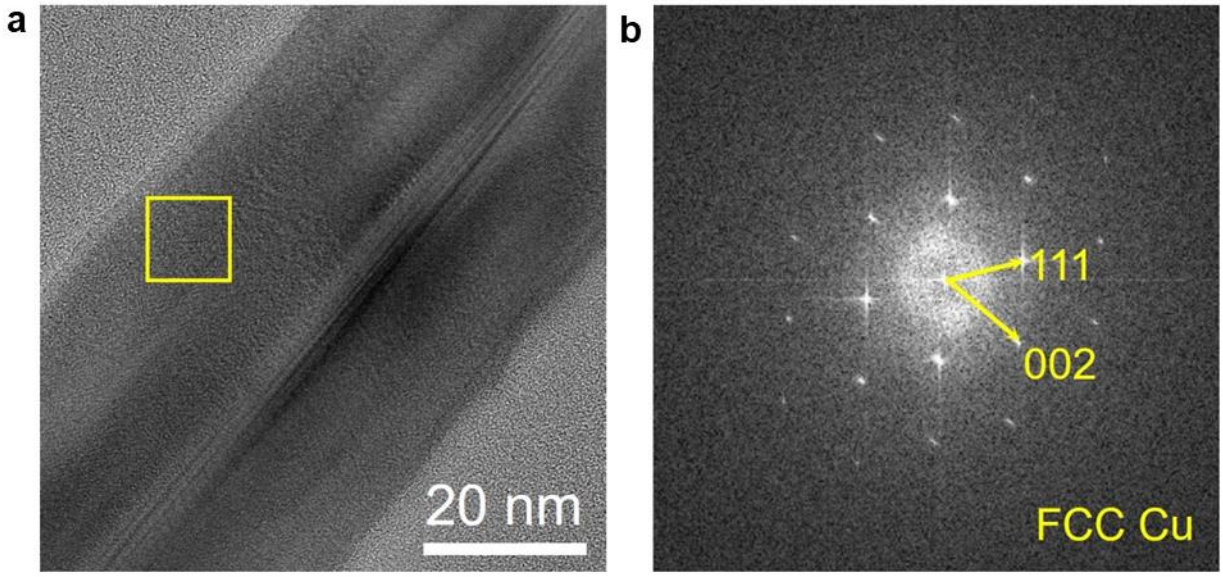

Figure 4.4: Characterization of Cu nanowire. (**a**) HRTEM image of one nanowire. (**b**) FFT pattern of as prepared Cu nanowire from the yellow square area showing single crystalline structure.

4.5 Electrodeposition of Cu nanoparticle on Cu nanowire at room temperature

After electrodeposition, we obtained two kinds of hierarchical structures depending on the temperature and named them Cu hierarchical nanoparticle/nanowire (NP/NW) structure and nanocluster/nanowire (NC/NW) structure. Electrodeposition at room temperature (20 ℃) produces individual nanoparticles attached to the nanowire, forming NP/NW hierarchical structure, as shown in **Fig. 4.5a**. Although the sizes of these nanoparticles are not uniform spanning from 10 nm to 22 nm, the average diameters are about 16 nm (**Fig. 4.6**). The HRTEM images show that these nanoparticles have good crystallinity. According to their crystal structures, they can be divided into five-fold twin crystals and single crystals (**Fig. 4.5b** & **e**). The HRTEM image and the corresponding FFT pattern of the five-fold twin show that the twin boundaries belong to (111) crystal facets (**Fig. 4.5c**). An enlarged image of the interface between nanoparticles and nanowires (**Fig. 4.5d**) shows that there is that there is no obvious dislocation or lattice distortion at the interface. Strain located at the twin boundary of the five-fold twin can be found, which might be due to the slight changes in lattice orientation.

The single-crystal particles are almost spherical. The corresponding FFT pattern shows that there is only one set of diffraction spots, and the crystal structures of nanoparticle and nanowire substrate perfectly match (**Fig. 4.5f**). The enlarged image (**Fig. 4.5g**) of the interface further confirms that the nanoparticles and nanowires are integrated, with no detectable differences in the lattice structures. The EDS spectrum verified that the particles only contain copper element and the appearance of the C peak is caused by the carbon film support (**Fig. 4.7**). **Fig. 4.5h** shows the distribution of the elements. Copper is evenly distributed in the material.

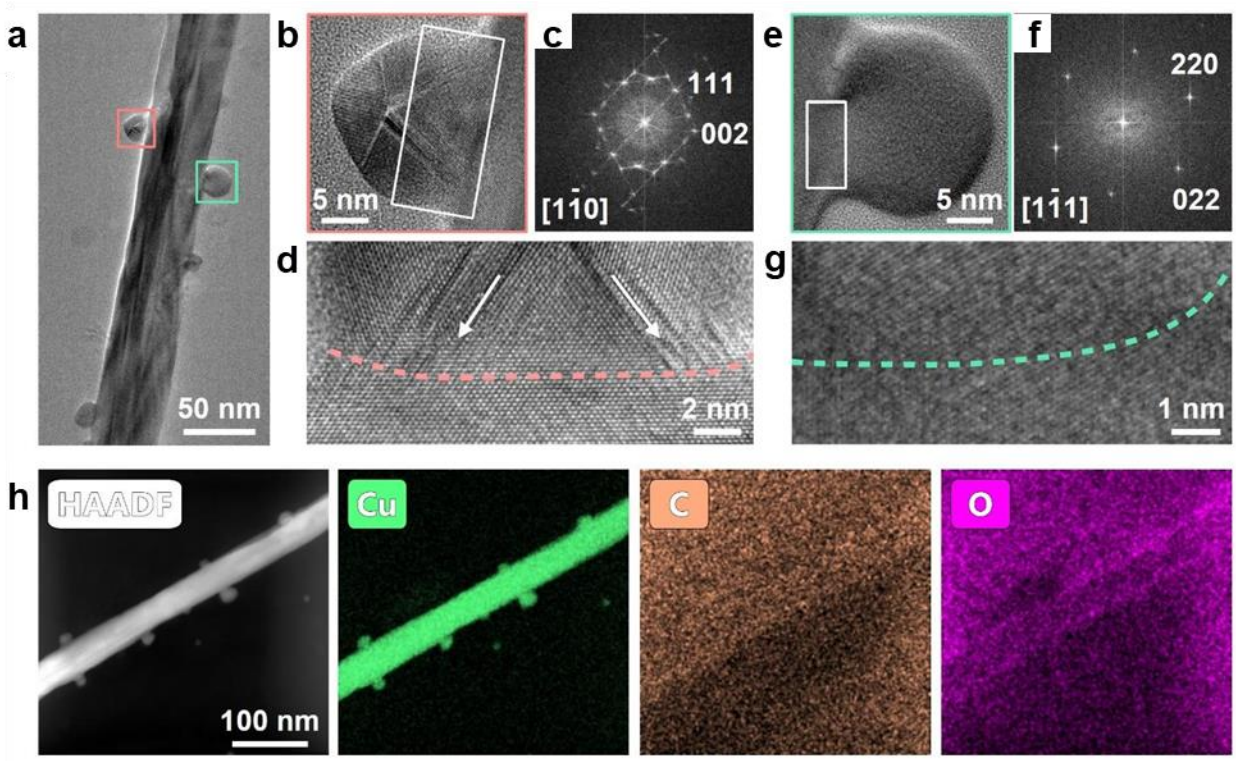

Figure 4.5: Structure characterization of the hierarchical Cu nanoparticle/nanowire nanostructure formed at room temperature. (**a**) Low magnification TEM image of the hierarchical Cu nanoparticle/nanowire nanostructure. (**b**) The zoom-in image of the pink box in (a) shows that the nanoparticle with a five-fold twin structure. (**c**) The corresponding FFT pattern of (b). (**d**) The zoom-in image of the white box area in (b) showing the interface between nanoparticle and nanowire. The pink dotted line marks out the interface. (**e**) The zoom-in image of the green box in (a) shows that the nanoparticle with a single crystal structure. (**f**) The corresponding FFT pattern of (e). (**g**) The zoom-in image of the white box area in (e) showing the interface between single crystal nanoparticle and nanowire. The green dotted line marks out the interface. (**h**) STEM and EDS elemental mapping of hierarchical Cu nanoparticle/nanowire nanostructure: HAADF image, Cu map, C map and O map.

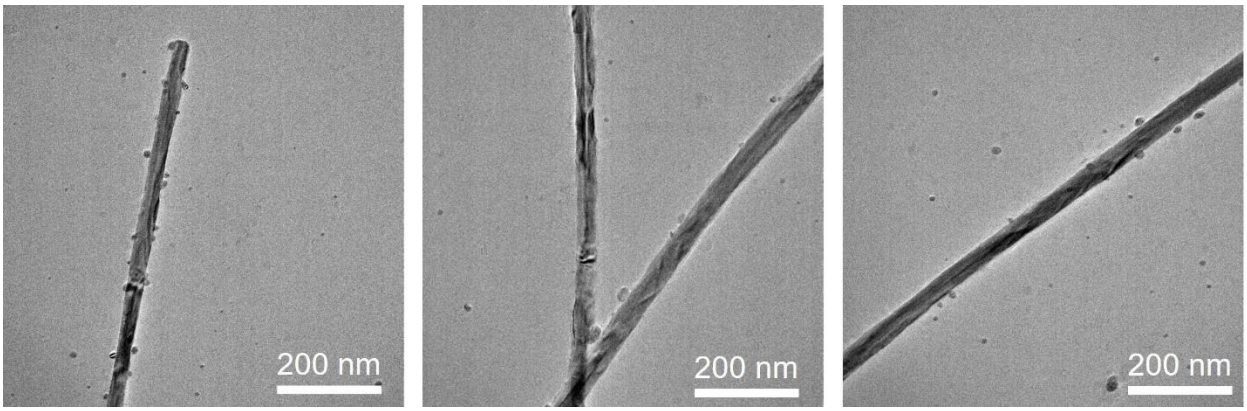

Figure 4.6: Low resolution TEM image of the hierarchical Cu nanoparticle-nanowire nanostructure.

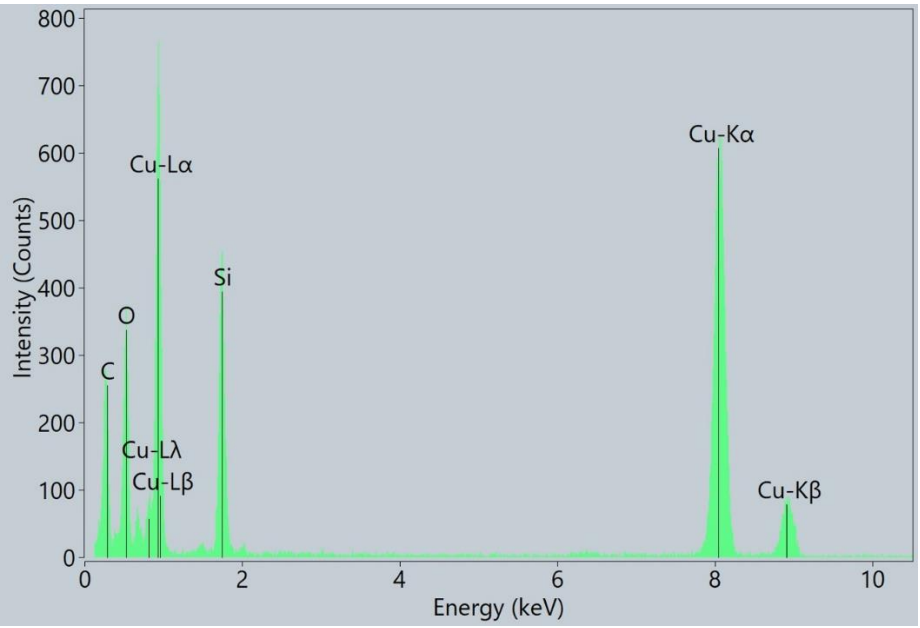

Figure 4.7: EDS spectra of Cu nanostructures formed at room temperature with large crystalline Cu nanoparticles attached to the Cu nanowires.

4.6 Electrodeposition of Cu nanoparticle on Cu nanowire at sub-zero temperature

In contrast, at -20 ℃, the morphology of Cu deposits are completely different and Cu clusters are found. Because copper is an active metal under electron beam irradiation[231], to avoid potential alteration by electron beam irradiation during imaging, cryogenic TEM imaging was adopted. As shown in **Fig. 4.8a**, we find that the deposited Cu tends to form nanoclusters rather than individual nanoparticles. These nanoclusters are the assembly of smaller nanoparticles and they connect with the nanowire forming hierarchical Cu NC/NW nanostructure. Compared with nanoparticles formed at room temperature, the nanoclusters are smaller in diameter (about 9 nm), and the nucleation density of nanoclusters is greater with the assembled smaller Cu nanoparticles. HRTEM image and the corresponding FFT pattern reveal the poor crystallinity of the nanoclusters (**Fig. 4.8b** and **Fig. 4.9**). Within a cluster, both crystalline regions and disordered regions are found. The crystalline part of the cluster is highlighted by performing the inverse Fourier transform of the diffraction spots in the FFT. Subsequently, the image showing the crystalline regions was dyed with orange color. As shown in **Fig. 4.8c**, the aggregation of nanoparticles within a nanocluster has no preferred orientation. FFT pattern of Cu nanoclusters obtained from **Fig. 4.8b** also shows randomly oriented polycrystalline Cu clusters (**Fig. 4.9**). We can also find that the neck between the nanoclusters and the nanowires is narrower. Combining with the observed disordered structure, it implies that the interfacial bonding is weak. The EDS mapping in **Fig. 4.8d** shows that only Cu exists in the sample. In summary, compared with the NP/NW structure formed at room temperature,

the Cu NC/NW nanostructure formed at low temperature show smaller sizes, the clusters of assembled small Cu nanoparticle, reduced crystallinity and weakened connection to the Cu nanowire.

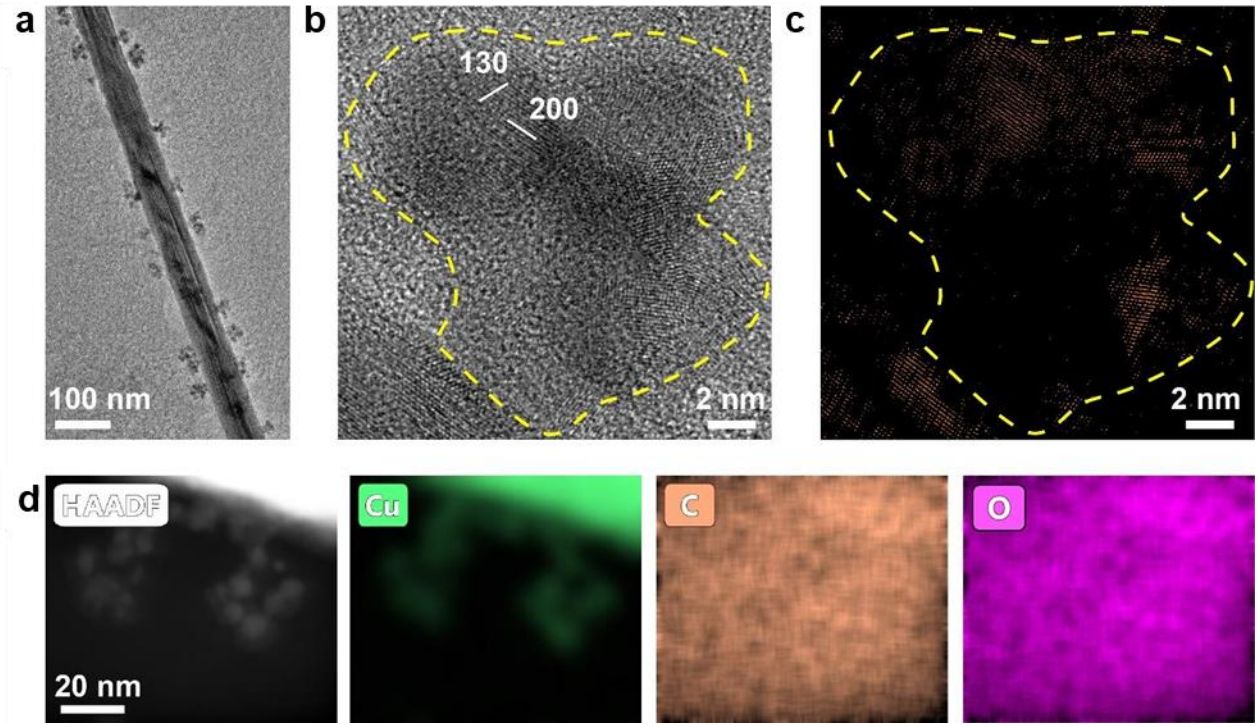

Figure 4.8: Structure characterization of the hierarchical Cu nanocluster/nanowire nanostructure formed at -20 °C. (**a**) Low magnification TEM image of the hierarchical Cu nanocluster/nanowire nanostructure. (**b**) HRTEM image of several gathered Cu nanoclusters shows the crystallinity of the clusters is not perfect. (**c**) The inverse FFT of the HRTEM image highlight the crystal part. The yellow dotted line marks the edge of the cluster. (**d**) STEM and EDS elemental mapping of the hierarchical Cu nanocluster-nanowire nanostructure: HAADF image, Cu map, C map, and O map.

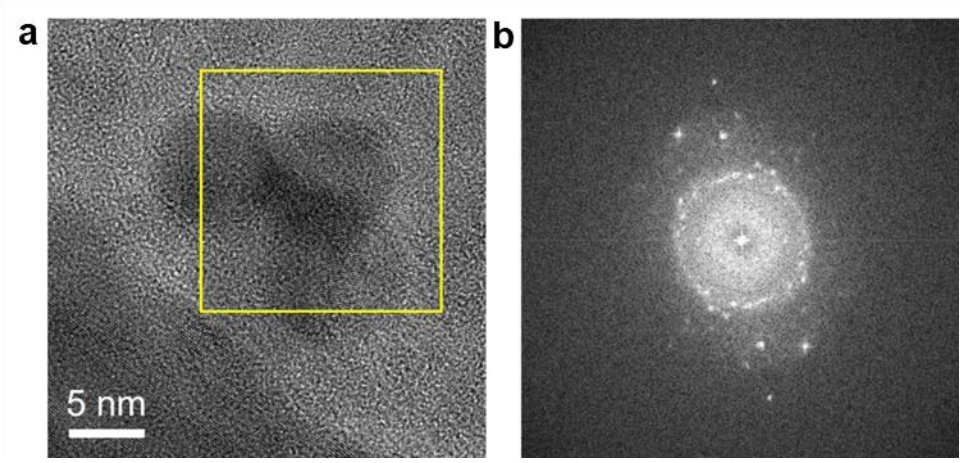

Figure 4.9: Characterization of hierarchical Cu nanocluster-nanowire nanostructure. (**a**) TEM image of the hierarchical Cu nanocluster-nanowire nanostructure. (**b**) FFT pattern of Cu nanoclusters obtained from the yellow square area at low temperature (-20 ℃). It shows random oriented polycrystalline Cu clusters.

4.7 Growth mechanism of Cu nanoparticle at different temperatures

Regarding the size of Cu nanoparticles, previous studies have shown that both temperature and current density impact the size of the deposited particles in electrochemical processes by changing the overpotential[226,232]. Classical nucleation equations can be used to understand the dependence of Cu particle sizes on the overpotential. Assuming isotropic surface energy, the critical radius (r_{crit}) of nucleation can be described as it follows[226,232]:

$$r_{crit} = 2\Upsilon V_m / F|\eta| \qquad (1)$$

Where F is Faraday's constant, Υ is the surface energy of the Cu-electrolyte interface, V_m is the molar volume of Cu, and η is the electrochemical overpotential. This equation is also applicable to express the critical nuclei size in heterogeneous nucleation[232,233]. Obviously, the nuclei size is inversely proportional to the electrochemical overpotential. It has been demonstrated in previous studies that the nucleation overpotential increases at lower temperatures[228] , resulting in smaller metal nuclei. Furthermore, as predicted by the Butler−Volmer electrode kinetics relationship between the current density and electrode potential, the current density decreases as the nucleation overpotential decreases[232]. Thus, under low current density conditions at the low temperature, the nuclei sizes are expected to be larger. However, in our experiment, the nucleation size is smaller corresponding to a low current density at -20 ℃. (**Fig. 4.10** and **4.11**). Therefore, we conclude that the effect of temperature on the nucleation overpotential is larger than the influence of the current density.

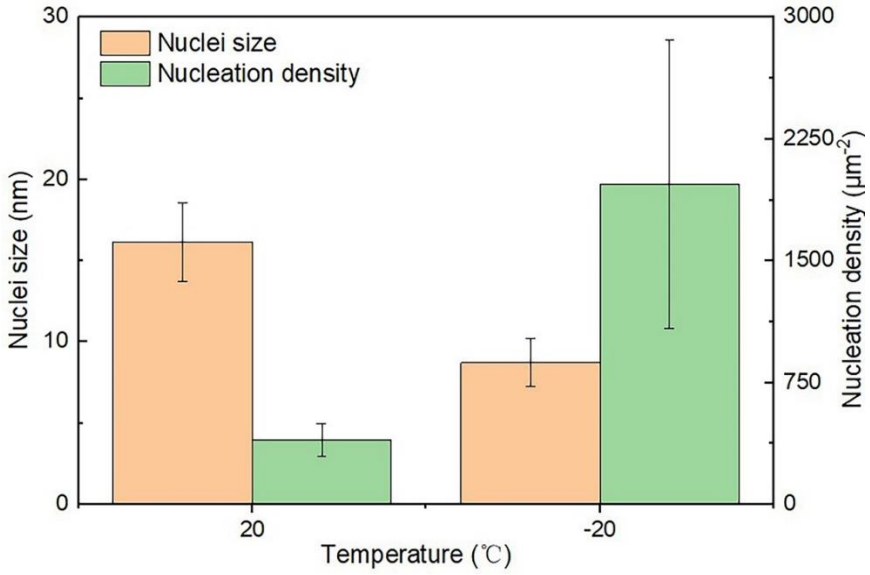

Figure 4.10: Nuclei size and nucleation density of Cu nanoparticles at 20 ℃ and -20 ℃.

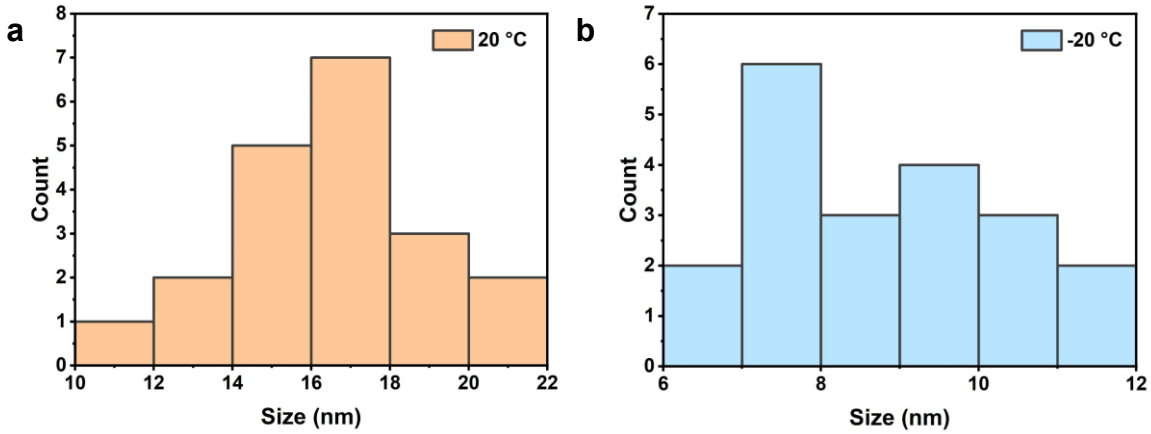

Figure 4.11: Histograms of Cu nanoparticles sizes at (a) 20 ºC and (b) -20 ºC.

To understand the differences in particle aggregation, interfacial bonding and crystallinity, we analyzed the entire process. The metal electrodeposition process usually includes three steps. For the first step, previous studies have proved that low temperature can reduce the ion diffusion coefficient. Similarly, nucleation overpotential increases with the decreasing temperature, the electroreduction reaction at the solid-liquid interface is more difficult to take place. Regarding to the third step, according to the surface diffusion theory, the diffusion coefficient D is given by:

$$D = \left(ve^{\frac{-E_{diff}}{K_B T}}\right) a^2/z \qquad (2)$$

Where v is the attempt frequency, T is the absolute temperature, K_B is Boltzmann constant, E_{diff} is the potential energy barrier for diffusion, and a is the distance per jump. z=2 for one dimensional diffusion, z=4 for two-dimensional diffusion, and z=6 for three-dimensional diffusion.

At room temperature, Cu electrodeposition is limited by the diffusion of ions in the solution. As shown in **Fig. 4.12a**, the Cu ions in the solution diffuse to the electrolyte/electrode interface under the electric bias, then reduced to adsorbed Cu atoms. The newly-born adsorbed metal atoms diffuse along the nanowire surface and aggregate with other newly-born atoms to form nanocrystals. Because the surface diffusion of Cu atoms is relatively fast at room temperature, they can find the lowest surface energy sites, resulting in the epitaxial formation of independent single crystal nanoparticles on the nanowires.

At low temperatures (**Fig. 4.12b**), although the rate of all three steps will decrease, the decrease of the reaction rate is more serious than the diffusion rate. Therefore, the whole process becomes limited by the reaction rate. The Cu ions diffuse to the liquid/solid interface and are reduced to adsorbed atoms. The first formed adsorbed atoms cannot diffuse rapidly result in small contact area between nanoclusters and nanowires. The following ions cannot be reduced in time due to the restriction of the reaction, so they will gather near the surface of the nanoclusters and nucleate again to form a new cluster after the concentration reach to a critical value. Due to the surface diffusion limitation of the adsorbed atoms, the newborn surface atoms can't reach the lowest energy positions and are randomly fixed at the reaction sites, resulting in poor crystallinity. This qualitatively explain the observed Cu nanoclusters formation at the sub-zero temperature.

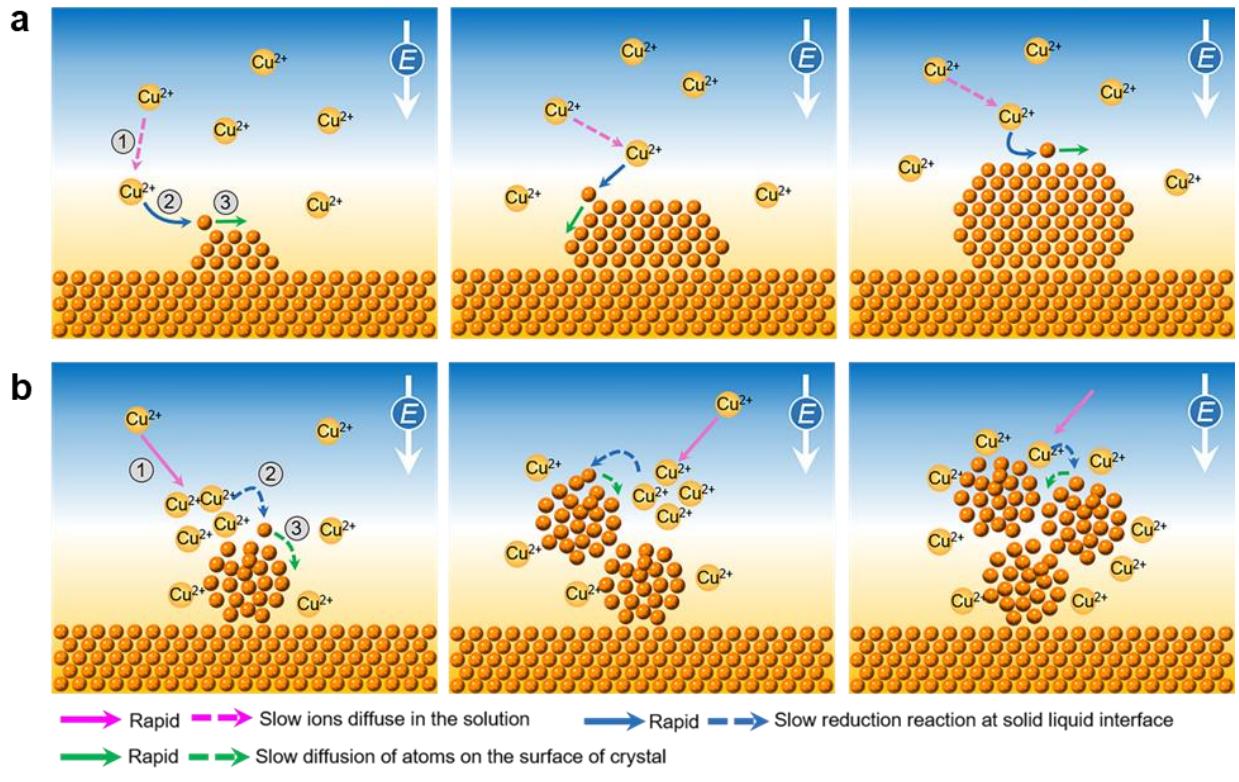

Figure 4.12: Schematic illustrations of two kinds of electrochemical growth mechanisms of copper metal. (**a**) The growth of individual large crystalline Cu nanocrystals is limited by the diffusion of ions in the solution at room temperature. (**b**) The growth of Cu nanoclusters with smaller and weaker interfaces is limited by the reduction reaction at the electrolyte/metal interface at -20 ℃.

4.8 Conclusions

In conclusion, we have demonstrated the temperature-dependent structure diversity of copper nanoparticles from electrodeposition. The electrodeposition at sub-zero temperature leads to the growth of Cu clusters with smaller Cu nanoparticles. The particle size, morphology, crystallinity and connection to the substrate (Cu nanowire) are distinctly different from those obtained at the room temperature. The reduced reaction rate results in multi-nuclei and weak bonding at the interfaces. The decreased surface diffusion rate at the low temperatures may also induce poor crystallinity of Cu clusters. This study deepens our understanding of nucleation in nanostructures and sheds light on the governing factors in the electrodeposition of metal nanoparticles and nanoscale dynamic processes.

Chapter 5

Visualization of nanomotor's directional movement by *in situ* liquid cell TEM

Nanomotors are miniaturized devices capable of converting energy into movement with many applications (i.e., drug delivery, chemical sensing, environmental remediation, etc.). Chemical reaction is widely used to create the motion of synthetic nanomotors via bubble propulsion, self-electrophoresis, and self-diffusiophoresis. The reaction can be spontaneous or triggered by external stimulus (i.e., light, electrical field, etc.). In this work, we report cadmium chloride tetrahydrate ($CdCl_2 \cdot 4H_2O$) nanomotors with remarkable directional movement under electron beam irradiation via self-diffusiophoresis using *in situ* liquid cell TEM. Unlike prior work where asymmetric coverage of active materials were applied to the structural design, surface crystal facets asymmetry was introduced into single $CdCl_2 \cdot 4H_2O$ material with the differences in chemical reactivity. When exposed to the electron beam, the nanomotors show directional movement in an aqueous solution. As the nanomotor morphology changes, the speed of movement also changes. We explore the origin of the directional motion of nanoparticles by carefully examining the dynamic movement, the asymmetric configuration with different crystal facets, and the chemical reactions. Finite element simulation of the electric field and fluid velocity distribution around the nanomotor assists our understanding of ionic self-diffusiophoresis as a driving force for the nanomotor movement. $CdCl_2 \cdot 4H_2O$ decompose under electron beam irradiation and release Cl^- ions. The nanomotor generates its own local ion concentration gradient due to different chemical reactivities on different facets. An electric field pointing toward the particle is spontaneously formed. This local and self-generated electric field then moves the charged particle in a way as self-diffusiophoresis, which opens future opportunities in exploring the applications of chemically powered nanomachines.

This chapter is adopted from Jiawei Wan *et al* 's work entitled "Facets Asymmetry Induced Directional Movement of Cadmium Chloride Nanomotor" from reference 59, with permission to reproduce it in this dissertation from the co-authors. In this work, the FEM simulation was performed by Dr. Jiayun Liang and Prof. Zakaria Y. Al Balushi.

5.1 Introduction

Nanomotors have attracted great attention because of their diverse applications ranging from drug delivery to chemical sensing, environmental remediation, and self-assembly[234–239]. Since the introduction of nanomotors using catalytic bimetallic nanorods[240], numerous nanomotors have been developed with various designs and driving mechanisms[241–243]. Among different strategies, chemical reactions are widely used to create the motion of nanomotors via bubble propulsion[244–247], self-diffusiophoresis[237,248–250] or self-electrophoresis[240,251]. The chemical reaction can be a spontaneous process[246,247], or it can be triggered by an external stimulus, such as light or electrical field[252–255]. For example, effort has been made on using light to control the speed and direction of a nanomotor's movement by changing the light intensity, polarization or wavelength[256,257]. In addition, rates of the chemical reactions may vary on different crystal facets[258]. Since high-index facets consist of a high density of low-coordinated atoms and dangling bonds, they offer more active sites for chemical reactions[259,260]. Recently, the enhanced performance of nanomotors has been achieved by ensuring high crystallinity and distinct activity of the exposed crystal facets[261]. However, it is hard to correlate the morphology changes of a nanomotor with the variations in moving direction and speed due to the lack of direct observation with high spatial resolution. Further understanding and controlling of the propulsion mechanisms of nanomotors utilizing different crystal facets are needed. Furthermore, despite the advances in controlling the motion of nanomotors, many nanomotors display Brownian motion with ineffective movements. Dependable and precise control of the directional motion of nanomotors is still a challenge[241].

Here, we present directional movement of $CdCl_2 \cdot 4H_2O$ nanomotors with distinct facets powered by electron beam illumination induced chemical reactions. Using *in situ* liquid cell TEM, we can track their movement and morphological evolution with remarkable precision. In recent years, *in situ* liquid cell TEM has become a powerful tool for studying liquid phase reactions and the dynamic phenomena at solid-liquid interfaces[23,262–264]. It has also been demonstrated that the electron beam can be used as the source to trigger pseudo-photochemical reactions[265,266], in which the inelastic scattering of the electron beam initiates photocatalytic reactions similar to those induced by UV light[266–268]. In this study, the electron beam is the energy source for powering the nanomotor as well as for imaging with high spatial resolution. While it may not be practical to use an electron beam for most real-world applications, the chemical reactions for motion of nanomotors with asymmetric geometry in this work can be initiated by alternative triggers.

The $CdCl_2 \cdot 4H_2O$ nanoparticles, which have an orthorhombic structure with water in between the layers, are formed in an aqueous solution inside a liquid cell. When exposed to the electron beam, the $CdCl_2 \cdot 4H_2O$ nanomotors show directional movement in an aqueous solution. We explore the origin of the directional motion of nanoparticles by carefully examining the dynamic movement, the asymmetric configuration with different crystal facets, and the chemical reactions. Finite element simulation of the electric field and fluid velocity distribution around the nanomotor assists our understanding of ionic self-diffusiophoresis as a driving force for the nanomotor movement.

5.2 Experimental setup and characterization

5.2.1 *In situ* liquid cell TEM

TEM experiments were performed on a FEI ThemIS aberration-corrected TEM at the National Center for Electron Microscopy (NCEM) of the Molecular Foundry (MF), Lawrence Berkeley National Laboratory (LBNL). The microscope was operated at 300 keV with a Super-X EDS detector, allowing for rapid chemical identification.

5.2.2 Finite element simulation setting

To further substantiate our theory regarding the movement of nanomotor arising from ionic self-diffusiophoresis, which stems from the reactivity differences between the different crystal facets, we employed the FEM based on COMSOL Multiphysics platform (version 6.1) to simulate the distribution of electric potential (V) and the fluid field ($\vec{v}$) surrounding the moving $CdCl_2 \cdot 4H_2O$ nanocrystal within the aqueous solution. To guarantee the accuracy of the simulation result, an extremely fine 2D axisymmetric mesh, which contained 31477 triangle elements and 63438 degrees of freedoms, was built to avoid any possible impacts introduced by the asymmetric mesh.

In our experiment, most of the charge, especially at the surface of $CdCl_2$ nanomotor, come from the radiolysis related redox reaction of $CdCl_2 \cdot 4H_2O$:

$$2CdCl_2 \cdot 4H_2O \leftrightarrow 2Cd + 4H^+ + 4Cl^- + 2H_2O_2$$

Given the fact that H^+ ($D_{H+} = 9.31 \times 10^{-9}$ m^2 s^{-1}) has a higher diffusivity constant than that of Cl^-($D_{Cl-} = 2.03 \times 10^{-9}$ m^2 s^{-1}), the surface of nanomotor is negatively charged because of the surface adsorption of Cl^- ion. The surface charge density ρ_s hereby depends on the ion flux, J, generated on $CdCl_2$ surface. To quantify the ion flux, based on the model developed by Zhou et al[237], we have:

$$J = kn_{CdCl_2}$$

where k is the rate constant of the radiolysis related redox reaction of $CdCl_2 \cdot 4H_2O$, and n_{CdCl_2} is the surface concentration of $CdCl_2$. Assuming that all the surface species participate in the reaction, n_{CdCl_2} can be calculated with the following equation:

$$n_{CdCl_2} = \frac{hA\rho}{M_{CdCl_2}}$$

where h and A are thickness and surface area of $CdCl_2$, respectively. ρ and M_{CdCl_2} are density and molar mass of $CdCl_2$. Therefore, the surface charge density ratio ($\frac{\rho_{s,h}}{\rho_{s,l}}$) between high index and low index facet is:

$$\frac{\rho_{s,h}}{\rho_{s,l}} = \frac{k_h A_h}{k_l A_l} = r_c \frac{A_h}{A_l}$$

where subscript "h" and "l" represent high index facet and low index facet, respectively. Here the thickness (dimension parallel to the electron beam direction) of different facets is approximated to be the same and the surface area is estimated based on the length of crystal facet in TEM images.

Additionally, the distribution of fluid field surrounding the moving $CdCl_2 \cdot 4H_2O$ nanocrystal follows the governing equations:

$$\nabla \cdot \vec{v} = 0$$

$$\nabla p = \eta \nabla^2 \vec{v}$$

Here, p denotes the pressure and η represents the dynamic viscosity of water, respectively. At the $CdCl_2$-water interface, the electroosmotic flow ($\overrightarrow{v_{eo}}$) is given by:

$$|\overrightarrow{v_{eo}}| = \frac{\zeta \varepsilon}{\eta} E'$$

where ζ corresponds to the zeta potential of either the high index or low index crystal facet, and E' represents the tangential component of the electric field. Considering the axial symmetry of the simulation model in both r-axis and phi-axis, the velocity of the nanomotor is determined as the average of the z-direction velocity component of electroosmotic flow surrounding the nanomotor.

5.3 Directional motion of a $CdCl_2 \cdot 4H_2O$ nanomotor

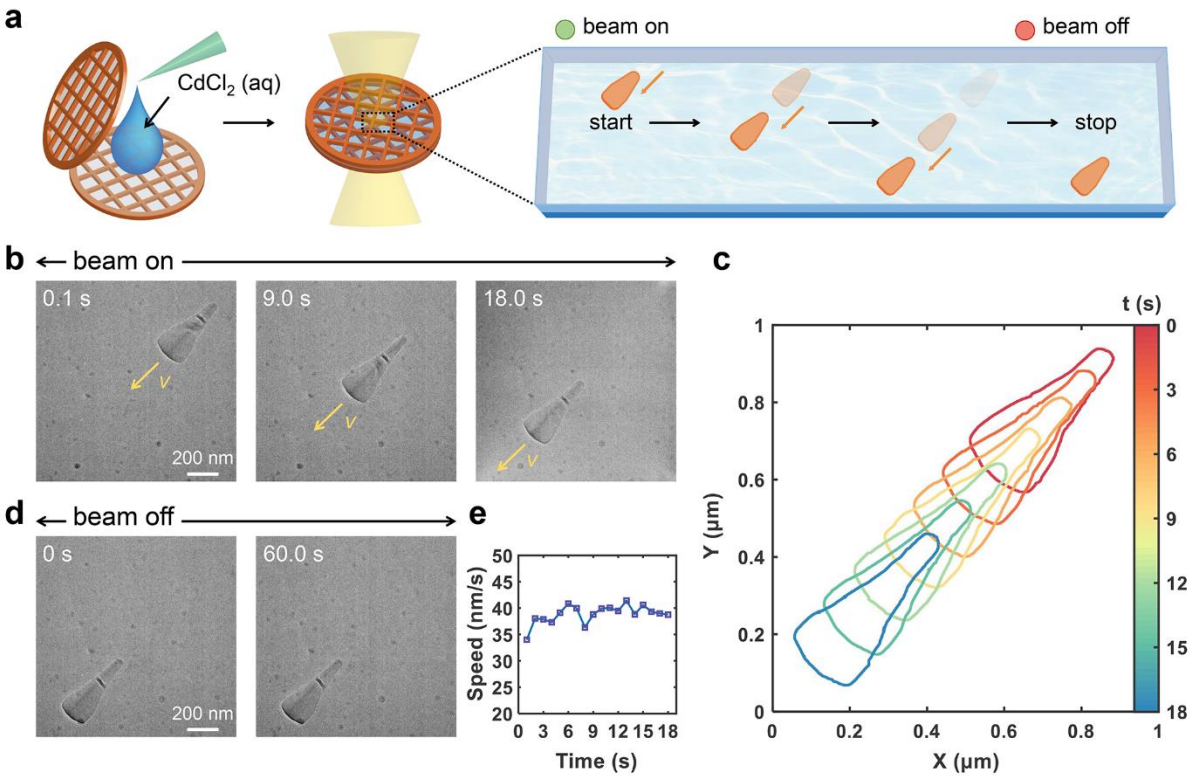

Figure 5.1: Directional motion of $CdCl_2 \cdot 4H_2O$ nanomotor in an aqueous solution under electron beam illumination. (**a**) Schematic representation of liquid cell and typical motion of a $CdCl_2 \cdot 4H_2O$ nanomotor. (**b**) Sequential TEM images from a movie showing directional motion of the $CdCl_2 \cdot 4H_2O$ nanomotor under electron beam illumination. (**c**) Representative trajectory of the $CdCl_2 \cdot 4H_2O$ nanomotor in a period of 18.0s. (**d**) Sequential TEM images showing the $CdCl_2 \cdot 4H_2O$

nanomotor with no movement without electron beam illumination. (**e**) The evolution of speed with time for the corresponding nanomotor shown in (b).

The schematic in **Fig. 5.1a** shows the preparation of a carbon film liquid cell and *in situ* liquid cell TEM imaging of the nanomotor's dynamic movement. The carbon film liquid cell is made with two carbon film-coated TEM grids encapsulating a liquid thin film. A droplet (1 μL) of the $CdCl_2$ dilute aqueous solution (0.1 mol L^{-1}) is dropped onto one carbon film grid and then covered by the second carbon film grid. Subsequent evaporation of some of the water results in sealing of the two films by van der Waals forces to form pockets of solution trapped inside. The thickness of liquid film in the pocket ranges from tens to hundreds of nanometers, measured using EELS[77,264]. During *in situ* TEM observation, $CdCl_2 \cdot 4H_2O$ nanoparticles of different shape nucleate and grow in the liquid cell resulting from evaporation of the aqueous solution. (more detailed crystal structure identification will be discussed in a later section). EDS elemental mapping is performed showing uniform distribution of Cd, Cl, and O in the nanoparticle (**Fig. 5.2**). The $CdCl_2 \cdot 4H_2O$ nanocrystal in **Fig. 5.1** is about 200 nm in diameter and 500 nm long with an asymmetric shape; one end is flat and the other end is a pointed-tip. Under electron beam irradiation (180 $e^{-}Å^{-2}s^{-1}$), the nanocrystals move in a straight line towards the direction of the flat end. As illustrated in **Fig. 5.1b**, the $CdCl_2 \cdot 4H_2O$ nanoparticle presents continuous self-propelled movement. We track the trajectories of the nanomotor movement and find the motion to be very linear as shown in **Fig. 5.1c**. The contour and particle size evolutions (**Fig. 5.1c** and **Fig. 5.3**) reveal minor changes in its morphology. The nanomotor moves at a relatively constant speed in the solution of about 40 nm s^{-1} (**Fig. 5.1e**).

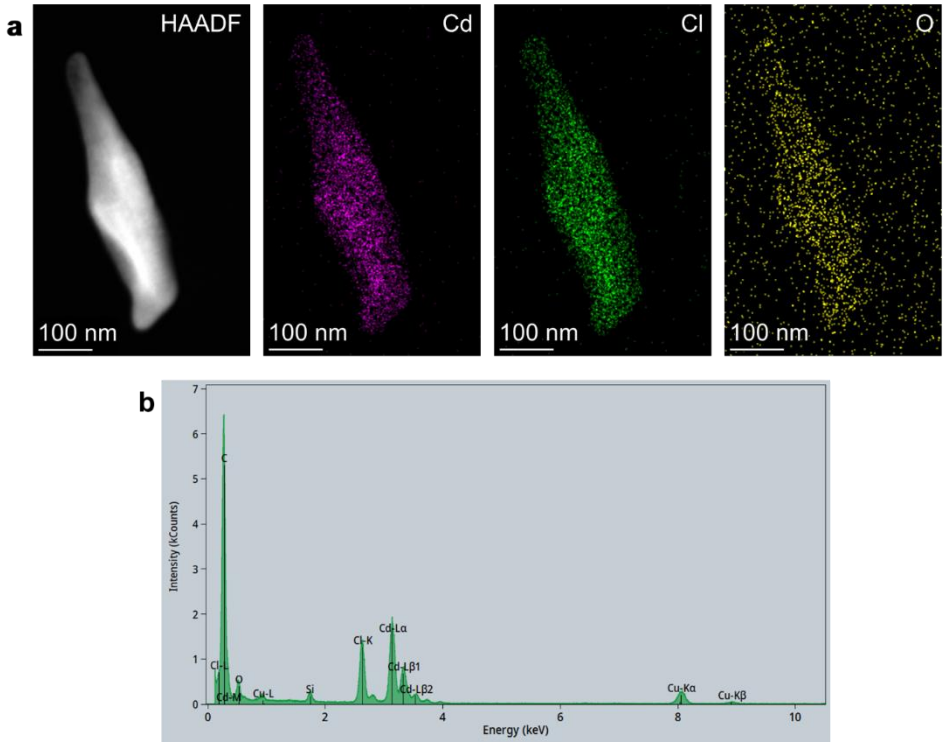

Figure 5.2: EDS mapping and spectrum of a $CdCl_2$ nanoparticle. (**a**) HAADF image, Cd map, Cl map, and O map. (**b**) EDS spectrum shows the presence of Cd, Cl, and O in the nanoparticle. The Cu peak comes from the Cu grid and the Si peak comes from the tip of the TEM holder.

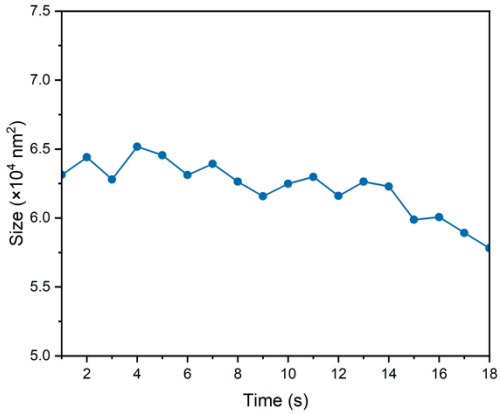

Figure 5.3: Evolution of projected area of nanomotor in Figure 5.1.

When the electron beam is shut off, the nanoparticle becomes stationary in the aqueous solution. **Fig. 5.1d** shows two captured photos inside the liquid cell, the first one is acquired just before the beam is shut off and the other is acquired after the beam has been off for 60 seconds. The nanomotor isn't propelled forward during the time when there's no electron beam irradiation. When the beam is turned on again, the nanomotor resumes the state of motion. Therefore, we can conclude that the electron beam serves as the external source propelling the nanomotor (**Fig. 5.1a**). Similar to the light-powered nanomotors, the electron beam can be used as a strategy for powering nanomotors where a $CdCl_2 \cdot 4H_2O$ nanomotor can be manipulated through the "on/off" switching of the electron beam illumination. Controllable launch and stop of synthetic nanomotors are of special importance for practical applications.

5.4 Deformation of a $CdCl_2 \cdot 4H_2O$ nanomotor

We investigate the nanomotor's dynamics under a higher electron dose rate (450 $e^{-}Å^{-2}s^{-1}$) on the $CdCl_2 \cdot 4H_2O$ nanomotors. The $CdCl_2 \cdot 4H_2O$ nanomotor under higher electron dose rate shows obvious surface deformation and concurrent speed changes during the course of movement as shown in **Fig. 5.4**; this behavior is different from the nanomotor in **Fig. 5.1** under lower electron dose rate exhibiting uniform velocity without distinguishable shape change. Video snapshots of the motion are shown in **Fig. 5.4a**, where the yellow arrows represent the moving direction of the nanomotor. The trajectory and outline of the nanomotor from the aligned movie (**Fig. 5.4b**) provides a distinct view of the motion. Similarly, the nanomotor shows excellent performance of directional motion pointing to the flat end. It also shows an obvious shape change of the nanoparticle that is not present in **Fig. 5.1a**. Comparing the shape of the nanomotor at 0 second with that at 30 seconds, it is found that the tip is elongated and the corner of flat end becomes sharper.

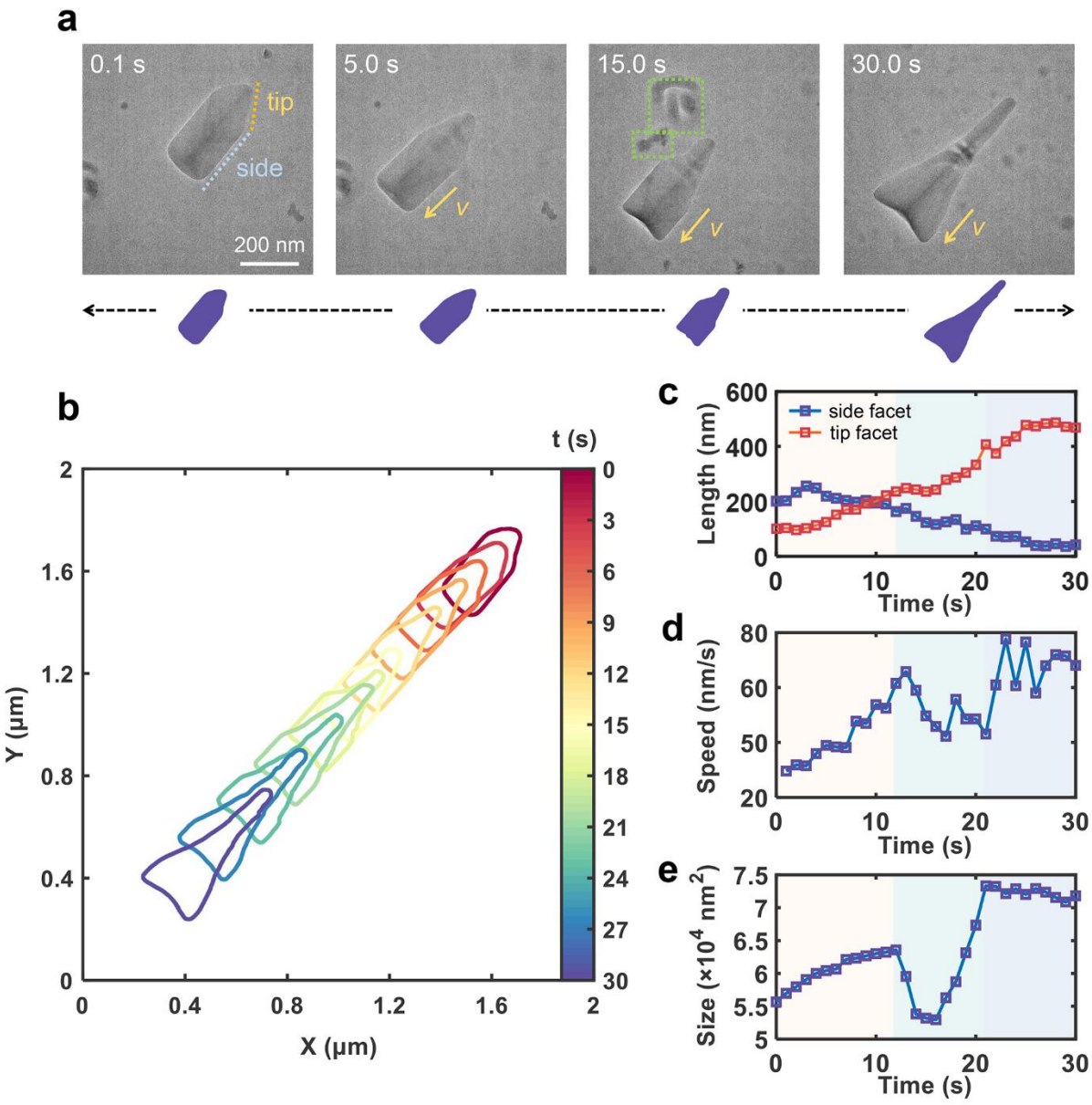

Figure 5.4: A $CdCl_2 \cdot 4H_2O$ nanomotor shows deformation during movement. (**a**) Sequential TEM images showing the deformation of a $CdCl_2 \cdot 4H_2O$ nanomotor during its directional movement. (**b**) Representative trajectory of the $CdCl_2 \cdot 4H_2O$ nanomotor in a period of 30.0s. (**c**)-(**e**) Evolution of the crystal facets, speed of movement, and projected area of the nanomotor shown in (b).

The characteristics of motion, including the evolution of facets, speed, and particle size of the nanomotor are analyzed. **Fig. 5.4c** shows the evolution of the facets' lengths on one side of the nanocrystal. We find that the tip facet (marked with yellow color in **Fig. 5.4a**) is elongated while the side facet (marked with blue color in **Fig. 5.4a**) is shortened during the motion of the nanomotor. As for the size and speed of the nanomotor, it shows three phases: first, from 0 to 11 seconds, the size and speed increase. Then, from 12 to 21 seconds, the size and speed suddenly decrease. Finally, from 22 to 30 seconds, the size and speed increase to a steady state (**Fig. 5.4d** and **e**). Overall, we can see that the speed has a relationship with the size of crystal facets. When the tip facet becomes longer, the speed of the nanomotor increases.

It is an interesting observation that during the second phase shown in **Fig. 5.4a**, the abnormal size and speed evolution of the nanomotor is instigated by other nanoparticles in the liquid (dotted box marked with green color). When moving close to these obstacles, the nanomotor and obstacles show repulsive interaction between each other likely due to the surface changes. The nanomotor can change its shape by shrinking on the surface in order to avoid the obstacles. The unique function of spontaneously avoiding obstacles in the fluids without changing the direction of the movement is fascinating. This observation demonstrates that nanomotors can deal with obstacles in complex tasks, which is of significant importance in the field of micro- and nanomotors.

5.5 Structural characterization of a $CdCl_2 \cdot 4H_2O$ nanomotor

HRTEM images are acquired to elucidate the atomic structure of the nanoparticles. **Fig. 5.5a** shows the TEM image of a $CdCl_2 \cdot 4H_2O$ nanocrystal inside the liquid cell and the enlarged yellow box shows the HRTEM image from a small area of the nanoparticles. A FFT pattern of the TEM image shows a set of spots corresponding to the orthorhombic crystal structure of cadmium chloride tetrahydrate ($CdCl_2 \cdot 4H_2O$) {002} (~0.75 nm) and {240} lattice planes (~0.24 nm) (**Fig. 5.5b**) and the crystal structure information of a standardized unit cell is shown in **Table 5.1**. Higher order spots are also shown in the FFT pattern which also match the structure of $CdCl_2 \cdot 4H_2O$[269]. The crystal structure of $CdCl_2 \cdot 4H_2O$ is shown in **Fig.5.5c**. It is reasonable for the material to be hydrated with water molecules between $CdCl_2$ layers that precipitate from aqueous solution without drying.

Table 5.1: Crystal structure information of $CdCl_2 \cdot 4H_2O$.

Space group	Crystal system	a (Å)	b (Å)	c (Å)	α (°C)	β (°C)	γ (°C)
$P2_12_12_1$	Orthorhombic	7.281	12.889	15.010	90	90	90

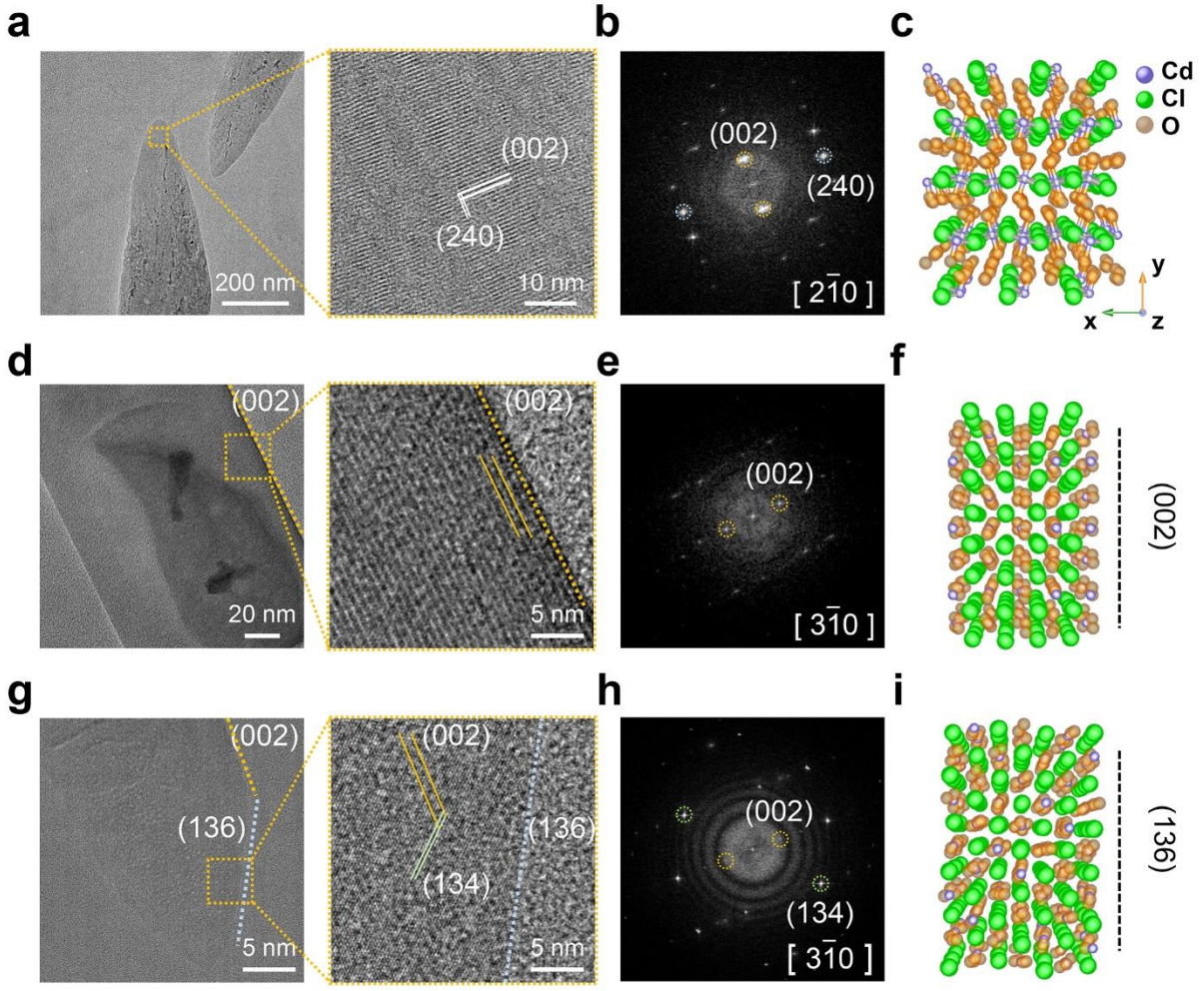

Figure 5.5: TEM characterization of the $CdCl_2 \cdot 4H_2O$ nanocrystals showing different crystal facets. (**a**) TEM image of $CdCl_2 \cdot 4H_2O$ nanocrystal. (**b**) FFT pattern corresponding to HRTEM image in (a) showing orthorhombic crystal structure ($P\,2_12_12_1$). (**c**) Crystal structure model of $CdCl_2 \cdot 4H_2O$. (**d**) TEM image of side portion of $CdCl_2 \cdot 4H_2O$ nanocrystal. (**e**) FFT pattern corresponding to HRTEM image in (d). (**f**) Crystal structure showing (002) facets of $CdCl_2 \cdot 4H_2O$. (**g**) TEM image of tip portion of $CdCl_2 \cdot 4H_2O$ nanocrystal. (**h**) FFT pattern corresponding to HRTEM image in (g). (**i**) Crystal structure showing (136) facets of $CdCl_2 \cdot 4H_2O$.

Since the material is sensitive to the high energy electron beam and its structure is easily damaged, we are unable to acquire a HRTEM image of the $CdCl_2 \cdot 4H_2O$ nanomotor during movement with the high dose-rate. However, we find a similar shape nanoparticle with a pointed-tip and a flat side, and acquire its HRTEM image with a short time of exposure. TEM images show both the side part and pointed-tip part of one $CdCl_2 \cdot 4H_2O$ nanoparticle in **Fig. 5.5d** and **g**. Additional HRTEM images from other areas on the nanoparticle are shown in **Fig. 5.6** with single crystal structure. From the FFT pattern (**Fig. 5.5e** and **h**) of each image, we can get the information about the facets: {002} facets on the side and {136} facets at the tip of the nanoparticle are exposed

to the solution. **Fig. 5.5f** and **i** show the crystal models for {002} and {136} facet. Higher index facets {136} at the tip have higher density of low-coordinated atoms and dangling bonds. After long time electron beam exposure, the nanoparticle is partially damaged. The TEM images show the left nanocrystal maintains $CdCl_2 \cdot 4H_2O$ structure (**Fig. 5.7**).

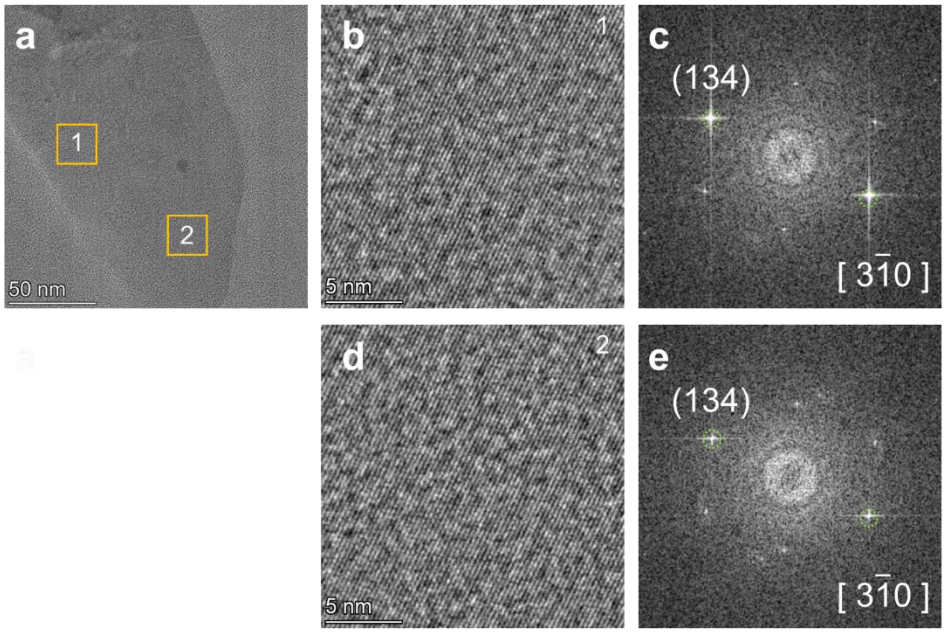

Figure 5.6: TEM characterization of a $CdCl_2 \cdot 4H_2O$ nanocrystal. (**a**) TEM image of a $CdCl_2 \cdot 4H_2O$ nanocrystal. (**b**)-(**c**) HRTEM image and corresponding FFT pattern of area 1 in (a). (**d**)-(**e**) HRTEM image and corresponding FFT pattern of area 2 in (a).

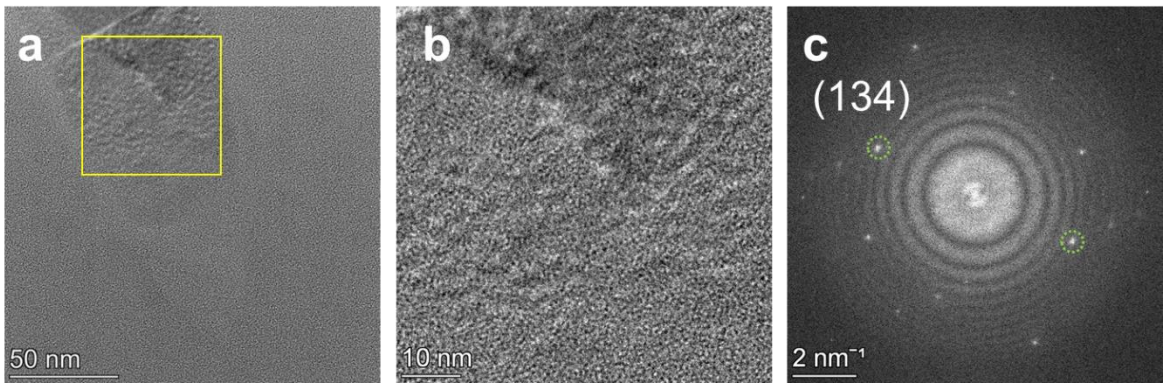

Figure 5.7: TEM characterization of the $CdCl_2 \cdot 4H_2O$ nanocrystals after high energy electron beam exposure. (**a**) TEM image of damaged $CdCl_2 \cdot 4H_2O$ nanocrystal. (**b**) HRTEM image of enlarged area from (a). (**c**) FFT pattern corresponding to HRTEM image in (b).

5.6 Mechanism study on nanomotor directional movement

Based on the observations that the nanomotor moves exclusively when electron beam is on, we conclude that the electron beam serves as the external energy source propelling the nanomotor. It's well known that the electron beam can influence a sample in different ways (e.g., heating, charging, photochemical reactions, etc.)[270,271]. According to the previous studies, the electron beam can act as a reducing agent that reduces $CdCl_2$ to metallic Cd in a liquid cell[272]. Also, the mass loss of the nanomotor is detected from particle size decrease (**Fig. 5.3**), indicating the existence of such decomposition reactions. We hypothesize that electron beam can induce a radiolysis-related redox reaction of $CdCl_2 \cdot 4H_2O$ similar to the photodecomposition of AgCl nanomotors[265]:

$$2CdCl_2 \cdot 4H_2O \leftrightarrow 2Cd + 4H^+ + 4Cl^- + 2H_2O_2$$

Given the fact that the produced H^+ ($D_{H+} = 9.31\times10^{-9}m^2s^{-1}$) diffuses much faster than Cl^- ($D_{Cl-} = 2.03\times10^{-9}m^2s^{-1}$) in the forward reaction, a Cl^- rich inside/H^+ rich outside ionic gradient could form[237,250,273]. Then, Cl^- ions$^-$ can be adsorbed on the surface of $CdCl_2$ nanocrystals due to the strong Cd^{2+}-Cl^- affinity in the first Helmholtz layer, and the surface will be further screened by outer layer ions.

The motion of self-propelled nanomotors is usually driven by asymmetric surface chemical reactions. Here, we propose that the motion of the $CdCl_2 \cdot 4H_2O$ nanomotor is caused by the differences in chemical reactivity on the different crystal facets of a single nanocrystal under the mechanism of ionic self-diffusiophoresis, as shown in **Fig. 5.8a**. According to the HRTEM results showing in **Fig. 5.5**, the tip facets are high index facets compared with other parts of the nanocrystal. The chemical reactions prefer taking place on these facets; it has been well established that high index crystal facets are more reactive chemically than low index crystal facets. Therefore, the tip is more reactive in the liquid cell under electron beam irradiation, which generates a higher concentration of Cl^- near the tip compared with the flat end. The asymmetric ionic concentration gradients around the nanomotor, resulting from different crystal facet reactivity, induce local electric field pointing toward the tip, which produces movement originating from ionic self-diffusiophoresis.

During the movement, chemical reaction induced mass loss leads to slight shrinking of particle size (**Fig. 5.3**). However, non-uniform surface charges and surface tension can contribute to an interparticle atomic reconstruction process resulting in shape changes as well, which is observed from the reshaping of AgCl nanocrystals in liquid phase TEM[265]. Under high electron beam intensity (**Fig. 5.4**), the electrostatic force surpasses surface tension, leading to reconstruction (e.g., sharpened corner, elongated tail) and an increased projected area of the $CdCl_2 \cdot 4H_2O$ nanomotor. The particle becomes thinner during the reconstruction process. Compared with the results of the nanomotor in **Fig. 5.1** under a low electron dose rate, the high electron dose rate induces a highly elongated shape, which has a higher reactive surface area. In ionic self-diffusiophoresis process, the velocity of particles is in proportional to the gradient of the ion concentration. Larger high index crystal facets lead to more reaction products, which generates a larger gradient. Therefore, when the tip of the nanomotor is elongated during the high dose-rate motion, the speed also increases.

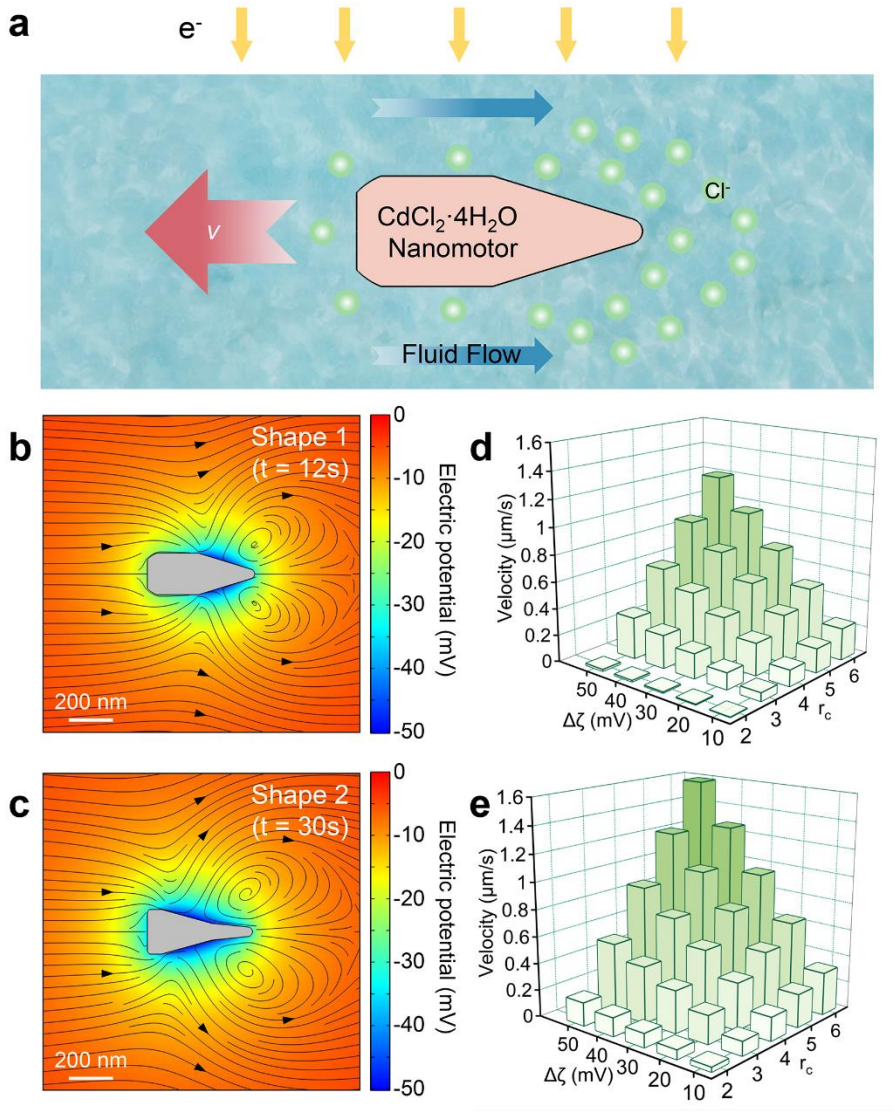

Figure 5.8: Mechanisms and finite element simulation of $CdCl_2 \cdot 4H_2O$ nanomotor system. (**a**) Schematic of ionic self-diffusiophoresis mechanism for the directional movement of $CdCl_2 \cdot 4H_2O$ nanomotor. (**b-c**) The distribution of electric potential (*color code*) and the fluid field (*black arrows*) surrounding $CdCl_2 \cdot 4H_2O$ nanocrystal during the deformation process of the nanomotor in (b) shape 1, and shape 2. (**d-e**) Corresponding average speed of the moving nanomotor in: (d) shape 1 and (e) shape 2 with various combinations of r_c and $\Delta\zeta$.

We employed the FEM to simulate the distribution of electric potential (V) and fluid field ($\vec{v}$) surrounding a $CdCl_2 \cdot 4H_2O$ nanocrystal within an aqueous solution (**Fig. 5.8a**) to understand the nanomotor movement arising from ionic self-diffusiophoresis caused by asymmetric crystal facets. Here, the electric potential distribution was simulated with the following equations:

$$\vec{E} = -\nabla V$$

$$\nabla \cdot (\varepsilon \vec{E}) = \rho_v$$

where $\vec{E}$ is electric field, ε is medium electrical permittivity, and ρ_v is space charge density. At the $CdCl_2$-water interface, the boundary condition for electric potential distribution was defined as:

$$\vec{n} \cdot (\varepsilon_1 \overrightarrow{E_1} - \varepsilon_2 \overrightarrow{E_2}) = \rho_s$$

For a crystal facet, surface charge density (ρ_s) is proportional to the product of its area (A) and reaction constant (k). And ratio of the surface charge densities of high index to low index one ($\frac{\rho_{s,h}}{\rho_{s,l}}$) can be determined using the following equation[237] (more details in Supporting Information):

$$\frac{\rho_{s,h}}{\rho_{s,l}} = \frac{k_h A_h}{k_l A_l} = r_c \frac{A_h}{A_l}$$

where subscript "h" and "l" represent high and low index facets, respectively. And r_c is the ratio of reaction constant of high index to low index one. At $CdCl_2$-water interface, the electroosmotic flow ($\overrightarrow{v_{eo}}$) is given by:

$$|\overrightarrow{v_{eo}}| = \frac{\zeta \varepsilon}{\eta} E'$$

where ζ corresponds the zeta potential of either the high index or low index crystal facet, and E' represents the tangential component of the electric field.

Electric field intensity and zeta potential at the $CdCl_2$-water interface are two important factors that dominate the direction and speed of the electroosmotic flow. The high index facet-water interface possesses a higher surface charge density with a greater concentration of Cl^- ions, accompanied by a more positive zeta potential value. **Fig. 5.8b** and **c** show the distribution of electric potential (*color code*) and the resulted fluid field (*black arrows*) surrounding $CdCl_2 \cdot 4H_2O$ nanocrystal with two different shapes. The shape 1 and 2 are the shape of $CdCl_2 \cdot 4H_2O$ nanocrystal at 12 s and 30 s in **Fig. 5.4c**, respectively. In the case of the negative surface charges, the electric potential gradient from the flat end to the tip induces an electroosmotic fluid flow in the same direction, independent of the shape of nanomotor. In the simulation model, the nanomotor is set as the reference frame, while in aforementioned experimental results, liquid is set as the reference frame. Building upon this premise, our simulation results well align with the experimental evidence in **Fig. 5.4** with ionic self-diffusiophoresis mechanism.

Additionally, electric field intensity is contingent upon the surface charge density, and therefore the reaction constant of the corresponding crystal facet. However, due to the lack of research on reaction constants for different crystal facets in $CdCl_2 \cdot 4H_2O$, quantifying r_c and the zeta potential differences $\Delta\zeta$, which is defined as the difference between ζ_h and ζ_l, between facets proves challenging. Instead, a series of parameter-sweeping simulations are performed by sweeping r_c (ranging from 2 to 6) and $\Delta\zeta$ (ranging from 10 to 50mV), aiming to qualitatively analyze the impact of r_c and $\Delta\zeta$ on the speed of the electroosmotic flow. The resulting speed of the moving nanomotor in two different shapes with various combinations of r_c and $\Delta\zeta$ is presented in **Fig. 5.8d** and **e**, respectively. The results suggest that a larger difference in reaction constant (i.e., greater r_c) and/or zeta potential between the low index and the high index facets (i.e., higher $\Delta\zeta$) will lead to the faster movement of nanomotor. Furthermore, the shape of the nanomotor, specifically the ratio of exposed high index to the low index facets, modulates the speed of moving

nanomotor as well. With fixed r_c and $\Delta\zeta$, compared to shape 1 (**Fig. 5.8d** and **Table 5.2**), the nanomotor with shape 2 (**Fig. 5.8e** and **Table 5.3**) moves faster. This difference arises from the elongated high index facets, which results in the release of more ions, thereby enhancing the electric field intensity around the surface of nanomotor. This simulation elucidates three tuning knobs (reaction constant ratio, zeta potential difference, and the shape of the nanomotors) for controlling the directional movement of nanomotors, and therefore enables the design of nanomotors with diverse structures and compositions to cater to a wide range of applications.

Table 5.2: Average velocity of $CdCl_2{\cdot}4H_2O$ nanomotor with shape 1 under various combinations of r_c and $\Delta\zeta$.

Average velocity of nanomotor (μm/s)		Zeta potential difference $\Delta\zeta$ (mV)				
		10	20	30	40	50
r_c	2	0.003	0.062	0.121	0.180	0.239
	3	0.006	0.124	0.242	0.360	0.478
	4	0.009	0.186	0.363	0.540	0.718
	5	0.011	0.248	0.484	0.721	0.957
	6	0.014	0.310	0.605	0.901	1.196

Table 5.3: Average velocity of $CdCl_2{\cdot}4H_2O$ nanomotor with shape 2 under various combinations of r_c and $\Delta\zeta$.

Average velocity of nanomotor (μm/s)		Zeta potential difference $\Delta\zeta$ (mV)				
		10	20	30	40	50
r_c	2	0.035	0.105	0.176	0.246	0.317
	3	0.069	0.211	0.352	0.493	0.634
	4	0.104	0.316	0.527	0.739	0.951
	5	0.139	0.421	0.703	0.985	1.268
	6	0.174	0.526	0.879	1.232	1.584

5.7 Conclusions

In conclusion, we have demonstrated $CdCl_2{\cdot}4H_2O$ nanomotors with outstanding directional movement in an aqueous solution driven by electron beam illumination using *in situ*

liquid phase TEM. The $CdCl_2 \cdot 4H_2O$ nanocrystals with different crystal facets can generate an asymmetric chemical concentration gradient due to differences in facet reactivity. The ionic self-diffusiophoresis drives the nanomotor movement. Using finite element simulation, we have been able to further understand this mechanism for fine-control of the directional movement of nanomotors through three tunning knobs (reaction constant, zeta potential, and the shape of the nanomotors). Our study represents advances in designing, characterizing, and controlling nanomotors with directional movement. It opens future opportunities in exploring the future applications of chemically powered nanomachines.

Chapter 6

Conclusions and outlooks

This chapter captures the principal findings of this dissertation and suggests potential avenues for advancing the research frontier of the body of work presented. The *in situ/operando* liquid cell TEM provides an advanced platform for real-time visualization of dynamic physical and chemical processes, which has created great opportunities for studying the mechanisms behind a wide range of dynamic processes of functional materials, such as electrocatalyst, and rechargeable batteries. To further probe the dynamic processes among different cutting-edge fields, challenges remain to be solved, and further improvements are always necessary.

6.1 Conclusions

This dissertation focuses on understanding the structural transformation mechanisms of electrocatalysts and other functional materials in aqueous solutions via *in situ/operando* TEM techniques. In Chapter 2, I introduce the two-electrode and three-electrode polymer membrane-based electrochemical liquid cells, which enable the breakthroughs in study of dynamic phenomena of electrocatalysts during electrocatalytic reactions at the atomic level and with the capability of elemental composition analysis.

In Chapter 3, I combined in-situ EC-TEM with *operando* XAS to unveil the formation pathways of OD-Cu active sites from CuO bicrystal nanowire precatalysts. These findings suggest a means to optimize active OD-Cu nanostructures through nanocracking by tailoring grain boundaries in CuO precatalysts. Our advanced *operando* approach opens new opportunities for mechanistic insights onto the improved control of catalyst structure and performance. This work also demonstrates an innovative solution towards spatiotemporally resolving the complex and dynamic nature of precatalysts in electrochemical systems, and emphasizes the crucial relevance of applying complementary operando methods such as electron microscopy and X-ray spectroscopy for understanding structure-performance correlations.

In Chapter 4, I have demonstrated the temperature-dependent structure diversity of Cu nanoparticles from electrodeposition. The particle size, morphology, crystallinity of Cu nanoparticles obtained from sub-zero temperature are distinctly different from those obtained at the room temperature. This study deepens our understanding of nucleation of nanostructures and sheds light on the governing factors in electrodeposition of metal nanoparticles and nanoscale dynamic processes.

In Chapter 5, I have described the study of $CdCl_2 \cdot 4H_2O$ nanomotors with outstanding directional movement in an aqueous solution driven by electron beam illumination using *in situ* liquid cell TEM. The $CdCl_2 \cdot 4H_2O$ nanocrystals with different crystal facets can generate an asymmetric chemical concentration gradient due to differences in facet reactivity. The ionic self-diffusiophoresis drives the nanomotor movement. Our study represents advances in designing, characterizing, and controlling nanomotors with directional movement. It opens future opportunities in exploring the future applications of chemically powered nanomachines.

6.2 Outlooks

The future of *in situ*/*operando* liquid cell TEM holds exciting potential for advancing our understanding of dynamic processes in physics, chemistry, biology, and materials science. As researchers continue to push the boundaries of spatial and temporal resolution, innovations in the liquid cell design will enable more precise real-time imaging of nanoscale phenomena. The integration of multimodal functionalities, such as simultaneous electrical biasing, heating, and liquid flow control, will allow for more sophisticated experimental setups, providing deeper insights into complex systems. Additionally, advancements in data acquisition and machine learning algorithms will enhance the ability to process large datasets, facilitating more accurate analysis of temporal changes in materials at the atomic level. As these technologies evolve, *in situ*/*operando* liquid cell TEM will become an even more powerful tool for probing dynamic processes, accelerating breakthroughs in energy storage, catalysis, and other cutting-edge fields.

6.2.1 Improvement of spatial and temporal resolution

First, there is still room for optimizing the balance among spatial resolution, liquid controllability, and experimental repeatability. Although 2D membrane-based liquid cells can achieve atomic resolution imaging, the randomly formed thin liquid pockets limit control over the amount and properties of the liquid. In contrast, SiN_x membrane-based liquid cells provide well-defined liquid layer thickness with flow capabilities, but the thicker liquid layer hinders high-resolution imaging. Additionally, their complex preparation process can impede broader application. Addressing these challenges may require an optimized liquid cell design and improved membrane composition.

Secondly, technical advancements, such as the development of sensitive and fast detectors and the integration of pump-probe techniques, have elevated *in situ* TEM to enable time-resolved studies across a broad range of timescales while preserving atomic-scale spatial resolution. Achieving this requires a sophisticated combination of laser and electron gun technologies, energy filters, apertures, detectors, and advanced data acquisition and processing schemes. More systematic experimental and theoretical investigations into the effects of these technologies on beam properties are essential to harness their full potential.

6.2.2 Integration of multimodal characterizations

The integration of multimodal characterization capabilities into *in situ/operando* liquid cell TEM has revolutionized the study of dynamic processes allowing for simultaneous control and monitoring of various stimuli. By combining capabilities such as electrical biasing, heating, chemical flow, within the liquid cell, researchers can now replicate real-world conditions more accurately while observing structural and chemical transformations in real-time at the nanoscale. Electrical biasing facilitates the study of electrochemical reactions, making it invaluable for investigating processes like battery cycling or electrocatalysis, while heating allows for the observation of thermally driven phenomena such as phase transitions and crystallization. Flow control introduces reactants in a continuous manner, making it possible to study reactions in operando conditions. This convergence of multiple stimuli within a single experiment offers unprecedented insights into complex material behaviors and has opened new avenues for applications ranging from energy storage to nanomedicine. With continued advancements, multimodal *in situ*/*operando* liquid cell TEM will play a key role in decoding the intricate interplay between structure and function in dynamic systems.

Advancements in liquid cell fabrication also open up vast opportunities for integrating advanced electron microscopy techniques, such as EDS, EELS, 4D-TEM, electron tomography, and cryo-EM. Combining (S)TEM imaging with these complementary techniques would offer more comprehensive data for solving scientific problems.

6.2.3 Innovation from *in situ* to *operando* liquid cell TEM

The transition from *in situ* to *operando* liquid cell TEM marks a significant innovation in the ability to study dynamic processes in real-time under realistic conditions. While *in situ* TEM

allows for the visualization of processes in controlled environments, *operando* liquid cell TEM takes this a step further by enabling simultaneous imaging and functional measurements of materials property and reaction products during reactions. This advancement is particularly transformative for multiple fields of research, such as electrocatalysis, and batteries, where unveiling the materials behavior under working conditions and correlating the structure and function are essential for uncovering true mechanisms. By enabling the monitoring of chemical, structural, as well as functional evolution of materials in the liquid cell under electrical biasing, thermal heating, or other stimuli, *operando* TEM enables direct correlation between structural changes and material performance. This capability leap will provide more accurate insights into the dynamics of reaction mechanisms and degradation pathways, accelerating the development of more efficient catalysts, energy storage devices, and advanced materials. The shift from *in situ* to *operando* studies thus represents a critical step toward bridging the gap between laboratory observations and real-world applications, unlocking new frontiers in material science and nanotechnology.

References

1. Mirsaidov, U., Patterson, J. P. & ZhengGuest, H. Liquid phase transmission electron microscopy for imaging of nanoscale processes in solution. *MRS Bulletin* **45**, 704–712 (2020).
2. Gong, S. *et al.* Recent Progress on the Stability of Electrocatalysts under High Current Densities toward Industrial Water Splitting. *ACS Catal.* 14399–14435 (2024) doi:10.1021/acscatal.4c03700.
3. Yip, K. M., Fischer, N., Paknia, E., Chari, A. & Stark, H. Atomic-resolution protein structure determination by cryo-EM. *Nature* **587**, 157–161 (2020).
4. Alcorn, F. M., Jain, P. K. & van der Veen, R. M. Time-resolved transmission electron microscopy for nanoscale chemical dynamics. *Nat Rev Chem* **7**, 256–272 (2023).
5. Urban, K. W. *et al.* Progress in atomic-resolution aberration corrected conventional transmission electron microscopy (CTEM). *Progress in Materials Science* **133**, 101037 (2023).
6. Stadelmann, P., Leifer, K. & Verdon, C. EDS and EELS using a TEM-FEG microscope. *Ultramicroscopy* **58**, 35–41 (1995).
7. Electron energy-loss spectroscopy in the TEM - IOPscience. https://iopscience.iop.org/article/10.1088/0034-4885/72/1/016502/meta.
8. Tsang, C. S. *et al.* Polar and quasicrystal vortex observed in twisted-bilayer molybdenum disulfide. *Science* **386**, 198–205 (2024).
9. Kazmierczak, N. P. *et al.* Strain fields in twisted bilayer graphene. *Nat. Mater.* **20**, 956–963 (2021).
10. Craig, I. M. *et al.* Local atomic stacking and symmetry in twisted graphene trilayers. *Nat. Mater.* **23**, 323–330 (2024).
11. Wang, N. *et al.* Bulk high-temperature superconductivity in pressurized tetragonal La2PrNi2O7. *Nature* **634**, 579–584 (2024).
12. Liu, L. *et al.* Imaging defects and their evolution in a metal–organic framework at sub-unit-cell resolution. *Nat. Chem.* **11**, 622–628 (2019).
13. Zhang, Q. *et al.* Metal/MXene composites via in situ reduction. *Nat. Synth* 1–10 (2024) doi:10.1038/s44160-024-00660-z.
14. DeepMainmast: integrated protocol of protein structure modeling for cryo-EM with deep learning and structure prediction | Nature Methods. https://www.nature.com/articles/s41592-023-02099-0.
15. Jamali, K. *et al.* Automated model building and protein identification in cryo-EM maps. *Nature* **628**, 450–457 (2024).
16. Kim, J. *et al.* Dissolution enables dolomite crystal growth near ambient conditions. *Science* **382**, 915–920 (2023).
17. Wirth, R. Focused Ion Beam (FIB) combined with SEM and TEM: Advanced analytical tools for studies of chemical composition, microstructure and crystal structure in geomaterials on a nanometre scale. *Chemical Geology* **261**, 217–229 (2009).
18. Zhao, J.-W., Li, Y., Luan, D. & Lou, X. W. (David). Structural evolution and catalytic mechanisms of perovskite oxides in electrocatalysis. *Science Advances* **10**, eadq4696 (2024).
19. Wei, S. Z. *et al.* Combining theory and experiment in electrocatalysis: Insights into materials design. *Science* **355**, eaad4998 (2017).
20. Yuan, H. *et al.* An ultrastable lithium metal anode enabled by designed metal fluoride spansules. *Science Advances* **6**, eaaz3112 (2020).
21. Yuk, J. M. *et al.* High-Resolution EM of Colloidal Nanocrystal Growth Using Graphene Liquid Cells. *Science* **336**, 61–64 (2012).
22. Zhang, J. *et al.* Clean Transfer of Large Graphene Single Crystals for High-Intactness Suspended Membranes and Liquid Cells. *Advanced Materials* **29**, 1700639 (2017).
23. Zheng, H. *et al.* Observation of single colloidal platinum nanocrystal growth trajectories. *Science* **324**, 1309–1312 (2009).

24. A Closed Cell for Electron Microscopy. https://www.science.org/doi/10.1126/science.100.2595.273 doi:10.1126/science.100.2595.273.
25. Williamson, M. J., Tromp, R. M., Vereecken, P. M., Hull, R. & Ross, F. M. Dynamic microscopy of nanoscale cluster growth at the solid–liquid interface. *Nature Mater* **2**, 532–536 (2003).
26. Liao, H.-G. *et al.* Facet development during platinum nanocube growth. *Science* **345**, 916–919 (2014).
27. Zheng, H. *et al.* Observation of Single Colloidal Platinum Nanocrystal Growth Trajectories. *Science* **324**, 1309–1312 (2009).
28. Liao, H.-G., Cui, L., Whitelam, S. & Zheng, H. Real-Time Imaging of Pt3Fe Nanorod Growth in Solution. *Science* **336**, 1011–1014 (2012).
29. Li, D. *et al.* Direction-Specific Interactions Control Crystal Growth by Oriented Attachment. *Science* **336**, 1014–1018 (2012).
30. Xin, H. L. & Zheng, H. In Situ Observation of Oscillatory Growth of Bismuth Nanoparticles. *Nano Lett.* **12**, 1470–1474 (2012).
31. Xin, H. L. *et al.* Revealing the Atomic Restructuring of Pt–Co Nanoparticles. *Nano Lett.* **14**, 3203–3207 (2014).
32. Nielsen, M. H., Aloni, S. & De Yoreo, J. J. In situ TEM imaging of CaCO3 nucleation reveals coexistence of direct and indirect pathways. *Science* **345**, 1158–1162 (2014).
33. Chee, S. W., Tan, S. F., Baraissov, Z., Bosman, M. & Mirsaidov, U. Direct observation of the nanoscale Kirkendall effect during galvanic replacement reactions. *Nature communications* **8**, 1224 (2017).
34. Zhu, C. *et al.* In-situ liquid cell transmission electron microscopy investigation on oriented attachment of gold nanoparticles. *Nat Commun* **9**, 421 (2018).
35. Formation of two-dimensional transition metal oxide nanosheets with nanoparticles as intermediates | Nature Materials. https://www.nature.com/articles/s41563-019-0415-3.
36. Yang, F. *et al.* Spatially and Chemically Resolved Visualization of Fe Incorporation into NiO Octahedra during the Oxygen Evolution Reaction. *J. Am. Chem. Soc.* **145**, 21465–21474 (2023).
37. Hong, J. *et al.* Metastable hexagonal close-packed palladium hydride in liquid cell TEM. *Nature* **603**, 631–636 (2022).
38. Wan, J. *et al.* Operando probing of nanocracking in CuO-derived Cu during CO$_2$ electroreduction. Preprint at https://doi.org/10.48550/arXiv.2407.16910 (2024).
39. Zhu, G.-Z. *et al.* In Situ Liquid Cell TEM Study of Morphological Evolution and Degradation of Pt–Fe Nanocatalysts During Potential Cycling. *J. Phys. Chem. C* **118**, 22111–22119 (2014).
40. Park, J. *et al.* Direct Observation of Nanoparticle Superlattice Formation by Using Liquid Cell Transmission Electron Microscopy. *ACS Nano* **6**, 2078–2085 (2012).
41. Powers, A. S. *et al.* Tracking Nanoparticle Diffusion and Interaction during Self-Assembly in a Liquid Cell. *Nano Lett.* **17**, 15–20 (2017).
42. Wang, Y. *et al.* Dynamic deformability of individual PbSe nanocrystals during superlattice phase transitions. *Science Advances* **5**, eaaw5623 (2019).
43. Touve, M. A., Carlini, A. S. & Gianneschi, N. C. Self-assembling peptides imaged by correlated liquid cell transmission electron microscopy and MALDI-imaging mass spectrometry. *Nat Commun* **10**, 4837 (2019).
44. Ou, Z., Wang, Z., Luo, B., Luijten, E. & Chen, Q. Kinetic pathways of crystallization at the nanoscale. *Nat. Mater.* **19**, 450–455 (2020).
45. Zhou, S. *et al.* Chiral assemblies of pinwheel superlattices on substrates. *Nature* **612**, 259–265 (2022).
46. Luo, B. *et al.* Unravelling crystal growth of nanoparticles. *Nat. Nanotechnol.* **18**, 589–595 (2023).
47. Jiang, Y. *et al.* In situ Study of Oxidative Etching of Palladium Nanocrystals by Liquid Cell Electron Microscopy. *Nano Lett.* **14**, 3761–3765 (2014).
48. Chen, L. *et al.* Imaging the kinetics of anisotropic dissolution of bimetallic core–shell nanocubes using graphene liquid cells. *Nat Commun* **11**, 3041 (2020).
49. Shan, H. *et al.* Nanoscale kinetics of asymmetrical corrosion in core-shell nanoparticles. *Nat Commun* **9**, 1011 (2018).

50. Tan, S. F. *et al.* Intermediate Structures of Pt–Ni Nanoparticles during Selective Chemical and Electrochemical Etching. *J. Phys. Chem. Lett.* **10**, 6090–6096 (2019).
51. Hauwiller, M. R. *et al.* Tracking the Effects of Ligands on Oxidative Etching of Gold Nanorods in Graphene Liquid Cell Electron Microscopy. *ACS Nano* **14**, 10239–10250 (2020).
52. Shi, F. *et al.* Strain-Induced Corrosion Kinetics at Nanoscale Are Revealed in Liquid: Enabling Control of Corrosion Dynamics of Electrocatalysis. *Chem* **6**, 2257–2271 (2020).
53. Zheng, Q. *et al.* Observation of Surface Ligands-Controlled Etching of Palladium Nanocrystals. *Nano Lett.* **21**, 6640–6647 (2021).
54. Wang, W., Yan, H., Anand, U. & Mirsaidov, U. Visualizing the Conversion of Metal–Organic Framework Nanoparticles into Hollow Layered Double Hydroxide Nanocages. *J. Am. Chem. Soc.* **143**, 1854–1862 (2021).
55. Wang, W. *et al.* Solid–liquid–gas reaction accelerated by gas molecule tunnelling-like effect. *Nat. Mater.* **21**, 859–863 (2022).
56. Zheng, H., Claridge, S. A., Minor, A. M., Alivisatos, A. P. & Dahmen, U. Nanocrystal Diffusion in a Liquid Thin Film Observed by in Situ Transmission Electron Microscopy. *Nano Lett.* **9**, 2460–2465 (2009).
57. Mirsaidov, U. M., Zheng, H., Bhattacharya, D., Casana, Y. & Matsudaira, P. Direct observation of stick-slip movements of water nanodroplets induced by an electron beam. *Proceedings of the National Academy of Sciences* **109**, 7187–7190 (2012).
58. Wan, J., Zhang, Q., Asta, M. & Zheng, H. Tacking Directional Movement of Nanomotors with Liquid Cell Electron Microscopy. *Microscopy and Microanalysis* **28**, 1888–1890 (2022).
59. Wan, J. *et al.* Visualizing Facets Asymmetry Induced Directional Movement of Cadmium Chloride Nanomotor. *Nano Lett.* **23**, 10132–10139 (2023).
60. Lyu, Z. *et al.* Nanoscopic Imaging of Self-Propelled Ultrasmall Catalytic Nanomotors. *ACS Nano* **18**, 14231–14243 (2024).
61. Jonge, N. de, Peckys, D. B., Kremers, G. J. & Piston, D. W. Electron microscopy of whole cells in liquid with nanometer resolution. *Proceedings of the National Academy of Sciences* **106**, 2159–2164 (2009).
62. Kong, L. *et al.* Facile hermetic TEM grid preparation for molecular imaging of hydrated biological samples at room temperature. *Nat Commun* **14**, 5641 (2023).
63. Park, J. *et al.* Direct Observation of Wet Biological Samples by Graphene Liquid Cell Transmission Electron Microscopy. *Nano Lett.* **15**, 4737–4744 (2015).
64. Sun, M., Liao, H.-G., Niu, K. & Zheng, H. Structural and Morphological Evolution of Lead Dendrites during Electrochemical Migration. *Sci Rep* **3**, 3227 (2013).
65. Influence of sub-zero temperature on nucleation and growth of copper nanoparticles in electrochemical reactions: iScience. https://www.cell.com/iscience/fulltext/S2589-0042(21)01258-X.
66. Zeng, Z. *et al.* Visualization of Electrode–Electrolyte Interfaces in LiPF6/EC/DEC Electrolyte for Lithium Ion Batteries via in Situ TEM. *Nano Lett.* **14**, 1745–1750 (2014).
67. Zeng, Z. *et al.* In Situ Study of Lithiation and Delithiation of MoS2 Nanosheets Using Electrochemical Liquid Cell Transmission Electron Microscopy. *Nano Lett.* **15**, 5214–5220 (2015).
68. Lee, S.-Y. *et al.* Unveiling the mechanisms of lithium dendrite suppression by cationic polymer film induced solid–electrolyte interphase modification. *Energy & Environmental Science* **13**, 1832–1842 (2020).
69. Zhou, S. *et al.* Visualizing interfacial collective reaction behaviour of Li–S batteries. *Nature* **621**, 75–81 (2023).
70. Zhang, Q. *et al.* Atomic dynamics of electrified solid–liquid interfaces in liquid-cell TEM. *Nature* **630**, 643–647 (2024).
71. Vavra, J., Shen, T.-H., Stoian, D., Tileli, V. & Buonsanti, R. Real-time Monitoring Reveals Dissolution/Redeposition Mechanism in Copper Nanocatalysts during the Initial Stages of the CO2 Reduction Reaction. *Angewandte Chemie International Edition* **60**, 1347–1354 (2021).

72. Yang, Y. *et al.* Operando studies reveal active Cu nanograins for CO2 electroreduction. *Nature* **614**, 262–269 (2023).
73. Arán-Ais, R. M. *et al.* Imaging electrochemically synthesized Cu2O cubes and their morphological evolution under conditions relevant to CO2 electroreduction. *Nature communications* **11**, 1–8 (2020).
74. Shen, T.-H., Spillane, L., Peng, J., Shao-Horn, Y. & Tileli, V. Switchable wetting of oxygen-evolving oxide catalysts. *Nat Catal* **5**, 30–36 (2022).
75. Loh, N. D. *et al.* Multistep nucleation of nanocrystals in aqueous solution. *Nature Chem* **9**, 77–82 (2017).
76. De Yoreo, J. J. *et al.* Crystallization by particle attachment in synthetic, biogenic, and geologic environments. *Science* **349**, aaa6760 (2015).
77. Yang, J. *et al.* Formation of two-dimensional transition metal oxide nanosheets with nanoparticles as intermediates. *Nature Materials* **18**, 970–976 (2019).
78. Liu, L., Li, Y. & Wang, F. Electrochemical Corrosion Behavior of Nanocrystalline Materials—a Review. *Journal of Materials Science & Technology* **26**, 1–14 (2010).
79. Li, X. Metal assisted chemical etching for high aspect ratio nanostructures: A review of characteristics and applications in photovoltaics. *Current Opinion in Solid State and Materials Science* **16**, 71–81 (2012).
80. Philp, D. & Stoddart, J. F. Self-Assembly in Natural and Unnatural Systems. *Angewandte Chemie International Edition in English* **35**, 1154–1196 (1996).
81. Controlling and imaging biomimetic self-assembly | Nature Chemistry. https://www.nature.com/articles/nchem.2383.
82. Fan, Z. *et al.* In Situ Transmission Electron Microscopy for Energy Materials and Devices. *Advanced Materials* **31**, 1900608 (2019).
83. Zhu, Y., Wang, J., Chu, H., Chu, Y.-C. & Chen, H. M. In Situ/Operando Studies for Designing Next-Generation Electrocatalysts. *ACS Energy Letters* **5**, 1281–1291 (2020).
84. Understanding Li Diffusion in Li-Intercalation Compounds | Accounts of Chemical Research. https://pubs.acs.org/doi/full/10.1021/ar200329r.
85. Frontiers in Theoretical Analysis of Solid Electrolyte Interphase Formation Mechanism - Takenaka - 2021 - Advanced Materials - Wiley Online Library. https://onlinelibrary.wiley.com/doi/full/10.1002/adma.202100574.
86. Wu, B. *et al.* The role of the solid electrolyte interphase layer in preventing Li dendrite growth in solid-state batteries. *Energy & Environmental Science* **11**, 1803–1810 (2018).
87. Mehdi, B. L. *et al.* Observation and Quantification of Nanoscale Processes in Lithium Batteries by Operando Electrochemical (S)TEM. *Nano Lett.* **15**, 2168–2173 (2015).
88. Zeng, Z. *et al.* Electrode roughness dependent electrodeposition of sodium at the nanoscale. *Nano Energy* **72**, 104721 (2020).
89. Noble metal-free hydrogen evolution catalysts for water splitting - Chemical Society Reviews (RSC Publishing) DOI:10.1039/C4CS00448E. https://pubs.rsc.org/en/content/articlehtml/2015/cs/c4cs00448e?casa_token=GpsTOp5lPNsAAAAA:31Z_FUjZW04Z_kZZraV2-Yqa1eIVWSDUzOeRKawwni-0YbEeYdKkfIrMvcTLDr2fWoqjm569v7LSxwgg&casa_token=mVfE_ju5ZjUAAAAA:wTqjKceCEv8j-nju_RJFDiwG_wjwJ2vJDl_FWnjsRpSx-pBlExABjdPASRymDPrNq-wz-EtvYdgobayp.
90. Zhang, K. & Zou, R. Advanced Transition Metal-Based OER Electrocatalysts: Current Status, Opportunities, and Challenges. *Small* **17**, 2100129 (2021).
91. Understanding Catalytic Activity Trends in the Oxygen Reduction Reaction | Chemical Reviews. https://pubs.acs.org/doi/full/10.1021/acs.chemrev.7b00488.
92. Wang, G. *et al.* Electrocatalysis for CO 2 conversion: from fundamentals to value-added products. *Chemical Society Reviews* **50**, 4993–5061 (2021).
93. Wang, X. *et al.* Morphology and mechanism of highly selective Cu(II) oxide nanosheet catalysts for carbon dioxide electroreduction. *Nature Communications* **12**, 794 (2021).

94. Vavra, J., Shen, T., Stoian, D., Tileli, V. & Buonsanti, R. Real-time monitoring reveals dissolution/redeposition mechanism in copper nanocatalysts during the initial stages of the CO2 reduction reaction. *Angewandte Chemie* **133**, 1367–1374 (2021).
95. Yifan, L. *et al.* Electrochemically scrambled nanocrystals are catalytically active for CO2-to-multicarbons. *Proceedings of the National Academy of Sciences* **117**, 9194–9201 (2020).
96. Grosse, P. *et al.* Dynamic transformation of cubic copper catalysts during CO2 electroreduction and its impact on catalytic selectivity. *Nat Commun* **12**, 6736 (2021).
97. Four-Dimensional Scanning Transmission Electron Microscopy (4D-STEM): From Scanning Nanodiffraction to Ptychography and Beyond | Microscopy and Microanalysis | Cambridge Core. https://www.cambridge.org/core/journals/microscopy-and-microanalysis/article/fourdimensional-scanning-transmission-electron-microscopy-4dstem-from-scanning-nanodiffraction-to-ptychography-and-beyond/A7E922A2C5BFD7FD3F208C537B872B7A.
98. Bustillo, K. C. *et al.* 4D-STEM of Beam-Sensitive Materials. *Acc. Chem. Res.* **54**, 2543–2551 (2021).
99. Chen, Q. *et al.* Nucleation, growth, and superlattice formation of nanocrystals observed in liquid cell transmission electron microscopy. *MRS Bulletin* **45**, 713–726 (2020).
100. Zheng, H. Imaging, understanding, and control of nanoscale materials transformations. *MRS Bulletin* **46**, 443–450 (2021).
101. Chen, Y., Yin, K., Xu, T., Guo, H. & Sun, L. Characterization of Nanomaterials Using In Situ Liquid-Cell Transmission Electron Microscopy: A Review. *ACS Appl. Nano Mater.* **6**, 22545–22567 (2023).
102. Jensen, E. & Mølhave, K. Encapsulated Liquid Cells for Transmission Electron Microscopy. in *Liquid Cell Electron Microscopy* (ed. Ross, F. M.) 35–55 (Cambridge University Press, Cambridge, 2016). doi:10.1017/9781316337455.003.
103. Zhu, C., Wang, W., Liao, H. & Sun, L. In-Situ Liquid Cell TEM. in *In-Situ Transmission Electron Microscopy* (eds. Sun, L., Xu, T. & Zhang, Z.) 221–250 (Springer Nature, Singapore, 2023). doi:10.1007/978-981-19-6845-7_8.
104. Dunn, G. *et al.* Graphene-Sealed Flow Cells for In Situ Transmission Electron Microscopy of Liquid Samples. *ACS Nano* **14**, 9637–9643 (2020).
105. Koo, K., Park, J., Ji, S., Toleukhanova, S. & Yuk, J. M. Liquid-Flowing Graphene Chip-Based High-Resolution Electron Microscopy. *Advanced Materials* **33**, 2005468 (2021).
106. Omme, J. T. van *et al.* Liquid phase transmission electron microscopy with flow and temperature control. *J. Mater. Chem. C* **8**, 10781–10790 (2020).
107. Fen Tan, S. *et al.* Real-time imaging of nanoscale electrochemical Ni etching under thermal conditions. *Chemical Science* **12**, 5259–5268 (2021).
108. Gu, M. *et al.* Demonstration of an Electrochemical Liquid Cell for Operando Transmission Electron Microscopy Observation of the Lithiation/Delithiation Behavior of Si Nanowire Battery Anodes. *Nano Lett.* **13**, 6106–6112 (2013).
109. Zhang, J. *et al.* Understanding the growth mechanisms of metal-based core–shell nanostructures revealed by *in situ* liquid cell transmission electron microscopy. *Journal of Energy Chemistry* **71**, 370–383 (2022).
110. Rasool, H., Dunn, G., Fathalizadeh, A. & Zettl, A. Graphene-sealed Si/SiN cavities for high-resolution in situ electron microscopy of nano-confined solutions. *physica status solidi (b)* **253**, 2351–2354 (2016).
111. Kelly, D. J. *et al.* In Situ TEM Imaging of Solution-Phase Chemical Reactions Using 2D-Heterostructure Mixing Cells. *Advanced Materials* **33**, 2100668 (2021).
112. Clark, N. *et al.* Tracking single adatoms in liquid in a transmission electron microscope. *Nature* **609**, 942–947 (2022).
113. Low Pressure CVD of Silicon Nitride - IOPscience. https://iopscience.iop.org/article/10.1149/1.2100756/meta.
114. Grogan, J. M., Schneider, N. M., Ross, F. M. & Bau, H. H. The Nanoaquarium: A New Paradigm in Electron Microscopy. **92**, (2012).

115. Kelly, D. J. *et al.* Nanometer Resolution Elemental Mapping in Graphene-Based TEM Liquid Cells. *Nano Lett.* **18**, 1168–1174 (2018).
116. Koo, K. *et al.* Ultrathin silicon nitride microchip for in situ/operando microscopy with high spatial resolution and spectral visibility. *Science Advances* **10**, eadj6417 (2024).
117. Moser, T. H. *et al.* The role of electron irradiation history in liquid cell transmission electron microscopy. *Science Advances* **4**, eaaq1202 (2018).
118. Lott, T. S. *et al.* Robust fully controlled nanometer liquid layers for high resolution liquid-cell electron microscopy. *Lab Chip* **23**, 3217–3225 (2023).
119. Nanofluidic chip for liquid TEM cell fabricated by parylene and silicon nitride direct bonding - IOPscience. https://iopscience.iop.org/article/10.1088/1361-6528/aa8196.
120. Unocic, R. R. *et al.* Quantitative Electrochemical Measurements Using In Situ ec-S/TEM Devices. *Microscopy and Microanalysis* **20**, 452–461 (2014).
121. Leenheer, A. J., Sullivan, J. P., Shaw, M. J. & Harris, C. T. A Sealed Liquid Cell for In Situ Transmission Electron Microscopy of Controlled Electrochemical Processes. *Journal of Microelectromechanical Systems* **24**, 1061–1068 (2015).
122. Sasaki, Y. *et al.* Design and fabrication of an electrochemical chip for liquid-phase transmission electron microscopy. *Microscopy* **71**, 238–241 (2022).
123. Kosari, A. *et al.* Challenges to electrochemical evaluation of nanometric sandwiched thin specimens using liquid cells designed for application in liquid-phase TEM corrosion studies. *Corrosion Science* **192**, 109864 (2021).
124. Kushima, A. *et al.* Liquid cell transmission electron microscopy observation of lithium metal growth and dissolution: Root growth, dead lithium and lithium flotsams. *Nano Energy* **32**, 271–279 (2017).
125. Wang, X. *et al.* Morphology and mechanism of highly selective Cu(II) oxide nanosheet catalysts for carbon dioxide electroreduction. *Nat Commun* **12**, 794 (2021).
126. Abdellah, A. M. *et al.* Impact of palladium/palladium hydride conversion on electrochemical CO2 reduction via in-situ transmission electron microscopy and diffraction. *Nat Commun* **15**, 938 (2024).
127. Kim, J. *et al.* Observation of H2 Evolution and Electrolyte Diffusion on MoS2 Monolayer by In Situ Liquid-Phase Transmission Electron Microscopy. *Advanced Materials* **34**, 2206066 (2022).
128. Fu, Q. *et al.* Unraveling and leveraging in situ surface amorphization for enhanced hydrogen evolution reaction in alkaline media. *Nat Commun* **14**, 6462 (2023).
129. Morphological and Structural Evolution of Co3O4 Nanoparticles Revealed by in Situ Electrochemical Transmission Electron Microscopy during Electrocatalytic Water Oxidation | ACS Nano. https://pubs.acs.org/doi/10.1021/acsnano.9b04745.
130. Impagnatiello, A. *et al.* Degradation Mechanisms of Supported Pt Nanocatalysts in Proton Exchange Membrane Fuel Cells: An Operando Study through Liquid Cell Transmission Electron Microscopy. *ACS Appl. Energy Mater.* **3**, 2360–2371 (2020).
131. Wang, F. *et al.* Tracking lithium transport and electrochemical reactions in nanoparticles. *Nat Commun* **3**, 1201 (2012).
132. Zhang, W. *et al.* Kinetic pathways of ionic transport in fast-charging lithium titanate. *Science* **367**, 1030–1034 (2020).
133. Ross, F. Temperature Effects in Liquid Cell Transmission Electron Microscopy. *Microscopy and Microanalysis* **26**, 2566–2567 (2020).
134. Ouyang, D., Weng, J., Chen, M. & Wang, J. Impact of high-temperature environment on the optimal cycle rate of lithium-ion battery. *Journal of Energy Storage* **28**, 101242 (2020).
135. Xu, J. *et al.* Extending the low temperature operational limit of Li-ion battery to −80 °C. *Energy Storage Materials* **23**, 383–389 (2019).
136. Membrane Electrode Assembly for Electrocatalytic CO2 Reduction: Principle and Application - Zhang - 2023 - Angewandte Chemie - Wiley Online Library. https://onlinelibrary.wiley.com/doi/full/10.1002/ange.202302789.

137. Zhang, J. *et al.* High temperature PEM fuel cells. *Journal of Power Sources* **160**, 872–891 (2006).
138. Multilayer Graphene—A Promising Electrode Material in Liquid Cell Electrochemistry - Tan - 2021 - Advanced Functional Materials - Wiley Online Library. https://onlinelibrary.wiley.com/doi/full/10.1002/adfm.202104628.
139. Erni, R. *et al.* Stability and dynamics of small molecules trapped on graphene. *Phys. Rev. B* **82**, 165443 (2010).
140. Nair, R. R. *et al.* Graphene as a transparent conductive support for studying biological molecules by transmission electron microscopy. *Applied Physics Letters* **97**, 153102 (2010).
141. Dahmke, I. N. *et al.* Graphene Liquid Enclosure for Single-Molecule Analysis of Membrane Proteins in Whole Cells Using Electron Microscopy. *ACS Nano* **11**, 11108–11117 (2017).
142. Wierman, J. L., Alden, J. S., Kim, C. U., McEuen, P. L. & Gruner, S. M. Graphene as a protein crystal mounting material to reduce background scatter. *J Appl Cryst* **46**, 1501–1507 (2013).
143. van Deursen, P. M. G. *et al.* Graphene Liquid Cells Assembled through Loop-Assisted Transfer Method and Located with Correlated Light-Electron Microscopy. *Advanced Functional Materials* **30**, 1904468 (2020).
144. Wang, D.-Y. *et al.* Clean-Lifting Transfer of Large-area Residual-Free Graphene Films. *Advanced Materials* **25**, 4521–4526 (2013).
145. Zheng, L. *et al.* Robust ultraclean atomically thin membranes for atomic-resolution electron microscopy. *Nat Commun* **11**, 541 (2020).
146. Yang, J. *et al.* MoS2 Liquid Cell Electron Microscopy Through Clean and Fast Polymer-Free MoS2 Transfer. *Nano Lett.* **19**, 1788–1795 (2019).
147. Jokisaari, J. R. *et al.* Vibrational Spectroscopy of Water with High Spatial Resolution. *Advanced Materials* **30**, 1802702 (2018).
148. Alam, S. B. *et al.* Hybrid nanocapsules for in situ TEM imaging of gas evolution reactions in confined liquids. *Nanoscale* **12**, 18606–18615 (2020).
149. Wu, H. *et al.* Mapping and Controlling Liquid Layer Thickness in Liquid-Phase (Scanning) Transmission Electron Microscopy. *Small Methods* **5**, 2001287 (2021).
150. Mapping Elevated Temperatures with a Micrometer Resolution Using the Luminescence of Chemically Stable Upconversion Nanoparticles | ACS Applied Nano Materials. https://pubs.acs.org/doi/10.1021/acsanm.1c00657.
151. Merkens, S. *et al.* Toward sub-second solution exchange dynamics in flow reactors for liquid-phase transmission electron microscopy. *Nat Commun* **15**, 2522 (2024).
152. Binggeli, M., Shen, T.-H. & Tileli, V. Simulating Current Distribution of Oxygen Evolution Reaction in Microcells Using Finite Element Method. *J. Electrochem. Soc.* **168**, 106508 (2021).
153. Chu, S. & Majumdar, A. Opportunities and challenges for a sustainable energy future. *Nature* **488**, 294–303 (2012).
154. Zhu, P. & Wang, H. High-purity and high-concentration liquid fuels through CO2 electroreduction. *Nature Catalysis* **4**, 943–951 (2021).
155. Jiao, Y., Zheng, Y., Jaroniec, M. & Qiao, S. Z. Design of electrocatalysts for oxygen-and hydrogen-involving energy conversion reactions. *Chemical Society Reviews* **44**, 2060–2086 (2015).
156. Chen, H. *et al.* Active site engineering in porous electrocatalysts. *Advanced Materials* **32**, 2002435 (2020).
157. Nong, H. N. *et al.* Key role of chemistry versus bias in electrocatalytic oxygen evolution. *Nature* **587**, 408–413 (2020).
158. Ferreira, P. J. *et al.* Instability of Pt⁄C electrocatalysts in proton exchange membrane fuel cells: a mechanistic investigation. *Journal of the Electrochemical Society* **152**, A2256 (2005).
159. Cui, C., Gan, L., Heggen, M., Rudi, S. & Strasser, P. Compositional segregation in shaped Pt alloy nanoparticles and their structural behaviour during electrocatalysis. *Nature materials* **12**, 765–771 (2013).

160. Huang, J. *et al.* Potential-induced nanoclustering of metallic catalysts during electrochemical CO2 reduction. *Nature communications* **9**, 1–9 (2018).
161. Zheng, X. *et al.* Theory-driven design of high-valence metal sites for water oxidation confirmed using in situ soft X-ray absorption. *Nature Chemistry* **10**, 149–154 (2018).
162. Timoshenko, J. & Roldan Cuenya, B. In Situ/Operando Electrocatalyst Characterization by X-ray Absorption Spectroscopy. *Chemical Reviews* **121**, 882–961 (2021).
163. Chang, C.-J. *et al.* In situ X-ray diffraction and X-ray absorption spectroscopy of electrocatalysts for energy conversion reactions. *Journal of Materials Chemistry A* **8**, 19079–19112 (2020).
164. Zheng, W., Liu, M. & Lee, L. Y. S. Electrochemical instability of metal–organic frameworks: in situ spectroelectrochemical investigation of the real active sites. *ACS Catalysis* **10**, 81–92 (2019).
165. Beermann, V. *et al.* Real-time imaging of activation and degradation of carbon supported octahedral Pt–Ni alloy fuel cell catalysts at the nanoscale using in situ electrochemical liquid cell STEM. *Energy Environ. Sci.* **12**, 2476–2485 (2019).
166. Jerkiewicz, G. Standard and Reversible Hydrogen Electrodes: Theory, Design, Operation, and Applications. *ACS Catal.* **10**, 8409–8417 (2020).
167. Sophocleous, M. & Atkinson, J. K. A review of screen-printed silver/silver chloride (Ag/AgCl) reference electrodes potentially suitable for environmental potentiometric sensors. *Sensors and Actuators A: Physical* **267**, 106–120 (2017).
168. Seh, Z. W. *et al.* Combining theory and experiment in electrocatalysis: Insights into materials design. *Science* **355**, eaad4998 (2017).
169. Ding, H., Liu, H., Chu, W., Wu, C. & Xie, Y. Structural Transformation of Heterogeneous Materials for Electrocatalytic Oxygen Evolution Reaction. *Chem. Rev.* **121**, 13174–13212 (2021).
170. Zhao, S., Yang, Y. & Tang, Z. Insight into Structural Evolution, Active Sites, and Stability of Heterogeneous Electrocatalysts. *Angewandte Chemie International Edition* **61**, e202110186 (2022).
171. Li, C. W., Ciston, J. & Kanan, M. W. Electroreduction of carbon monoxide to liquid fuel on oxide-derived nanocrystalline copper. *Nature* **508**, 504–507 (2014).
172. Mistry, H. *et al.* Highly selective plasma-activated copper catalysts for carbon dioxide reduction to ethylene. *Nat Commun* **7**, 12123 (2016).
173. Long, C. *et al.* Regulating reconstruction of oxide-derived Cu for electrochemical CO2 reduction toward n-propanol. *Science Advances* **9**, eadi6119 (2023).
174. Zhu, Y., Wang, J., Chu, H., Chu, Y.-C. & Chen, H. M. In Situ/Operando Studies for Designing Next-Generation Electrocatalysts. *ACS Energy Lett.* **5**, 1281–1291 (2020).
175. Chee, S. W., Lunkenbein, T., Schlögl, R. & Roldán Cuenya, B. Operando Electron Microscopy of Catalysts: The Missing Cornerstone in Heterogeneous Catalysis Research? *Chem. Rev.* **123**, 13374–13418 (2023).
176. Zhu, P. & Wang, H. High-purity and high-concentration liquid fuels through CO2 electroreduction. *Nat Catal* **4**, 943–951 (2021).
177. Nitopi, S. *et al.* Progress and Perspectives of Electrochemical CO2 Reduction on Copper in Aqueous Electrolyte. *Chem. Rev.* **119**, 7610–7672 (2019).
178. Dinh, C.-T. *et al.* CO2 electroreduction to ethylene via hydroxide-mediated copper catalysis at an abrupt interface. *Science* **360**, 783–787 (2018).
179. Jung, H. *et al.* Electrochemical Fragmentation of Cu2O Nanoparticles Enhancing Selective C–C Coupling from CO2 Reduction Reaction. *J. Am. Chem. Soc.* **141**, 4624–4633 (2019).
180. Lei, Q. *et al.* Investigating the Origin of Enhanced C2+ Selectivity in Oxide-/Hydroxide-Derived Copper Electrodes during CO2 Electroreduction. *J. Am. Chem. Soc.* **142**, 4213–4222 (2020).
181. Xiao, H., Goddard, W. A., Cheng, T. & Liu, Y. Cu metal embedded in oxidized matrix catalyst to promote CO2 activation and CO dimerization for electrochemical reduction of CO2. *Proceedings of the National Academy of Sciences* **114**, 6685–6688 (2017).
182. Cheng, D. *et al.* The nature of active sites for carbon dioxide electroreduction over oxide-derived copper catalysts. *Nat Commun* **12**, 395 (2021).

183. Amirbeigiarab, R. *et al.* Atomic-scale surface restructuring of copper electrodes under CO2 electroreduction conditions. *Nat Catal* **6**, 837–846 (2023).
184. Lin, S.-C. *et al.* Operando time-resolved X-ray absorption spectroscopy reveals the chemical nature enabling highly selective CO2 reduction. *Nat Commun* **11**, 3525 (2020).
185. Lee, S. H. *et al.* Oxidation State and Surface Reconstruction of Cu under CO2 Reduction Conditions from In Situ X-ray Characterization. *J. Am. Chem. Soc.* **143**, 588–592 (2021).
186. Jiang, X., Herricks, T. & Xia, Y. CuO Nanowires Can Be Synthesized by Heating Copper Substrates in Air. *Nano Lett.* **2**, 1333–1338 (2002).
187. (IUCr) IFEFFIT : interactive XAFS analysis and FEFF fitting. *Journal of Synchrotron Radiation* vol. 8 322–324 https://scripts.iucr.org/cgi-bin/paper?S0909049500016964 (2001).
188. Ravel, B. & Gallagher, K. Atomic structure and the magnetic properties of Zr-doped Sm2Co17. *Phys. Scr.* **2005**, 606 (2005).
189. Newville, M., Līviņš, P., Yacoby, Y., Rehr, J. J. & Stern, E. A. Near-edge x-ray-absorption fine structure of Pb: A comparison of theory and experiment. *Phys. Rev. B* **47**, 14126–14131 (1993).
190. Ankudinov, A. L., Ravel, B., Rehr, J. J. & Conradson, S. D. Real-space multiple-scattering calculation and interpretation of x-ray-absorption near-edge structure. *Phys. Rev. B* **58**, 7565–7576 (1998).
191. Kresse, G. & Furthmüller, J. Efficient iterative schemes for ab initio total-energy calculations using a plane-wave basis set. *Phys. Rev. B* **54**, 11169–11186 (1996).
192. Perdew, J. P. *et al.* Atoms, molecules, solids, and surfaces: Applications of the generalized gradient approximation for exchange and correlation. *Phys. Rev. B* **46**, 6671–6687 (1992).
193. Dudarev, S. L., Botton, G. A., Savrasov, S. Y., Humphreys, C. J. & Sutton, A. P. Electron-energy-loss spectra and the structural stability of nickel oxide: An LSDA+U study. *Phys. Rev. B* **57**, 1505–1509 (1998).
194. Nolan, M. & Elliott, S. D. The p-type conduction mechanism in Cu2O: a first principles study. *Phys. Chem. Chem. Phys.* **8**, 5350–5358 (2006).
195. Sun, X. *et al.* Atomic-Scale Mechanism of Unidirectional Oxide Growth. *Advanced Functional Materials* **30**, 1906504 (2020).
196. Monkhorst, H. J. & Pack, J. D. Special points for Brillouin-zone integrations. *Phys. Rev. B* **13**, 5188–5192 (1976).
197. Mills, G., Jónsson, H. & Schenter, G. K. Reversible work transition state theory: application to dissociative adsorption of hydrogen. *Surface Science* **324**, 305–337 (1995).
198. Nudged elastic band method for finding minimum energy paths of transitions | Classical and Quantum Dynamics in Condensed Phase Simulations. https://www.worldscientific.com/doi/10.1142/9789812839664_0016.
199. Rackauskas, S. *et al.* In Situ Study of Noncatalytic Metal Oxide Nanowire Growth. *Nano Lett.* **14**, 5810–5813 (2014).
200. Atomic-Scale Mechanism of Unidirectional Oxide Growth - Sun - 2020 - Advanced Functional Materials - Wiley Online Library. https://onlinelibrary.wiley.com/doi/full/10.1002/adfm.201906504.
201. Steger, C. An unbiased detector of curvilinear structures. *IEEE Transactions on Pattern Analysis and Machine Intelligence* **20**, 113–125 (1998).
202. Chen, H. *et al.* Active Site Engineering in Porous Electrocatalysts. *Advanced Materials* **32**, 2002435 (2020).
203. Zhuang, T.-T. *et al.* Copper nanocavities confine intermediates for efficient electrosynthesis of C3 alcohol fuels from carbon monoxide. *Nat Catal* **1**, 946–951 (2018).
204. Yang, P.-P. *et al.* Protecting Copper Oxidation State via Intermediate Confinement for Selective CO2 Electroreduction to C2+ Fuels. *J. Am. Chem. Soc.* **142**, 6400–6408 (2020).
205. Kim, C. *et al.* Tailored catalyst microenvironments for CO2 electroreduction to multicarbon products on copper using bilayer ionomer coatings. *Nat Energy* **6**, 1026–1034 (2021).

206. Gao, D. *et al.* Selective CO2 Electroreduction to Ethylene and Multicarbon Alcohols via Electrolyte-Driven Nanostructuring. *Angewandte Chemie* **131**, 17203–17209 (2019).
207. Lum, Y. & Ager, J. W. Evidence for product-specific active sites on oxide-derived Cu catalysts for electrochemical CO2 reduction. *Nat Catal* **2**, 86–93 (2019).
208. Garza, A. J., Bell, A. T. & Head-Gordon, M. Is Subsurface Oxygen Necessary for the Electrochemical Reduction of CO2 on Copper? *J. Phys. Chem. Lett.* **9**, 601–606 (2018).
209. Kim, J. Y., Rodriguez, J. A., Hanson, J. C., Frenkel, A. I. & Lee, P. L. Reduction of CuO and Cu2O with H2: H Embedding and Kinetic Effects in the Formation of Suboxides. *J. Am. Chem. Soc.* **125**, 10684–10692 (2003).
210. Wang, X., Hanson, J. C., Frenkel, A. I., Kim, J.-Y. & Rodriguez, J. A. Time-resolved Studies for the Mechanism of Reduction of Copper Oxides with Carbon Monoxide: Complex Behavior of Lattice Oxygen and the Formation of Suboxides. *J. Phys. Chem. B* **108**, 13667–13673 (2004).
211. Lei, Q. *et al.* Structural evolution and strain generation of derived-Cu catalysts during CO2 electroreduction. *Nat Commun* **13**, 4857 (2022).
212. Choi, C. *et al.* Highly active and stable stepped Cu surface for enhanced electrochemical CO2 reduction to C2H4. *Nat Catal* **3**, 804–812 (2020).
213. Weng, L.-C., T. Bell, A. & Z. Weber, A. Towards membrane-electrode assembly systems for CO 2 reduction: a modeling study. *Energy & Environmental Science* **12**, 1950–1968 (2019).
214. Advances and challenges in understanding the electrocatalytic conversion of carbon dioxide to fuels | Nature Energy. https://www.nature.com/articles/s41560-019-0450-y.
215. Kim, T. & Palmore, G. T. R. A scalable method for preparing Cu electrocatalysts that convert CO2 into C2+ products. *Nat Commun* **11**, 3622 (2020).
216. Ross, M. B. *et al.* Designing materials for electrochemical carbon dioxide recycling. *Nat Catal* **2**, 648–658 (2019).
217. Gattrell, M., Gupta, N. & Co, A. A review of the aqueous electrochemical reduction of CO2 to hydrocarbons at copper. *Journal of Electroanalytical Chemistry* **594**, 1–19 (2006).
218. Li, P.-Z. *et al.* A Triazole-Containing Metal–Organic Framework as a Highly Effective and Substrate Size-Dependent Catalyst for CO2 Conversion. *J. Am. Chem. Soc.* **138**, 2142–2145 (2016).
219. L. Stephens, I. E., S. Bondarenko, A., Grønbjerg, U., Rossmeisl, J. & Chorkendorff, I. Understanding the electrocatalysis of oxygen reduction on platinum and its alloys. *Energy & Environmental Science* **5**, 6744–6762 (2012).
220. Grosse, P. *et al.* Dynamic Changes in the Structure, Chemical State and Catalytic Selectivity of Cu Nanocubes during CO2 Electroreduction: Size and Support Effects. *Angewandte Chemie* **130**, 6300–6305 (2018).
221. Li, Y. *et al.* Crystallinity Dependence of Ruthenium Nanocatalyst toward Hydrogen Evolution Reaction. *ACS Catal.* **8**, 5714–5720 (2018).
222. De Luna, P. *et al.* Catalyst electro-redeposition controls morphology and oxidation state for selective carbon dioxide reduction. *Nat Catal* **1**, 103–110 (2018).
223. Che, Q. *et al.* One-step electrodeposition of a hierarchically structured S-doped NiCo film as a highly-efficient electrocatalyst for the hydrogen evolution reaction. *Nanoscale* **10**, 15238–15248 (2018).
224. Lu, X. & Zhao, C. Electrodeposition of hierarchically structured three-dimensional nickel–iron electrodes for efficient oxygen evolution at high current densities. *Nat Commun* **6**, 6616 (2015).
225. Day, T. M., Unwin, P. R. & Macpherson, J. V. Factors Controlling the Electrodeposition of Metal Nanoparticles on Pristine Single Walled Carbon Nanotubes. *Nano Lett.* **7**, 51–57 (2007).
226. Pei, A., Zheng, G., Shi, F., Li, Y. & Cui, Y. Nanoscale Nucleation and Growth of Electrodeposited Lithium Metal. *Nano Lett.* **17**, 1132–1139 (2017).
227. Qiao, X., Li, H., Zhao, W. & Li, D. Effects of deposition temperature on electrodeposition of zinc–nickel alloy coatings. *Electrochimica Acta* **89**, 771–777 (2013).

228. Temperature-Dependent Nucleation and Growth of Dendrite-Free Lithium Metal Anodes - Yan - 2019 - Angewandte Chemie - Wiley Online Library. https://onlinelibrary.wiley.com/doi/full/10.1002/ange.201905251.
229. Liquid/Solid Phase Diagrams of Binary Carbonates for Lithium Batteries Part II - IOPscience. https://iopscience.iop.org/article/10.1149/1.1353568/meta.
230. Jin, M. *et al.* Shape-Controlled Synthesis of Copper Nanocrystals in an Aqueous Solution with Glucose as a Reducing Agent and Hexadecylamine as a Capping Agent. *Angewandte Chemie International Edition* **50**, 10560–10564 (2011).
231. Lin, T.-Y. *et al.* Electron Beam Irradiation-Induced Deoxidation and Atomic Flattening on the Copper Surface. *ACS Appl. Mater. Interfaces* **11**, 40909–40915 (2019).
232. Ely, D. R. & García, R. E. Heterogeneous Nucleation and Growth of Lithium Electrodeposits on Negative Electrodes. *J. Electrochem. Soc.* **160**, A662 (2013).
233. Effect of Current Density on Morphology of Lithium Electrodeposited in Ionic Liquid-Based Electrolytes - IOPscience. https://iopscience.iop.org/article/10.1149/2.0331409jes/meta.
234. Gao, W. & Wang, J. Synthetic micro/nanomotors in drug delivery. *Nanoscale* **6**, 10486–10494 (2014).
235. Kagan, D. *et al.* Rapid delivery of drug carriers propelled and navigated by catalytic nanoshuttles. *Small* **6**, 2741–2747 (2010).
236. Kagan, D. *et al.* Chemical sensing based on catalytic nanomotors: Motion-based detection of trace silver. *Journal of the American Chemical Society* **131**, 12082–12083 (2009).
237. Zhou, C., Zhang, H. P., Tang, J. & Wang, W. Photochemically Powered AgCl Janus Micromotors as a Model System to Understand Ionic Self-Diffusiophoresis. *Langmuir* **34**, 3289–3295 (2018).
238. Zarei, M. & Zarei, M. Self-Propelled Micro/Nanomotors for Sensing and Environmental Remediation. *Small* **14**, 1–17 (2018).
239. Dong, B., Zhou, T., Zhang, H. & Li, C. Y. Directed self-assembly of nanoparticles for nanomotors. *ACS Nano* **7**, 5192–5198 (2013).
240. Paxton, W. F. *et al.* Catalytic nanomotors: Autonomous movement of striped nanorods. *Journal of the American Chemical Society* **126**, 13424–13431 (2004).
241. Yang, Q. *et al.* Recent Advances in Motion Control of Micro/Nanomotors. *Advanced Intelligent Systems* **2**, 2000049 (2020).
242. Fernández-Medina, M., Ramos-Docampo, M. A., Hovorka, O., Salgueiriño, V. & Städler, B. Recent Advances in Nano- and Micromotors. *Advanced Functional Materials* **30**, 1–17 (2020).
243. Chen, C., Soto, F., Karshalev, E., Li, J. & Wang, J. Hybrid Nanovehicles: One Machine, Two Engines. *Advanced Functional Materials* **29**, 1–10 (2019).
244. Dey, K. K. & Sen, A. Chemically Propelled Molecules and Machines. *Journal of the American Chemical Society* **139**, 7666–7676 (2017).
245. Li, J., Rozen, I. & Wang, J. Rocket Science at the Nanoscale. *ACS Nano* **10**, 5619–5634 (2016).
246. Ma, X., Hahn, K. & Sanchez, S. Catalytic mesoporous janus nanomotors for active cargo delivery. *Journal of the American Chemical Society* **137**, 4976–4979 (2015).
247. De Ávila, B. E. F. *et al.* Micromotor-enabled active drug delivery for in vivo treatment of stomach infection. *Nature Communications* **8**, 1–8 (2017).
248. Howse, J. R. *et al.* Self-Motile Colloidal Particles: From Directed Propulsion to Random Walk. *Physical Review Letters* **99**, 8–11 (2007).
249. Wang, S. & Wu, N. Selecting the swimming mechanisms of colloidal particles: Bubble propulsion versus self-diffusiophoresis. *Langmuir* **30**, 3477–3486 (2014).
250. Wang, Y. *et al.* Photocatalytically Powered Matchlike Nanomotor for Light-Guided Active SERS Sensing. *Angewandte Chemie - International Edition* **57**, 13110–13113 (2018).
251. Brooks, A. M. *et al.* Shape-directed rotation of homogeneous micromotors via catalytic self-electrophoresis. *Nature Communications* **10**, 1–9 (2019).

252. Xu, L., Mou, F., Gong, H., Luo, M. & Guan, J. Light-driven micro/nanomotors: From fundamentals to applications. *Chemical Society Reviews* **46**, 6905–6926 (2017).
253. Garcia-Gradilla, V. *et al.* Functionalized ultrasound-propelled magnetically guided nanomotors: Toward practical biomedical applications. *ACS Nano* **7**, 9232–9240 (2013).
254. Li, J. *et al.* Magneto-Acoustic Hybrid Nanomotor. *Nano Letters* **15**, 4814–4821 (2015).
255. Rahman, M. M., Chowdhury, M. M. & Alam, M. K. Rotating-Electric-Field-Induced Carbon-Nanotube-Based Nanomotor in Water: A Molecular Dynamics Study. *Small* **13**, 1–10 (2017).
256. Šípová-Jungová, H., Andrén, D., Jones, S. & Käll, M. Nanoscale Inorganic Motors Driven by Light: Principles, Realizations, and Opportunities. *Chemical Reviews* **120**, 269–287 (2020).
257. Laocharoensuk, R., Burdick, J. & Wang, J. Carbon-nanotube-induced acceleration of catalytic nanomotors. *ACS nano* **2**, 1069–1075 (2008).
258. Benjamin, I. Chemical reactions and solvation at liquid interfaces: A microscopic perspective. *Chemical Reviews* **96**, 1449–1475 (1996).
259. Quan, Z., Wang, Y. & Fang, J. High-index faceted noble metal nanocrystals. *Accounts of Chemical Research* **46**, 191–202 (2013).
260. Katsuyama, T. *et al.* Synthesis of Tetrahexahedral Platinum. *Handbook of Chemistry and Physics* 732–735 (2007).
261. Liu, W. *et al.* Visible-light-driven cuprous oxide nanomotors with surface-heterojunction-induced propulsion. *Nanoscale Horizons* **6**, 238–244 (2021).
262. Liao, H. G., Cui, L., Whitelam, S. & Zheng, H. Real-time imaging of Pt3Fe nanorod growth in solution. *Science* **336**, 1011–1014 (2012).
263. Liao, H. G. *et al.* Facet development during platinum nanocube growth. *Science* **345**, 916–919 (2014).
264. Zheng, H. Imaging, understanding, and control of nanoscale materials transformations. *MRS Bulletin* **46**, 443–450 (2021).
265. Tian, X., Anand, U., Mirsaidov, U. & Zheng, H. Spontaneous Reshaping and Splitting of AgCl Nanocrystals under Electron Beam Illumination. *Small* **14**, 1–7 (2018).
266. Yin, Z. W. *et al.* Visualization of facet-dependent pseudo-photocatalytic behavior of TiO2 nanorods for water splitting using In situ liquid cell TEM. *Nano Energy* **62**, 507–512 (2019).
267. Roy, P., Lynch, R. & Schmuki, P. Electron beam induced in-vacuo Ag deposition on TiO2 from ionic liquids. *Electrochemistry Communications* **11**, 1567–1570 (2009).
268. Kolmakova, N. & Kolmakov, A. Scanning electron microscopy for in situ monitoring of semiconductor-liquid interfacial processes: Electron assisted reduction of Ag ions from aqueous solution on the surface of TiO2 rutile nanowire. *Journal of Physical Chemistry C* **114**, 17233–17237 (2010).
269. Leligny, H. & Monier, J. C. Structure de dichlorure de cadmium tétrahydraté. *Acta Crystallographica Section B: Structural Crystallography and Crystal Chemistry* **35**, 569–573 (1979).
270. Woehl, T. J., Moser, T., Evans, J. E. & Ross, F. M. Electron-beam-driven chemical processes during liquid phase transmission electron microscopy. *MRS Bulletin* **45**, 746–753 (2020).
271. Grogan, J. M., Schneider, N. M., Ross, F. M. & Bau, H. H. Bubble and pattern formation in liquid induced by an electron beam. *Nano Letters* **14**, 359–364 (2014).
272. Zhang, Q. *et al.* Defect-mediated ripening of core-shell nanostructures. *Nature Communications* **13**, 2211 (2022).
273. Ibele, M., Mallouk, T. E. & Sen, A. Schooling Behavior of Light-Powered Autonomous Micromotors in Water. *Angewandte Chemie* **121**, 3358–3362 (2009).